A. I. Alikhanian National Science Laboratory
(Yerevan Physics Institute)

Gayane Ghevondyan

Study of the ARICH detector performance, as one of the essential components of charged particle identification in the Belle II experiment

Thesis for acquiring the degree of candidate of physical-mathematical sciences with nucleus, elementary particles and cosmic rays physics (01.04.16) specialization

Scientific supervisor

Norayr Akopov

YEREVAN 2024

Contents

Introduction

The Belle II experiment at the SuperKEKB asymmetric e^+e^- collider [1][2] in the High Energy Accelerator Research Organization (KEK, Tsukuba, Japan) is searching for CP asymmetries in different rare decays, as well as new physics (NP) beyond the standard model (BSM) and aims to collect a high statistics data set corresponding to an integrated luminosity of 50[ab^{-1}]. The primary physics goals of Belle II, as a next-generation flavor factory, are to search for NP in the flavor sector at the intensity frontier, and to improve the precision of measurements of Standard Model (SM) parameters. The SuperKEKB facility is designed to collide electrons and positrons at center-of-mass energies in the regions of the Υ resonances. Most of the data will be collected at the $\Upsilon(4S)$ resonance, which is just above the threshold for the production of B-meson pairs where no fragmentation particles are produced.

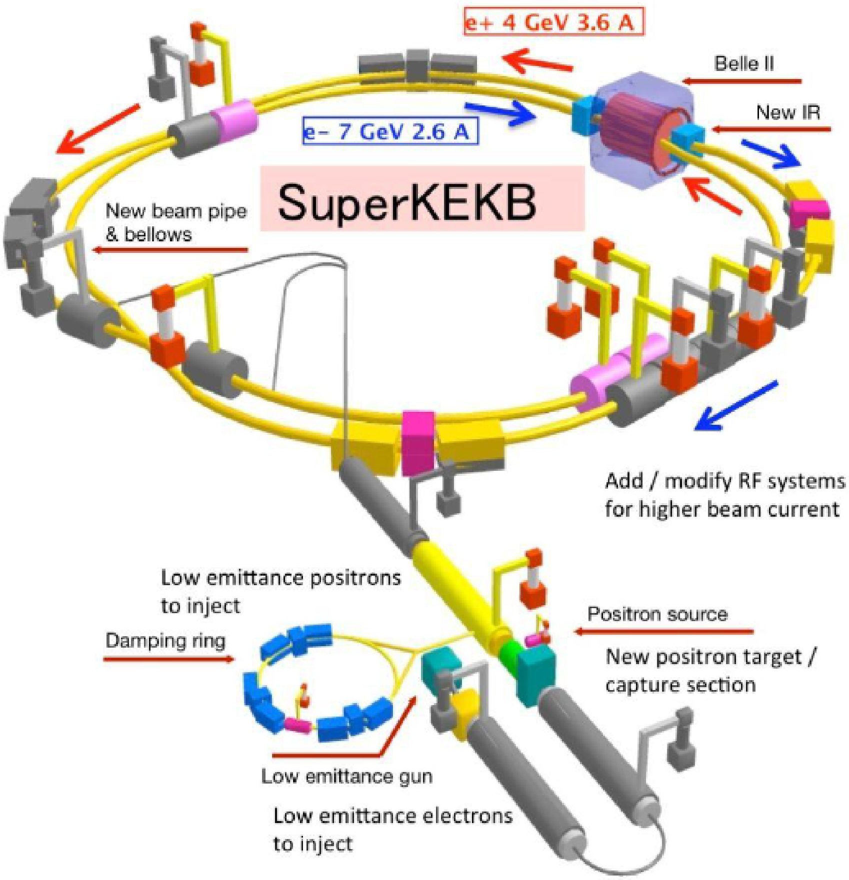

Figure 1: *Schematic overview of SuperKEKB accelerator*

The schematic overview of the SuperKEKB accelerator and the Belle II detector are shown on Fig.1 and 2

The accelerator is designed with asymmetric beam energies to provide a boost to the center-of-mass system and thereby allow for time-dependent charge-parity (CP) symmetry violation measurement.

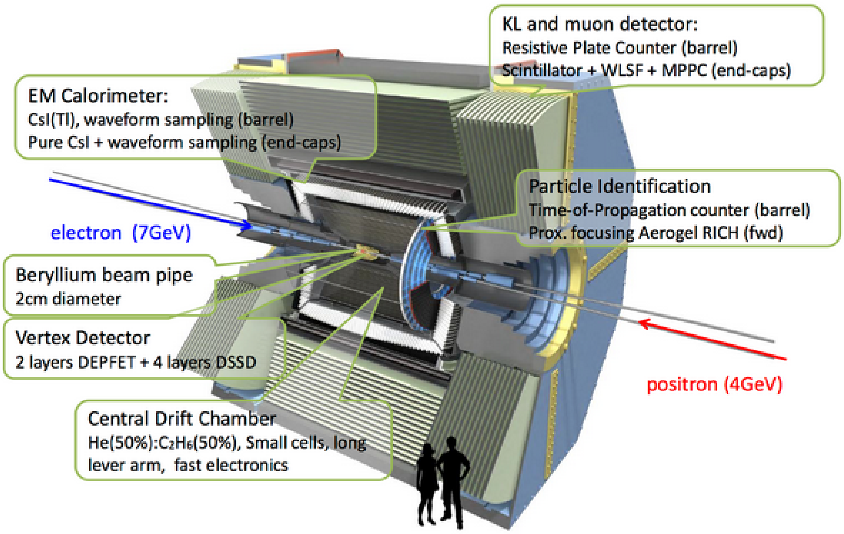

Figure 2: *Belle II detector*

At its present level of experimental precision and the energies achieved thus far, the Standard Model represents the most thoroughly tested theory of nature at a fundamental level. Although it has been remarkably successful in explaining the behaviors of fundamental particles and their interactions, except for gravity, it fails to address numerous fundamental questions. The Standard Model fails to account for why there are specifically three generations of elementary fermions or the observed hierarchy in fermion masses. It explains the origin of the mass for fundamental particles through spontaneous electroweak symmetry breaking, which gives rise to the Higgs boson. However, it does not definitively explain the masses of neutrinos. Furthermore, it remains unclear whether the Standard Model includes only a single Higgs boson or if there might exist a more complex Higgs sector with additional Higgs-like particles, as proposed in supersymmetry and other new physics models. Additionally, on a cosmological scale, the unresolved issue of matter-antimatter asymmetry in the universe persists. The violation of CP symmetry is essential for the development of a matter-dominated universe. However, the observed CP violation within the quark sector, arising from the complex phase of the Cabibbo-Kobayashi-Maskawa (CKM) matrix, is significantly insufficient by many orders of magnitude to account for the prevalence of matter over antimatter in the universe. Therefore, there must be undiscovered sources that contribute to the CP asymmetry. Additionally, the CKM matrix elements exhibit a roughly diagonal hierarchy, contrary to predictions from the Standard Model. This hints at the possible existence of a new mechanism, such as flavor symmetry, that remains unbroken at higher energy scales.

There are several experimental reasons that make SuperKEKB and Belle II perfectly suited to address these puzzles in particle physics. [1]

- A very clean sample of $B^0\bar{B}^0$ pairs in a quantum correlated $1--$ state is produced because of the processing that the Υ $(4S)$ resonance produces. The low background environment effectively allows for the reconstruction of π^0, $\rho^{\pm}$, η, η' mesons as well as the reconstruction of neutral K_L^0 mesons.

- The detector hermeticism and azimuthal asymmetry create very small charged asymmetries in reconstruction, while the flavor production asymmetry is zero.

- Lorentz boost of the e^+e^- system is large enough because of asymmetric beam energies. That allows many particles, specifically B or D mesons, to travel a remarkable distance before decaying. This feature allows to measure lifetimes, mixing parameters, and CP violation more precisely. Furthermore, B and D decays produce large samples of τ leptons by using a e^+e- machine that allows us to measure rare τ decays.

- B tag procedure when the products of other B were detected.
- We have a high B, D and τ reconstruction efficiency and very low trigger bias because of detector occupancy and low track multiplicities, which leads to less correction and systematic uncertainties in many types of measurement.
- Belle II experiment is able to measure absolute branching fractions since the absolute delivered luminosity is measured with Bhabha scattering.

The sensitivity of Belle II to NP depends on the strength of the flavor-violating couplings of the NP. The mass reach for new particle/process effects can be as high as $O(100TeV)$ if the couplings are not as suppressed as in SM [4]. In the past, quantum corrections in process measurements provided insights into high-mass-scale physics, even before accelerators could directly explore these scales. Belle II and SuperKEKB will leverage our capabilities at the intensity frontier by advancing beyond mere observation of a new-physics effect. Instead, they aim to thoroughly characterize it through tightly-constrained measurements across various related flavor physics reactions. The ARICH counter [2],[3] is located in the forward end-cap of the Belle II spectrometer. It is a novel type of particle identification device that has been developed for the Belle II experiment that is capable of identifying pions and kaons with momenta up to 4[GeV/c] by detecting Cherenkov photons emitted in a silica aerogel radiator.

The studies performed in presented thesis are devoted to detailed investigations of the ARICH performance aiming to provide detailed tables with efficiencies and mis-ID values in 2D case (dependencies on momentum and angle) and 1D case (momentum dependencies integrated over the particles angle, or angular dependencies integrated over particles momentum). Also, a possible dependence on the number of charged tracks in the final state was investigated.

1 The Belle II experiment

In this chapter the Belle II experiment will be discussed. Belle II is a particle physics experiment at SuperKEKB, a particle accelerator at Japan's KEK High Energy Physics Research Center which was designed in order to enable researchers to discover new interactions and new particles.

1.1 SuperKEKB accelerator

SuperKEKB(Fig.3) is Japan's largest electron-positron collider, located at the KEK Tsukuba Campus. The Belle II detector is a large particle detector surrounding the collision point of the SuperKEKB accelerator to record the interactions and decays of particles produced in the collisions. SuperKEKB is a particle accelerator, specifically a robust 3 km electron-positron storage ring. This enhanced SuperKEKB accelerator is the successor to the KEKB accelerator, which ran from 1998 to 2010 and set the world record for luminosity (the rate of particle collisions (or interactions) per unit area and time in a particle accelerator). A high luminosity allows for exceptional measurement precision, making both KEKB and SuperKEKB, in particular, designed for extremely accurate measurements.

(a) (b)

Figure 3: *SuperKEKB.*

SuperKEKB is a circular collider with a circumference of approximately 3 km, located 11 meters beneath the surface. It accelerates beams of electrons and positrons to nearly the speed of light, causing them to collide. Together with the Belle II detector, SuperKEKB serves as a facility aimed at exploring new physical phenomena that could provide insights into the fundamental mysteries surrounding the origins of the universe.

The SuperKEKB accelerator began collecting data for physics analysis in 2019 and set the world record for the highest luminosity (a measure of collision performance) in June 2020. Since then, the accelerator has consistently broken luminosity records. However, to continue improving and achieving new milestones, a shutdown period was required for necessary upgrades.

SuperKEKB entered an 18-month shutdown in June 2022 for essential upgrades and maintenance to the accelerator. These improvements were designed to preserve beam quality even as the beams were focused more tightly. Key upgrades included the installation of a "nonlinear collimator" on the positron ring to reduce beam instability, a redesign of the electron injector, and the addition of a pulse solenoid to the linear injector. Notably, the installation of the "nonlinear collimator" is a world-first, and it is expected to enhance luminosity while minimizing background noise caused by the beams.

On 29 January 2024, the SuperKEKB accelerator and the Belle II detector restarted operations for the first time in 18 months, following the completion of a number of upgrades.

1.2 The Belle II detector

As was mentioned, the powerful new particle accelerator SuperKEKB replaced its predecessor model KEKB in 2019.

The particle beams of matter (electrons) and their antiparticles (positrons) colliding in the SuperKEKB are expected to produce a collision rate up to 30 times higher than its predecessor. The particles generated in the collisions and their degradation products will be measured and analyzed in the Belle II experiment. For this purpose, various detector components are arranged cylindrically around the beamline. The detector components can detect the individual degradation end products of the decay (such as electrons, muons, pions, and other particles). The entire Belle II detector is about 10 m wide, equally high, and weighs a total of 1500 tons.

The horizontal sectional view of the Belle II spectrometer is shown in Fig.4.

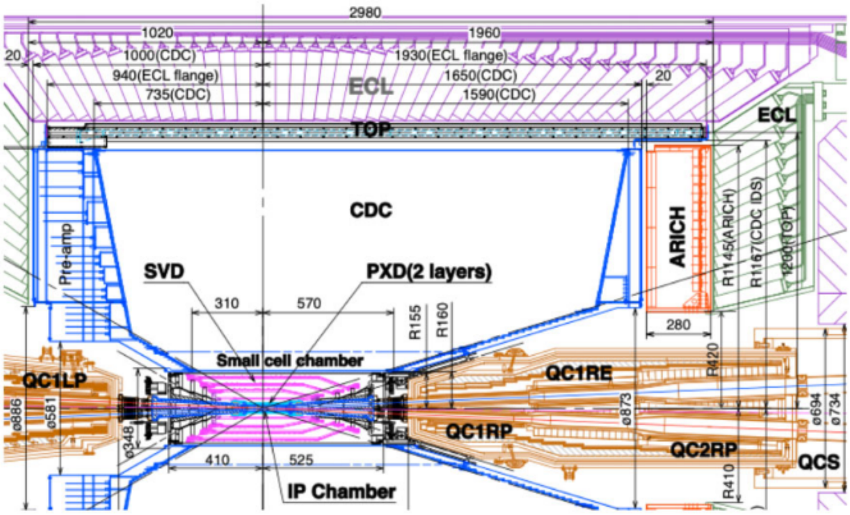

Figure 4: *Horizontal sectional view of the Belle II spectrometer. The dimensions on the figure are in mm.*

Going outwards from the interaction point, the Belle II detector consists of [5]:

- a pixel detector employing $DEPFET$ (DEPleted Field Effect Transistor) technology (PXD) for accurate vertex detection.
- a double-walled Beryllium beam pipe with a radius of 12 mm cooled by paraffin.

- the central drift chamber (CDC) measures the momentum and energy loss of charged particles, while also delivering a rapid trigger signal for the Level-1 (L1) trigger system.
- a proximity-focusing Aerogel Ring Imaging Cherenkov detector(ARICH) is employed for particle identification (PID) in the forward end-cap.
- four layers of double-sided silicon strip detectors spanning the full $17° - 150°$ acceptance of the Belle II detector (SVD) are used to extrapolate tracks reconstructed in the CDC and to reconstruct low-momentum tracks in the PXD.
- the barrel region, where a time-of-propagation counter (TOP) utilizes an array of 16 quartz bars positioned between the outer cover of the CDC and the inner surface of the calorimeter. This setup provides particle identification (PID) information and a timing signal with a resolution of a few nanoseconds to the trigger system.
- the barrel region which features a segmented array of $CsI(Tl)$ crystals, while the end-caps are equipped with pure CsI crystals that are read out by photodiodes for electromagnetic calorimetry (ECL).
- an iron support structure that acts as the return path for the magnetic flux. It is equipped with glass-electrode resistive plate counters (RPC) in the barrel region and scintillator strips in the end-caps for K_L and muon detection (KLM).
- and finally, superconducting solenoid generates a uniform magnetic field of $1.5T$.

More detailed about detector systems can be seen below.

1.2.1 Inner and Tracking detectors

For position and momentum measurements of the particle emitted in the collisions we rely on the information from high-resolution vertex detectors. The VerteX Detector (VXD) system of Belle II is fundamental to reconstruct the vertex of B-mesons decays, with lifetimes of the order of the picoseconds (one trillionth of a second) and of the other short-lived particle decays.

The Belle II VXD consists of two inner layers of a silicon PiXel Detector (PXD) followed by four layers of a Silicon Vertex Detector (SVD), which is composed of double-sided silicon strips sensors. The whole VXD is immersed in a 1.5T magnetic field parallel to the beam axis.

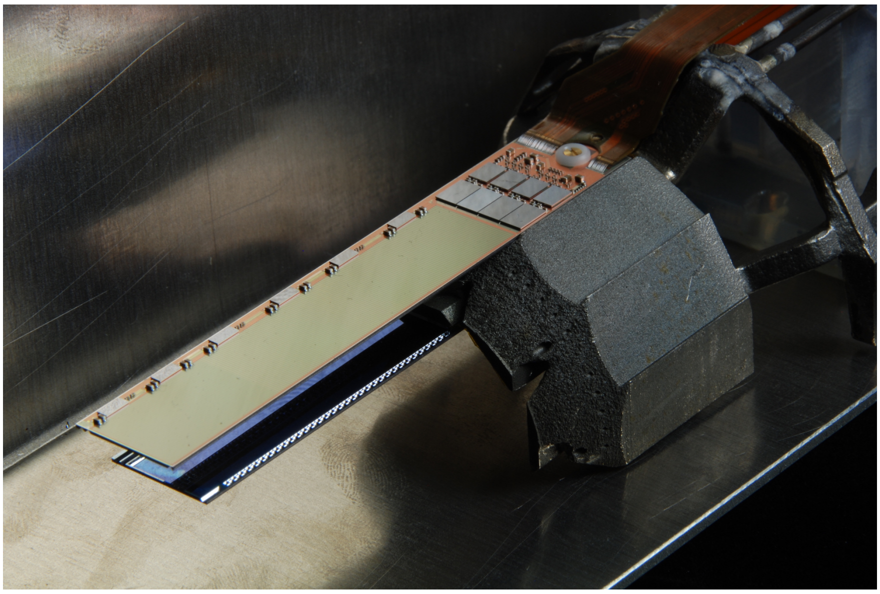

Figure 5: *Technical drawing of the PXD arrangement – the two innermost layers of the Belle II Experiment*

The Belle II pixel detector (PXD) uses ultra-pure silicon, 1000 times purer than standard transistors. It integrates 200,000 DEPFET (Depleted p-channel Field Effect Transistor) pixel cells on $88cm^3$. DEPFET technology amplifies tiny signals from single photons or particles within each pixel, enabling precise tracking with 10-micrometer accuracy.

To process pixel data quickly, application-specific integrated circuits (ASICs) are attached to the sensor substrate, digitizing and transmitting data at 50,000 images per second. The sensor module connects 200,000 pixels to the ASICs, with the thin and lightweight DEPFET matrix minimizing interference with particle tracking.

The PXD collaboration developed 75-micrometer thick DEPFET sensor modules supported by a frame, with ASICs mounted using ball grid technology and flexible power/data lines. Two modules form a "ladder" structure, supported at the ends.

These thin DEPFET ladders are arranged cylindrically around the interaction point, with a CO2 cooling unit for the ASICs. The PXD vertex detector includes 8 inner and 12 outer ladders, positioned 14 and 22 millimeters from the interaction point, ensuring high precision in particle tracking.

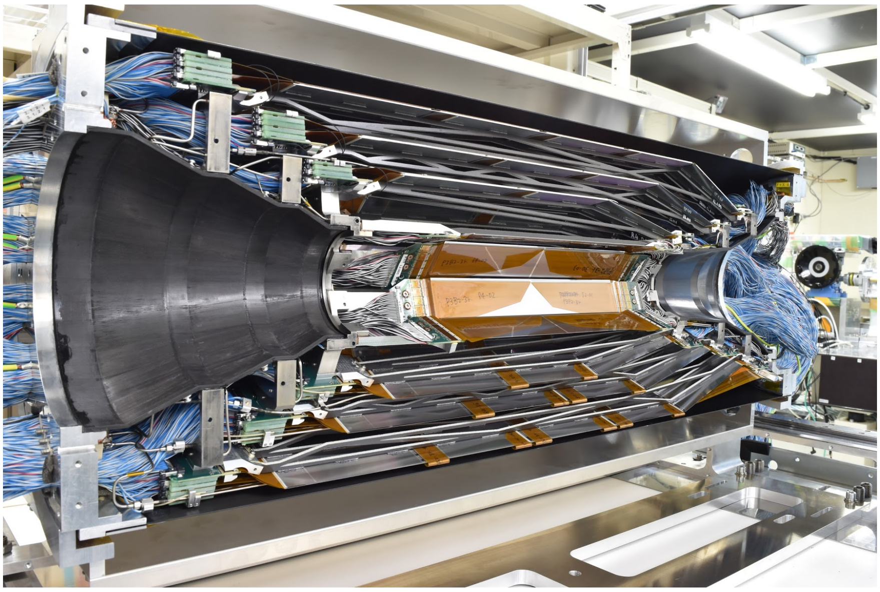

Figure 6: *The final SVD layout of Belle II experiment*

The Silicon Vertex Detector(SVD)[6] design consists of four layers of double sided silicon strip sensors fabricated from six-inches silicon wafers. The sensors are used to assemble slices of each layer, called 'ladders', which are then organized in a barrel geometry, with slanted sensors in the forward region to maximize angular acceptance. The final SVD layout is shown in the drawing in Fig.6.

The SVD, along with the PXD and CDC, enables the reconstruction of charged particle trajectories from B-meson decays. It also helps to estimate energy loss as charged particles pass through sensors, aiding in particle identification.

The SVD's "Origami concept" uses a three-layer Kapton flexible circuit to place read-out chips on the same side of the sensors, reducing material and maintaining precision. Layer 3 ladders have external electronics, while layers 4-6 use internal electronics to handle high radiation. The APV25 chip, selected for its speed and radiation resistance, ensures optimal performance despite assembly challenges.

An important feature of the SVD is its ability to reduce the large amount of data from the PXD, which would be difficult to read out quickly. SVD data can track charged particle trajectories in real-time, helping to identify the region where a particle likely interacted with the PXD. Only data from this "Region of Interest" (ROI) is then read out, optimizing the process.

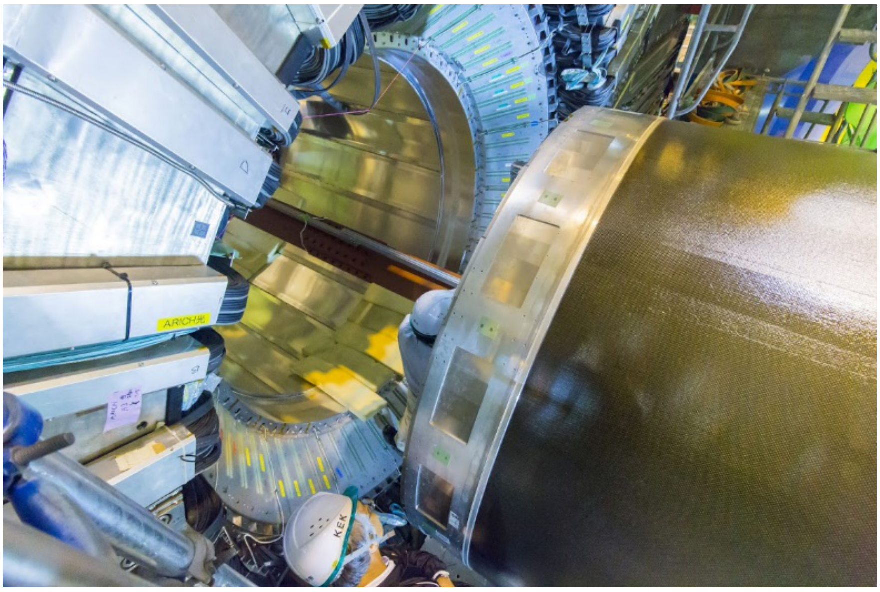

Figure 7: *The Belle II Central Drift Chamber(CDC*

The Belle II Central Drift Chamber(CDC, Fig.7) detects charged particle and measures its momentum under magnetic field. The CDC also provides pulse height information of the charged particle to identify particle species.

The CDC features over 50,000 wires, including 30um tungsten wires and 120um aluminum wires, arranged between forward and backward endplates supported by cylindrical walls. These wires are coaxially strung to form rectangular "cells" measuring approximately 1.8 cm x 1.8 cm.

CDC cells function as proportional chambers, where the signal pulse height correlates with the particle's energy loss. The "drift time" measures the distance between the position of the particle and the sense wire. These positions are used to reconstruct the track of the particle.

1.2.2 Electromagnetic Calorimeter

The Electromagnetic Calorimeter (ECL, Fig.8) for the Belle II experiment reuses the original Belle detector ECL with upgraded readout electronics. It consists of 8,736 CsI(Tl) crystals, each $6{\times}6{\times}30cm^3$, and detects photons and particles π^0 from the decays of the B-meson. The ECL covers a polar angle from *12°* to *155°* and provides fine granularity for high-precision measurements. CsI(Tl) crystals emit light with a wavelength of 560 nm, read out by two sets of silicon PIN photodiodes connected to charge-sensitive preamplifiers.

The ECL's energy resolution is crucial for distinguishing signal and background events, especially in high-energy collisions. The readout system is designed to handle a much higher trigger rate in Belle II (100 times higher than Belle). To manage radiation damage and prevent deadtime, waveform sampling and pipelined readout are used. The system's core is a Shaper Digitizer board that processes signals from 16 crystals, digitizes them, and stores them in a buffer. The upgraded system is expected to reduce cluster fake rates by a factor of seven.

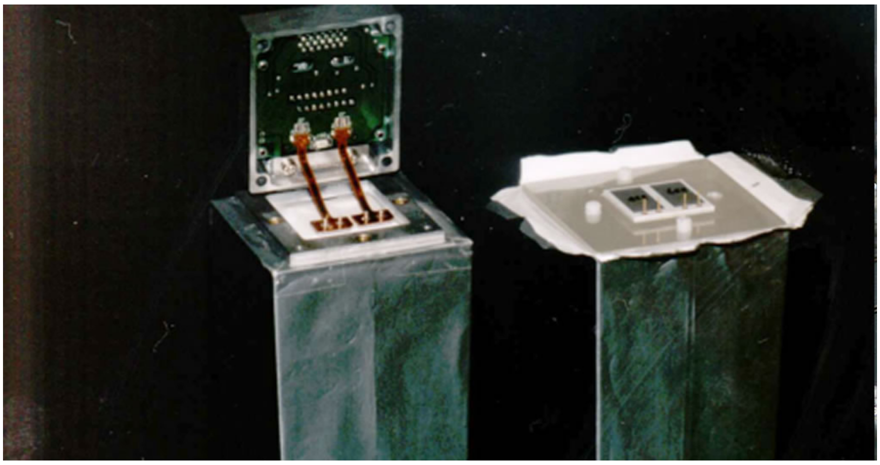

Figure 8: *The Electromagnetic Calorimeter (ECL) for the Belle II experiment*

In the forward region, pileup can affect energy and time resolution. Replacing some crystals with pure CsI could improve this, as pure CsI has a faster decay time (30 ns). The readout of pure CsI crystals will likely use phototubes, with ongoing research into using Avalanche Photodiodes (APDs) for their smaller size and redundancy in readout. APDs are less sensitive to magnetic fields but more sensitive to temperature variations and have a lower gain than phototubes.

1.2.3 Muon detection

The muon is an elementary particle similar to the electron but 207 times heavier. Because of its greater mass, a muon loses much less energy as it moves through matter and can penetrate much deeper than an electron. K_L (K-long) is a neutral kaon (K^0) that decays into three pions. Due to their long lifetime, the K_L particles pass through the detector without being detected. Both muons and K_L particles are known to travel long distances within the Belle II detector.

To identify muons and K_L particles, the largest subdetector in Belle II, KLM (K-Long-Muon), is used. It is positioned in the gaps of the magnet yoke. Due to the distance between the interaction point and the metal in the yoke, only muons and K_L particles can penetrate and reach the KLM effectively.

KLM consists of a barrel section with 15 layers and two endcaps, with 14 and 12 layers in the forward and backward directions, respectively. The inner two barrel layers and both endcaps are equipped with scintillator strips, while the outer 13 barrel layers are equipped with Resistive Plate Counters (RPCs).

A typical muon passes through all KLM layers, leaving a clear trail of hits. A K-long particle, on the other hand, interacts with an iron nucleus, producing debris that creates a concentrated cluster of hits in KLM.

1.2.4 Trigger and Data Acquisition

To select and store interesting events while reducing the data flow, the Belle II experiment uses a high-performance trigger and data acquisition system.

The Belle II detector generates data from several hundred kilo channels every 8 nanoseconds, which is too much to record continuously. Since subdetectors don't know when a physics event occurs, data is briefly stored in a buffer for just 5 microseconds before older data is discarded. The Level 1 (L1) Trigger system, implemented on FPGA-based readout boards, extracts only relevant physics data from this continuous flow. It has background separation power to filter events at a maximum rate of 30 kHz, while ensuring 100% detection efficiency.

The L1 trigger analyzes data from CDC, ECL, TOP, and KLM detectors within a 2 to 4 microsecond window after beam crossing to detect physics events, signaling the DAQ system to record the desired data.

With the increased luminosity of SuperKEKB, managing the data flow is a challenge. The data acquisition system uses cutting-edge technology to process, reduce, and store data for later analysis.

1.2.5 Particle-Identification

Particle Identification detectors allow using the information left by the particles passing through them, to identify the type of particle.

A barrel-shaped array of Time-Of-Propagation (TOP) counters reconstructs in spacial and time coordinates, the ring-image of Cherenkov light cones emitted from charged particles passing through quartz radiator bars.

The Time-Of-Propagation (TOP) counter in the Belle II detector distinguishes pions from kaons, crucial for identifying B meson decays.

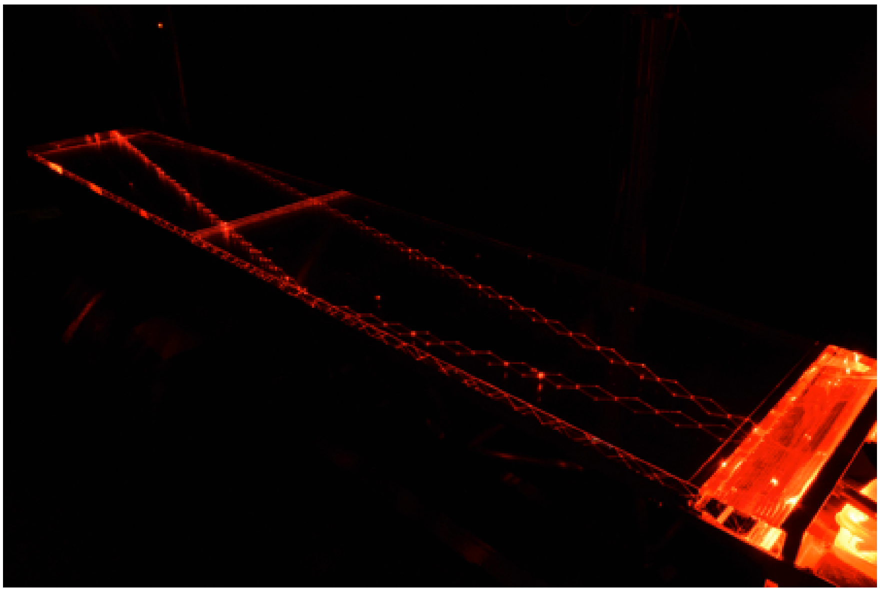

Figure 9: *Long time exposure with laser input from prism end in the Belle II experiment*

The core of this detector is a 2-cm thick quartz bar, polished to an extremely flat surface with roughness under 5 angstroms (about the size of 5 atoms). When a charged particle, like a pion or kaon, passes through the quartz, it emits Cherenkov light at a specific angle relative to the particle's direction. This light reflects internally along the bar to the end, where its arrival time is measured. Due to slight differences in the Cherenkov light's angle, the path length to the photodetector varies between pions and kaons, leading to a small time difference in light arrival. These differences are precisely measured by Micro Channel Plate

Photo Multiplier Tubes (MCP-PMTs), which offer an unprecedented timing precision of 50 picoseconds. This precision allows the detector to distinguish between pions and kaons based on their light arrival times.

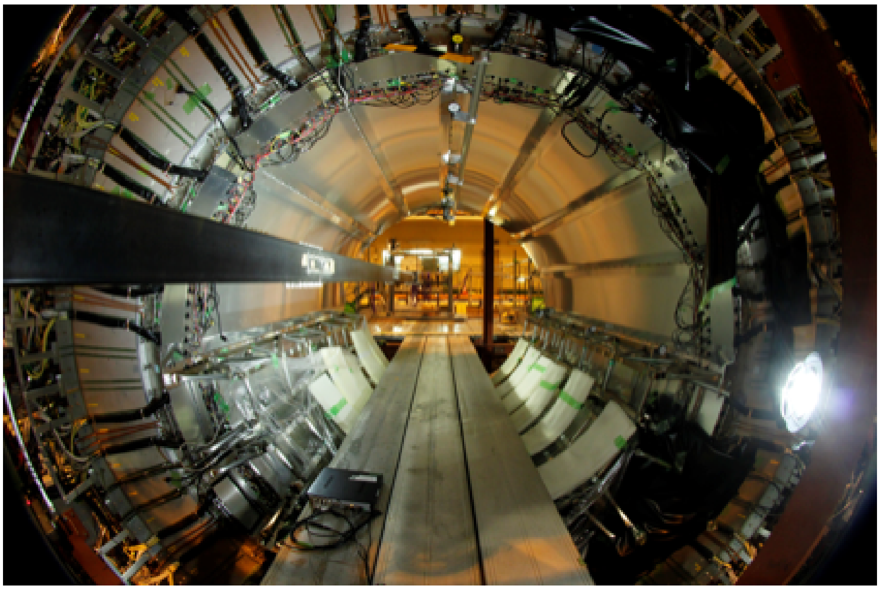

Figure 10: *All 16 modules installed in the Magnet in the Belle II experiment*

The detector comprises 16 identical modules Fig.10, each containing a 2.5-meter-long and 45-centimeter-wide quartz bar. Since Cherenkov light is weak and can be easily lost due to dust, the modules were manufactured in a clean room environment (as shown in the photos). The modules are arranged in a barrel configuration with a 1.2-meter radius, covering the entire inner surface of the electromagnetic calorimeter (ECL).

Another ring-imaging Cherenkov counter with aerogel radiator in the forward end-cap (A-RICH), is used to identify charged particles in the front-end endcap region of the Belle II spectrometer. Its main objective is to separate kaons from pions in the full kinematical region of the experiment (about 0.5-4.0 GeV). About ARICH we will talk in the next section.

2 The Aerogel RICH counter

In this chapter, the principle of the RICH counter and the design of the Belle II ARICH counter will be described. Efficient identification of long-lived charged particles plays an important role in B-tagging and in studies of rare decays. The performance of the charged particle identification is evaluated in terms of correct identification and misidentification probabilities. Efficiency is defined as a fraction of correctly identified particles among all reconstructed particles of the same type. The misidentification probabilities, on the other hand, give information about the fraction of particles that are incorrectly identified as particles of some different type [7].

2.1 Cherenkov Radiation

The dedicated particle identification Cherenkov counters detect charged particles through the effect of Cherenkov radiation. Cherenkov radiation arises when a charged particle moves in a dielectric material faster than the light travels in the same material. The speed of light in a material v_{light} is

$$v_{light} = \frac{c_0}{n}, \tag{1}$$

where c_0 is the speed of light in vacuum and n is the refractive index of the medium. The refractive index indicates how light travels through a medium, and its value is equal to or greater than 1 in the optical range.

When a charged particle moves through a dielectric material, it temporarily polarizes the molecules along its path. As the induced dipoles return to their stable initial states, photons are emitted in the process.

When the charged particle travels slower than c_0/n, the polarization (Fig.11) is symmetrical and radiation is not seen due to destructive interference. But when a particle travels faster than c_0/n, the polarization is asymmetrical, resulting in constructive interference, seen as the creation of an electromagnetic shock wave [8].

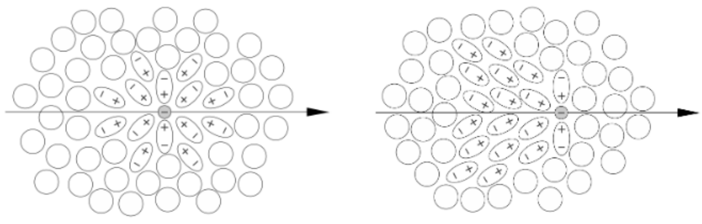

Figure 11: *: Polarization in dielectric material, induced by a charged particle, traveling through the medium with a speed lower (a) and greater (b) than the speed of light in the same medium [9]. When the particle is faster than light, polarization becomes asymmetrical and creates a dipole field*

An electromagnetic shock wave forms as shown in Fig.12. While the particle travels over a distance vt, the shock wave moves over a distance of $\frac{c_0}{n}t$. The angle, by which photons are emitted – Cherenkov angle θ_{ch} is measured relatively to the particle trajectory and is defined with

$$\cos\theta_{ch} = \frac{1}{vt}\frac{c_0 t}{n} = \frac{1}{\beta n}, \tag{2}$$

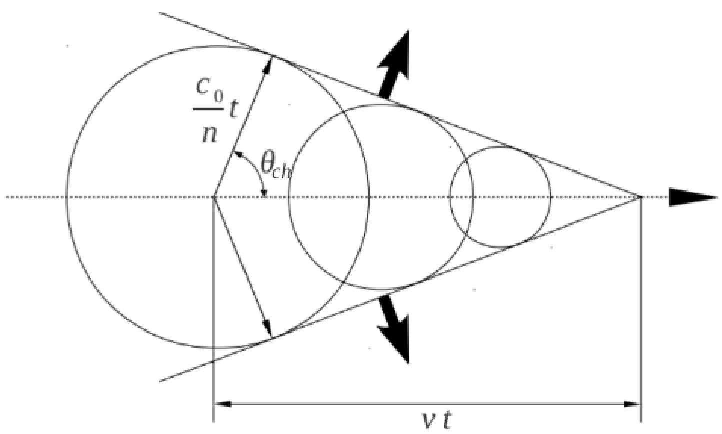

Figure 12: Cherenkov radiation. *An electromagnetic shock wave is created when a charged particle travels faster than light in a medium. The coherent wavefront is emitted at well-defined Cherenkov angle θ_{ch}*

The maximum Cherenkov angle, when a particle travels at the speed of light, is therefore:

$$\theta_{ch,max} = \arccos{(n^{-1})}, \tag{3}$$

The number of emitted photons depends on the charge of the particle, z, the refractive index of the medium, n, and the thickness of the material, l. It can be calculated as[10]:

$$N_{emmited} = \frac{2\pi\alpha z^2}{hc} l \int_{E_1}^{E_2} \sin\theta_{ch}(E) dE, \tag{4}$$

where E_1 and E_2 are the limits of the optical photon energy interval and α is a fine-structure constant $\alpha = \frac{2\pi e_0^2}{4\pi\epsilon_0 hc_0} \approx \frac{1}{137}$.

2.2 Principle of Belle II ARICH

The Belle II spectrometer is equipped with two Cherenkov detectors. In both detectors, charged particles are identified (indirectly) on the basis of their mass m, which can be determined from the relationship between their momentum p and velocity v. The momentum is derived from the curvature radius of the particle's trajectory in a magnetic field, whereas the velocity is measured using Cherenkov radiation.

The fundamental operating principle of all Cherenkov detectors is consistent. They require a radiator material where Cherenkov photons are produced along with a medium where these photons can travel (often aided by mirrors or lenses to focus the photons). In addition, sensors are needed to detect photons. The design and choice of materials for the detector are determined by factors such as spatial constraints, desired signal resolution, and the need to differentiate between particles across a specific momentum range. In particle physics, momentum is typically used in place of velocity, so the focus is on the relevant momentum range for operation.

A momentum threshold for emitting Cherenkov radiation can be expressed using the equation for relativistic momentum $p = mv/\sqrt{1 - v^2/c_0^2}$, and the relation between the momentum and the refractive index (Eq.1) as

$$p_{th} = \frac{mc_0}{n\sqrt{1 - \frac{c_0^2}{n^2 c_0^2}}} = \frac{mc_0}{\sqrt{n^2 - 1}}, \tag{5}$$

The Cherenkov angle is influenced by both the velocity of the charged particle and the refractive index of the radiator (see Eq.2). Fig.13 shows how the Cherenkov angle varies with momentum for different particles emitted in the aerogel, demonstrating that the range for efficient particle identification is limited. This threshold can be adjusted across a wide momentum range by selecting an appropriate radiator. With solid radiators, it is possible to distinguish kaons from pions at momenta as low as several tens of MeV/c, and with gaseous radiators, this can extend up to 100 GeV/c.

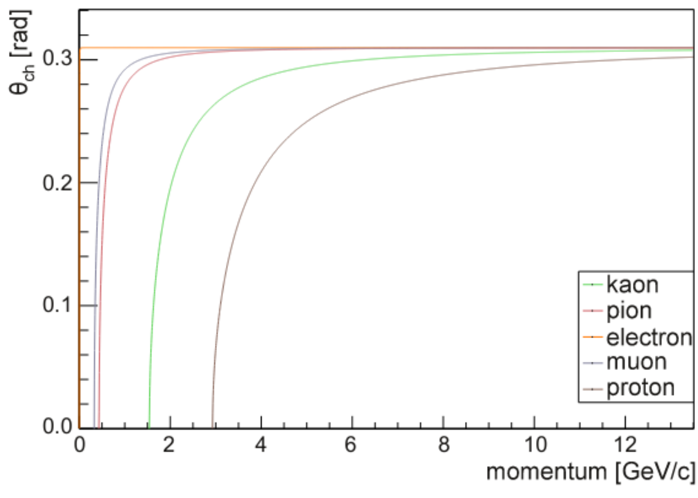

Figure 13: *A comparison of Cherenkov angle as a function of momentum for photons, emitted within the aerogel radiator with n = 1.05 by five different charged particles*

There are various types of Cherenkov detectors, which are typically classified as threshold or imaging counters. Threshold counters are capable of distinguishing between two charged particles but operate within a narrow momentum range defined by two momentum thresholds. Imaging counters can be further categorized into differential Cherenkov detectors and ring-imaging Cherenkov detectors. Differential Cherenkov detectors function within a very limited momentum range; they detect photons from one type of particle at a specific momentum, while photons from the other particle, emitted at a different angle at the same momentum, do not reach the sensor. In contrast, only ring-imaging Cherenkov detectors are sensitive across a broader momentum range.

The main components of ARICH are a double layer aerogel radiator for Cherenkov photon emission, an empty space for a Cherenkov light-cone expansion, the Hybrid Avalanche Photo-Detector($HAPD$) sensor plane and the read-out electronics, which were developed for the Belle II experiment [11]. A schematic depiction of the ARICH detector and its operation is shown in Fig.14.

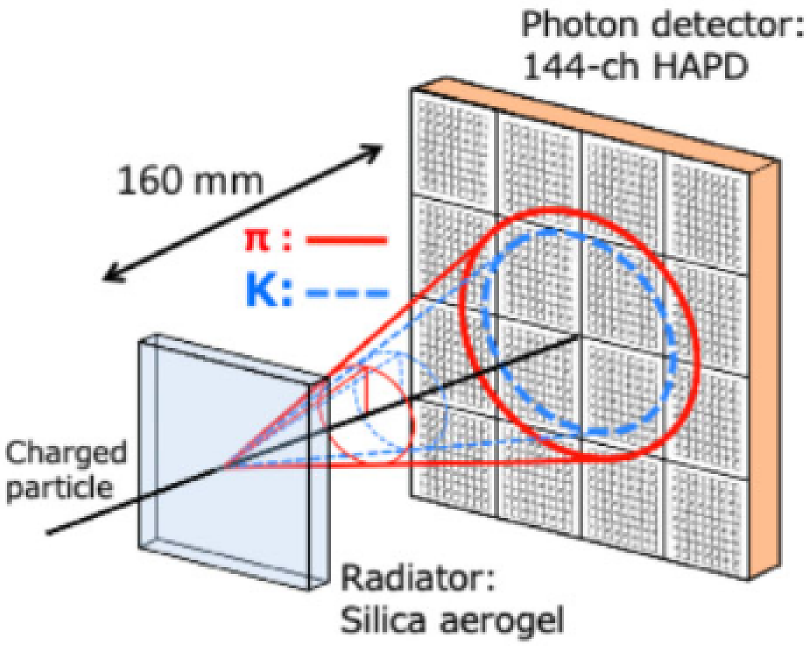

Figure 14: *The principle of the particle identification with the ARICH counter*

2.3 Design of Belle II ARICH

The ARICH counter is comprised of three main components: the silica aerogel radiators, the HAPD photo-sensors and the readout electronics.

2.3.1 The radiator

The radiator needs to have a large transmission length and an appropriate refractive index. The refractive index must ensure that the ring radius is several decimeters, emitting a sufficient number of photons while preventing total reflection at the interface between the radiator and air. Selecting the refractive index of silica aerogel involves balancing both the emission of Cherenkov photons and the transmission length considerations.

Generally, transmission decreases with respect to the refractive index. A shorter transmission length results in the loss of emitted photons, necessitating a longer transmission length. The maximum transmission length is typically found around a refractive index of 1.03, and remains sufficiently high ($> 20mm$) at a refractive index of 1.05. Therefore, ARICH chooses 1.05 as a refractive index of the radiator [12].

A dual-layer scheme is adopted to improve angle resolution without reducing the number of detected Cherenkov photons [13],[14],[15]. By optimizing the two distinct refractive indices, Cherenkov photons are focused onto the photon detector plane, producing a compressed ring image as illustrated in figure 15. We have selected refractive indices of 1.045 for the upstream aerogel tile and 1.055 for the downstream aerogel tile. The threshold momenta to emit the Cherenkov photons are 0.44 [GeV/c] for pions and 1.54 [GeV/c] for kaons with a refractive index of 1.05.

The ARICH counter employs large-area silica aerogel tiles known for their extensive transmission capabilities [16],[17],[18]. To ensure maximum overlap of the ring image, the refractive index difference between upstream and downstream tiles must be carefully adjusted. Currently, the refractive index difference in installed tile pairs ranges from 0.0095 to 0.0104, which falls within our required range of 0.008 to 0.012 [12].

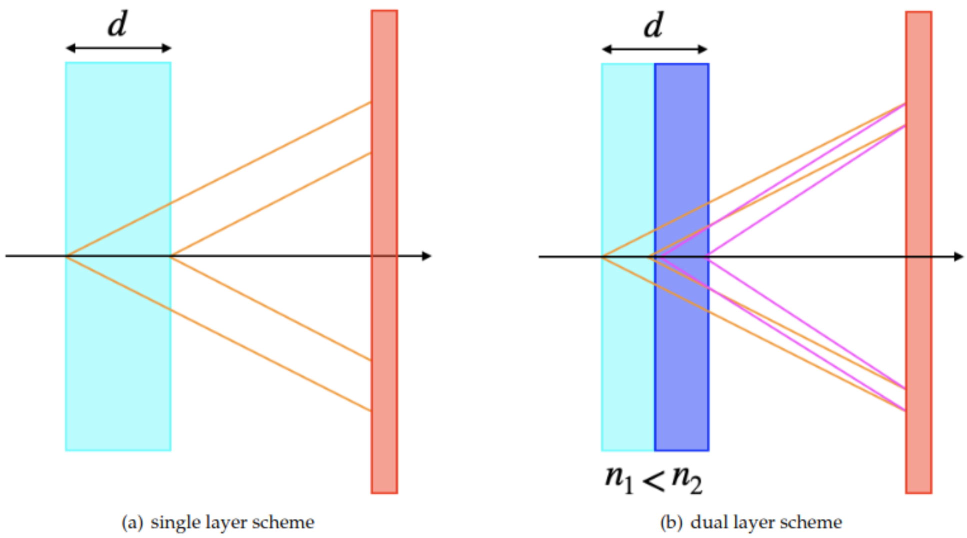

Figure 15: *The conceptual diagram of the radiator design. (a) single layer scheme and (b) dual layer scheme.*

2.3.2 Photon detector

The ARICH photon detector has the following properties [2]:

- Capable of detecting single photons, with each pad size smaller than $5mm.$;
- tolerance to the high magnetic field ($B = 1.5T$);
- a sufficient radiation hardness to endure the 10-year operation of Belle II, withstanding a radiation dose of 100 Gy and neutron fluency equivalent to $10^{12}[MeV]$ neutrons per cm^2.

The HAPD (Fig.16)developed by Hamamatsu Photonics K.K. meets our requirements as a photon detector [19, 20, 21]. Its specifications are detailed in Table 1. The HAPD consists of a quartz window with a photo-cathode, housed within a vacuum tube, and incorporates four Avalanche Photo Diode (APD) chips. Each APD chip is divided into 6×6 pixels, each with dimensions of $4.9 \times 4.9[mm^2]$,

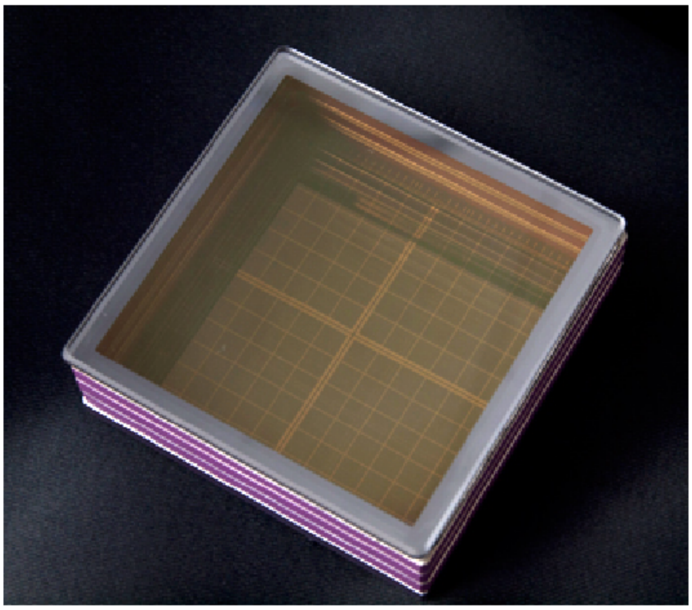

Figure 4.17: A Hybrid Avalanche Photo Detector (HAPD).

Figure 16: *A Hybrid Avalanche Photo Detector (HAPD).*

resulting in a total of 144 channels per HAPD. Photon detection in the HAPD occurs through two main steps: bombardment of a photo-electron figure 17(a) and avalanche amplification in the APD chip figure 17(b).

Size	$73 \times 73 \times 28\ mm^3$
Number of APD chips	$2 \times 2 = 4$ chips
Number of channels	$12 \times 12 = 144$ ch
Channel size	$4.9 \times mm^2$
Effective area	65 %
Photo-cathode material	Bialkali
Quantum efficiency	$\sim$ 28% at 400 nm
Bombardment gain	$\sim$ 1800
Avalanche gain	$\sim$ 40
Total gain	72000
Capacitance	80 pF

Table 1: *The specification of the HAPD.*

The photo-electrons are accelerated in a high electric field by applying a negative high voltage to the photo-cathode, generating approximately 1800 electron-hole pairs within the APD. Each electron in the depletion region creates around

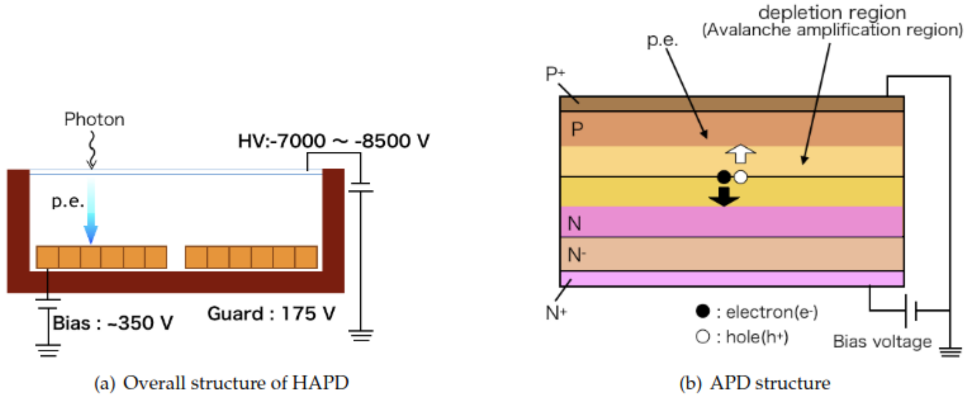

Figure 17: *The mechanical structure of HAPD. (a) overall structure of HAPD and (b) APD structure in HAPD*

40 electron-hole pairs as a result of the reverse bias voltage applied to the APD. Consequently, the total gain of the HAPD is approximately 72,000. To control an HAPD, three types of power supplies are required: a negative high voltage ($HV \times 1 : 7 - 8kV$), for accelerating photo-electrons, reverse bias voltages ($Bias \times 4 : around 350V$) for each APD, and a common guard voltage ($Guard \times 1 : 175V$) for the APDs. Therefore, six power supply inputs are necessary per HAPD. In total, 420 HAPDs are arranged in seven concentric rings with varying numbers of detectors: 42, 48, 54, 60, 66, 72, and 78 detectors per ring.

The figure 18 displays both one-dimensional and two-dimensional distributions of the average quantum efficiency at $400nm$ for all installed HAPDs [22]. The mean quantum efficiency of the installed HAPDs is 32.2% . These HAPDs are randomly distributed throughout the photon detector plane to mitigate any position-dependent variations in the detection efficiency for Cherenkov light.

2.3.3 Readout electronics

The readout electronics for the ARICH system comprise Front End Boards (FEBs) and Merger Boards (MBs) [22, 23, 24]. Each FEB is directly connected to the HAPD and is equipped with four Application Specific Integrated Circuit

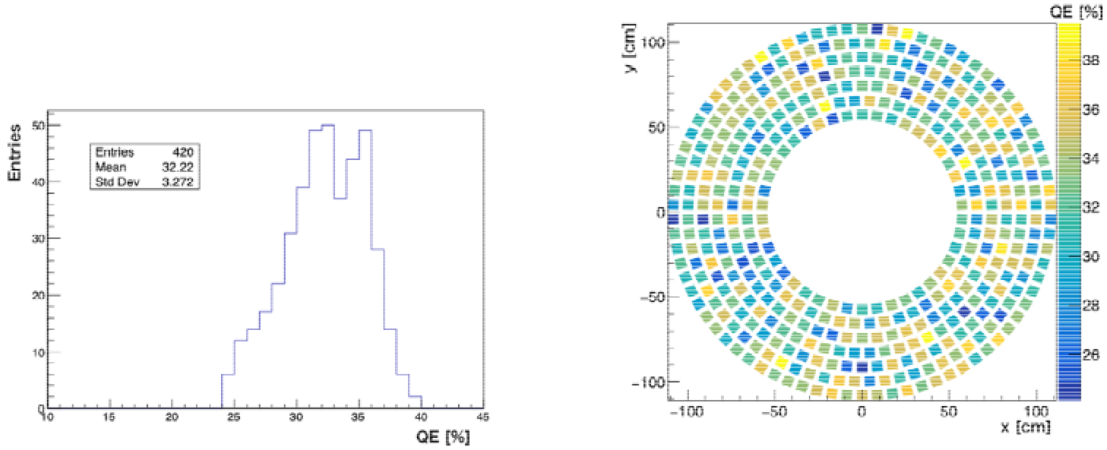

(a) One-dimensional distribution (b) Two-dimensional distribution

Figure 18: *One (a) and two (b) dimensional distributions of quantum efficiency of installed HAPDs. The quantum efficiency for each HAPD is arranged over the photo sensitive area.*

(ASIC) chips specifically developed for HAPD readout [25]. These ASIC chips continuously amplify, shape, and discriminate 36 signals originating from a quarter of the HAPD. In the ARICH system, the primary function is to measure the ring image, and only hit information is collected. Up to six FEBs are linked to one MB. The MB then serializes the data received from the FEBs and suppresses data from channels that have not recorded hits, effectively reducing the overall data size.

The MBs transmit merged data to the back-end Belle II central data acquisition system. Each MB is equipped with two RJ45 connections for trigger and Joint Test Action Group (JTAG), as well as an optical fiber connector for data acquisition and FEB configuration. The configuration settings for the FEBs are managed via the MBs. Both the Front End Boards (FEBs) and MBs utilize a field-programmable gate array (FPGA) responsible for facilitating communication between the boards and the back-end data acquisition electronics. In total, the ARICH system comprises 420 FEBs and 72 MBs, handling a total of 60,480 channels.

2.3.4 Aerogel

Aerogel is an extremely lightweight material known for its high optical transparency. Its structure resembles that of a gel, but the liquid component is replaced by gas. Aerogels vary depending on factors such as molecular structure, density, water interaction, and more. The properties of aerogel are determined during its synthesis, which involves three main steps:

- Gel preparation (gelation of the source solution)
- Aging of the gel (adding the strength to the gel structure)
- Drying of the gel (carefully removing the liquid

The refractive index of the aerogel, typically ranging from 1.003 to 1.11, can be finely adjusted during the synthesis process, making it ideal for a variety of applications, including Cherenkov detectors [26],[27]. A silica aerogel is composed of nanoscale molecules that are connected by numerous siloxane (Si-O-Si) bridges, which aggregate to form larger structures.

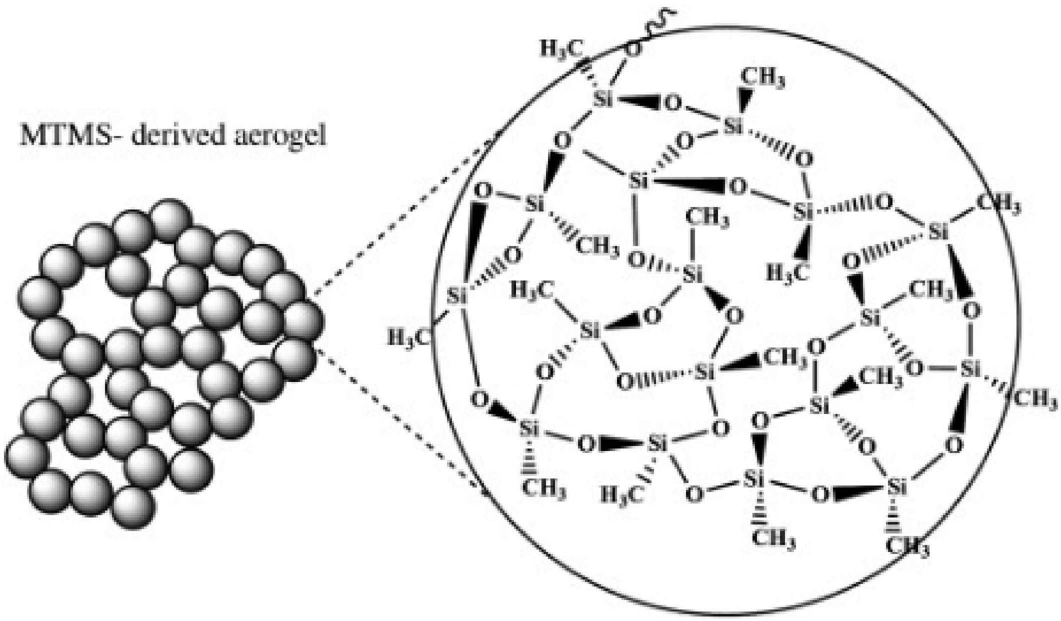

Figure 19: *Condensed formula of a silica aerogel .*

3 ARICH performance

3.1 PID method

Charged particle identification (PID) is accomplished by a time-of-propagation counter and an aerogel ring imaging Cherenkov counter located in the barrel and forward-endcap regions, respectively. The CDC provides additional PID information through the measurement of specific ionization. PID information from all relevant sub-detectors is combined to separate final states into exclusive samples and to further reduce backgrounds. [28].

For each charged track passing through ARICH, the value of the likelihood function [29, 30, 31, 32] is evaluated for six particle hypotheses: electron, muon, pion, kaon, proton, and deuteron. This thesis was based on [29, 30, 31, 32] papers, where *Global PID* was intensively used to obtain physical results for this paper. The likelihood function for a particle hypothesis h is defined as:

$$L_h = \prod_{allpixel} p_{h,i}(m_{h,i}); \quad p_{h,i}(m_{h,i}) = \frac{e^{-n_{h,i}} n_{h,i}^{m_{h,i}}}{m_{h,i}!}, \tag{6}$$

where the product runs over all pixels of the whole ARICH counter, and $p_{h,i}(m_{h,i})$ is the probability of observing $m_{h,i}$ hits on the i-th pixel, while $n_{h,i}$ hits are being expected on average (for an assumed hypothesis h) [1, 2]. Since there is no discrimination of multiple-photon from single-photon hits in ARICH, $p_{h,i}(m_i)$ can be rephrased as

$$p_{h,i}(nohit) = e^{-n_{h,i}}, \tag{7}$$

$$p_{h,i}(hit) = 1 - p_{h,i}(nohit) = 1 - e^{-n_{h,i}}, \tag{8}$$

Using eq. 7 and eq. 8, eq. 6 can be rewritten as PID method

$$lnL_h = -N_h + \sum_{hit_i} [n_{h,i} + ln(1 - e^{-n_{h,i}})], \tag{9}$$

where N_h is the expected total number of hits, and the sum runs over pixels that were hit. The global logarithms of the likelihood ratios [33] are defined as:

$$R_h = \frac{lnL_h}{lnL_K + lnL_\pi + lnL_\mu + lnL_e + lnL_p + lnL_d} \tag{10}$$

The separation between kaons and pions is performed by imposing selection criteria on the logarithms of likelihood ratios (see Eq. 9) which are defined as

$$R_{K/\pi} = \frac{lnL_K}{lnL_K + lnL_\pi} \tag{11}$$

$$R_{\pi/K} = \frac{lnL_\pi}{lnL_K + lnL_\pi} \tag{12}$$

Charged kaon and pion candidates are identified on the basis of information from PID detectors and the specific ionization measured in the drift chamber. We use the ratio $L_{K/\pi} \equiv L_K/[L_K + L_\pi]$ to identify the type of charged particles, where L (h) is the probability that a kaon or pion will produce the signals observed in the detectors. Charged particles with $L_{K/\pi} > 0.6$ are identified as kaons and those with $L_{\pi/K} > 0.6$ as pions.

3.2 Probability density function

The PDF is constructed from two parts: track-correlated and uncorrelated components. First, the track-correlated part is built as a function of the reconstructed Cherenkov angle, which corresponds to the Cherenkov angle for unscattered Cherenkov photons. The expected number of hits on a specific channel (denoted as ($n_{h,i}$)) is determined by projecting the correlated part of the PDF onto the photon-detector plane and integrating it over the surface of the pixel i. Additionally, the uncorrelated part of the PDF is added to this calculation [2].

The PDF is composed of the following components:

1. Cherenkov photons emitted in a silica aerogel.

   Cherenkov light is emitted when a particle traveling through the silica aerogel in ARICH exceeds the speed of light within the aerogel medium. This emission generates photons that produce two Gaussian peaks in the Cherenkov angle distribution, both centered around the expected Cherenkov angle. The primary narrow peak corresponds to non-scattered photons, while the broader peak describes photons that undergo Rayleigh scattering within the silica aerogel. Additionally, photons passing through the photo-cathode and being reflected from the APD surface contribute to this broader peak. The sizes of both peaks correlate with the expected number of photons emitted in the aerogel. Their widths and relative contributions are established by fitting observed Cherenkov angle distributions derived from control samples. Different expected numbers of emitted photons are assigned to each aerogel layer on the basis of its specific characteristics within the ARICH setup.

2. Track-correlated background sources Cherenkov photons are also emitted when a particle traverses the quartz window of an HAPD. Some photons

are promptly converted into photoe-electrons, forming a Gaussian peak around the incident point of the track. Others undergo multiple total internal reflections within the quartz window before being converted into photoe-electrons. These photons contribute to the PDF at small Cherenkov angles. The latter component is determined separately based on whether the extrapolated track intersects the quartz window or not, as this distinction significantly affects the photon's path. These contributions follow an exponential distribution combined with either a second- or first-order polynomial function depending on whether the extrapolated track enters the quartz window or not.

3. Random background sources

   Random background in the ARICH system can arise from various sources such as beam background, Cherenkov photons emitted by other tracks, hits due to electronic noise, dark counts from HAPDs, and more. This background is not correlated with any specific track and is modeled as a uniform distribution across the photon-detector area. The level of this random background is determined on the basis of the average number of off-time hits per channel per event.

3.3 Efficiency determination

The registration efficiency of the ARICH detector as well as the misidentification probability as a function of a particle momentum and polar angle are very important characteristics for any Particle Identification Detector (PID) in measuring physical observables such as the cross section, branching fractions, and others. The typical approach to calculate the efficiency is based on the usage of well-known resonance decays with pions, kaons, and protons in the final state. For the performed studies, the decays of $D^{*+} \to D^0 + \pi^+$ and $D^{*-} \to \bar{D}^0 + \pi^-$ were used. Performing the fitting of the invariant mass spectrum formed by decaying particles and applying the requirements on the invariant mass to be within the window of fitted values of resonance mass and width, one can determine a hadron type in the final state with the highest probability. Identification performance is discussed in terms of identification efficiency ϵ and the mis-identification probability η. Both are determined as a ratio of the number of reconstructed D^* decays obtained with and without the identification selection criteria applied, i.e.:

$$\epsilon_K = \frac{number\ of\ K\ tracks\ after\ R_{K/\pi} > R_{cut}}{number\ of\ K\ tracks} \tag{13}$$

$$\epsilon_\pi = \frac{number\ of\ \pi\ tracks\ after\ R_{\pi/K} > R_{cut}}{number\ of\ \pi\ tracks} \tag{14}$$

$$\eta_K = \frac{number\ of\ K\ tracks\ after\ R_{\pi/K} > (R_{cut})}{number\ of\ K\ tracks} \tag{15}$$

$$\eta_\pi = \frac{number\ of\ \pi\ tracks\ after\ R_{K/\pi} > (R_{cut})}{number\ of\ \pi\ tracks}, \tag{16}$$

where $R_{\pi/K}$ and $R_{K/\pi}$ are defined by Eq.(11, 12) and R_{cut} is fixed after dedicated studies with typical values $R_{cut} = 0.6$.

4 Dataset

4.1 Event selection

We use the $D^{*\pm} \to D^0(\bar{D}^0)\pi^\pm \to (K^\mp\pi^\pm)\pi^\pm$ decays to evaluate the performance of particle identification. This decay can be reconstructed with a relatively low background. The fraction of decay $D^{*\pm} \to D^0(\bar{D}^0)\pi^\pm$ is $(67.7 \pm 0.5)\%$. Meanwhile, the fraction of $D^0(\bar{D}^0) \to K^\mp\pi^\pm$ is $(3.947 \pm 0.030)\%$.

To reconstruct $D^{*\pm} \to D^0(\bar{D}^0)\pi^\pm \to (K^\mp\pi^\pm)\pi^\pm$ decays, certain kinematic and geometric pre-cuts were applied to the decay products. First, we fix a certain invariant mass range for the $D^0(\bar{D}^0)$ particles that require them to be in a $1.77 < M_{D^0} < 1.97$ mass window. To fix the invariant mass range for the $D^{*\pm}$ particles we use $0.0 < Q < \mathit{0.01\ GeV}$ cut. The Q variable applied is the decay energy released that connects the invariant masses $D^{*\pm}$ and $D^0(\bar{D}^0)$. It is the analog of the variable $|M(D^{*\pm}) - M(D^0\bar{D}^0) - 0.14543 < 0.0015|$.

Furthermore, we use general tracking recommendations to take only good tracks. The daughter pions of the $D^{*\pm}$ particles should satisfy the following requirements:

- $dr < 2[cm]$
- $|dz| < 4[cm]$
- *thetaInCDCAcceptance*

For daughter pions and kaons of $D^0(\bar{D}^0)$ particles, the restrictions are fallowing:

- $dr < 1[cm]$
- $|dz| < 3[cm]$
- *thetaInCDCAcceptance*

- *p (momentum)* > 0.3 *GeV*

where *dr* is the transverse distance with respect to the interaction point (IP) for a vertex and $|dz|$ is the vertex z with respect to IP. p is the momentum of a particle, and *thetaInCDCAcceptance* requires that all tracks be in CDC angular acceptance which is $17^{\circ} - 150^{\circ}$.

We also require that daughter pions of the decays $D^{*\pm}$ and $D^0(\bar{D}^0)$ have the same charge sign.

We are using exactly the same cut selection for both Data and MC samples.

4.2 Data selection

In the Belle II experiment, data collections without interruptions are called a *run*. Some amount of runs collected is called an *experiment*. Usually after big issues or shutdowns, the number of experiment is changes. It can also be related to the central mass energy change, but in our case we take only *experiments* with the mass energy of $\Upsilon(4S)$. Starting *experiment 20* was also implemented *Buckets* which are units smaller than *experimnets*. After collecting some amount of data, we can move to another *bucket*.

For this study, we used a subset of the Moriond 2023 dataset, the compositions of which are shown in Table. 2. Dataset was used with the exclusion of bad runs and the analysis was performed using $release - 06 - 02 - 12$.

Experiment number	Bucket Label	Integrated Offline Luminosity fb^{-1} proc13 & prompt
7	-	0.506 ± 0.002 ± 0.004
8	-	1.6630 ± 0.003 ± 0.011
10	-	3.655 ± 0.002 ± 0.024
12	-	54.573 ± 0.005 ± 0.350
14	-	16.500 ± 0.006 ± 0.106
16	-	10.294 ± 0.004 ± 0.066
17	-	10.715 ± 0.004 ± 0.069
18	-	89.900 ± 0.011 ± 0.576
20	26	3.788 ± 0.003 ± 0.025
22	28,29	32.060 ± 0.007 ± 0.206
24	30,31,4,33	85.642 ± 0.011 ± 0.549
26	35,36	54.795 ± 0.009 ± 0.351

Table 2: *Data sample used in the analysis*

The combined integrated offline luminosity for all the experiments used together is 368.091 fb^{-1}. In order to use the combined sample obtained together, there is a need to check the compatibility between different data samples.

Fig. 20 shows the invariant mass distributions for D^0 and $\bar{D}^0$ where different colors correspond to different experiments and normalization was performed through cross sections.

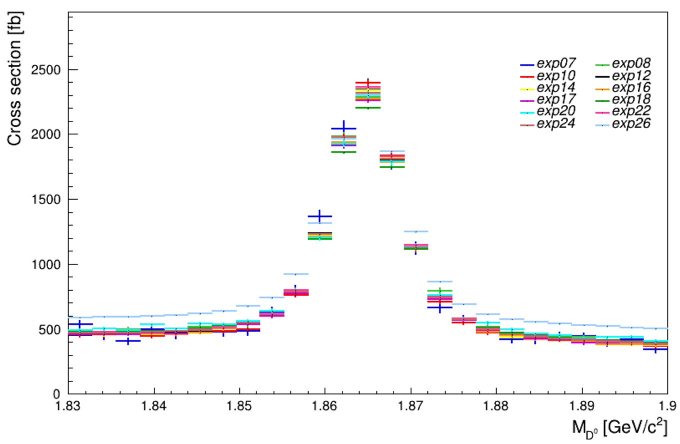

a

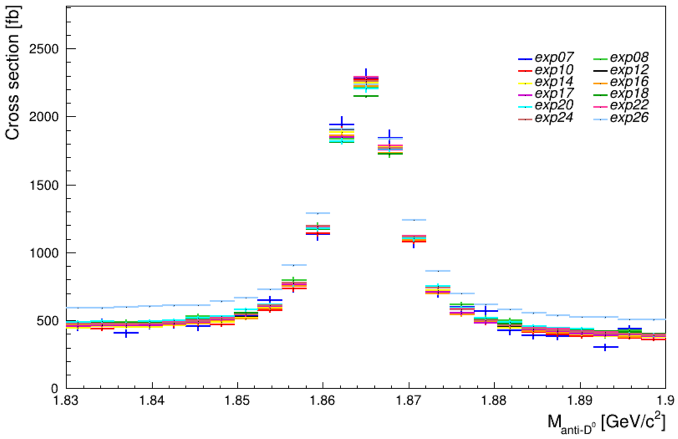

b

Figure 20: *The invM distributions for D^0 (a) and $\bar{D}^0$ (b).*

Moreover, Fig. 21 presents the invariant mass distributions for the particles D^{*+} and D^{*-}.

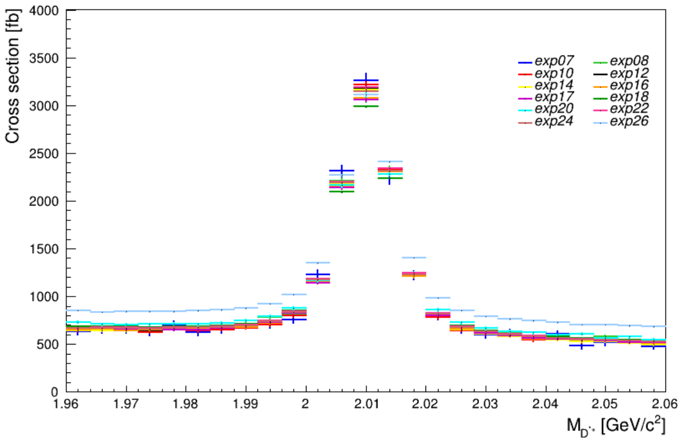

a

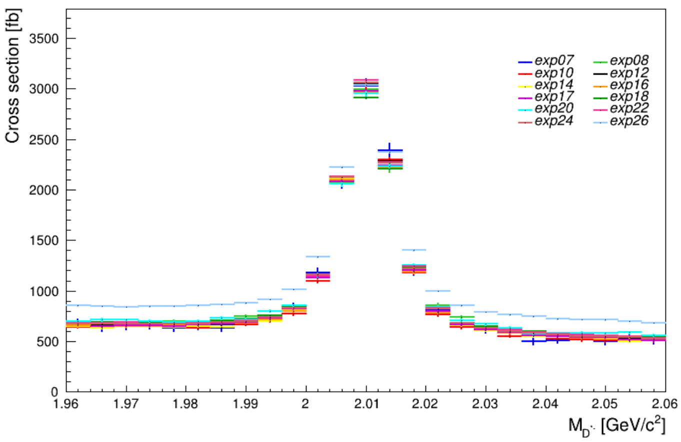

b

Figure 21: *The invM distribution for D^{*+} (a) and D^{*-} (b).*

More detailed comparisons between data samples with ratio plots were done. *exp18* was fixed as a check sample and a comparison of *exp18* was made with all the other *experiments*. Fig. 22 indicates the compatibility check for the particle D^0 between all the particle used *experiments*.

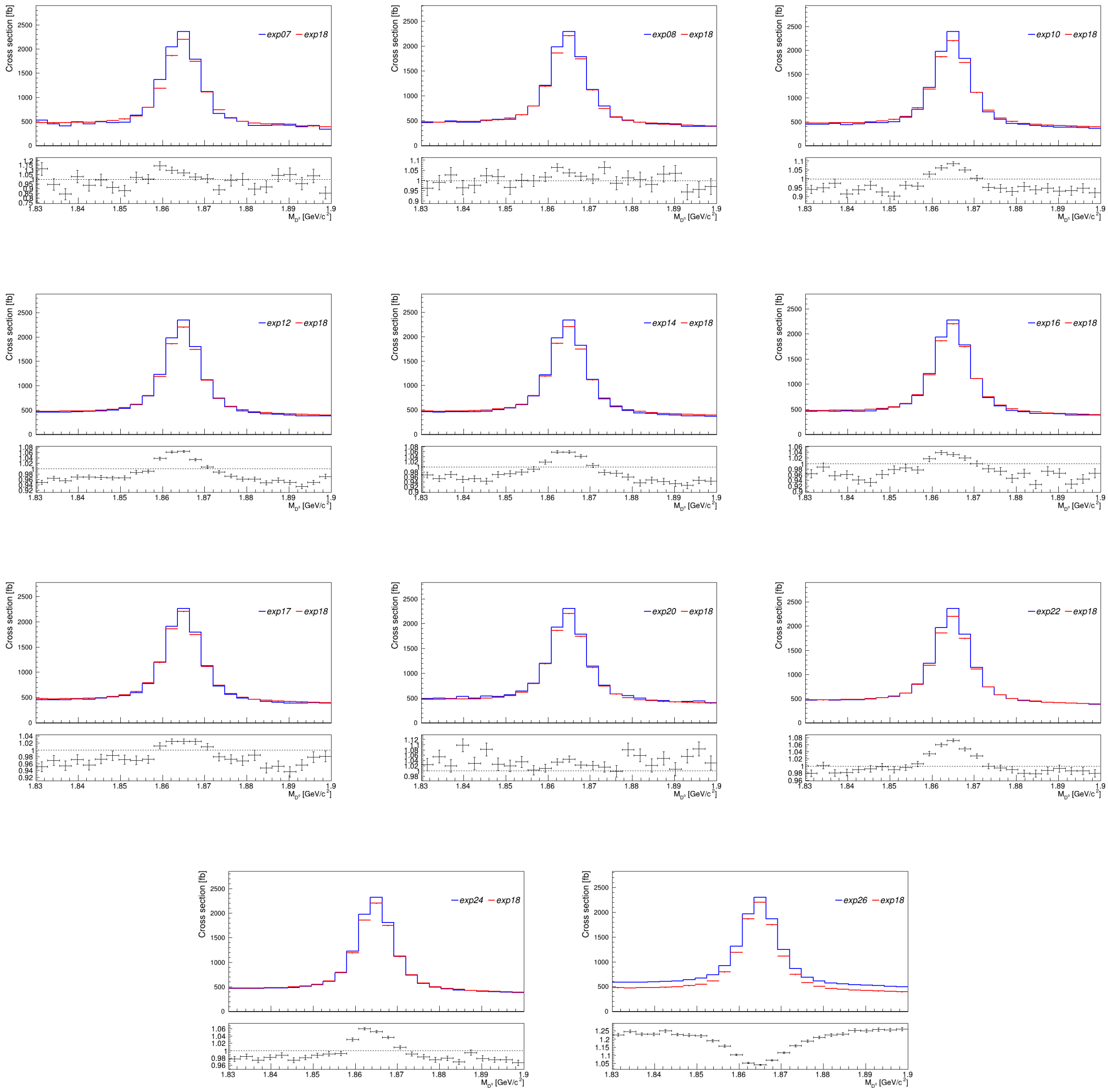

Figure 22: *Compatibility check between samples for* D^0

As we can see from the above obtained results, there is good agreement between different *experiment* samples, and a combined sample can be used. This check was also done for $\bar{D}^0$, D^{*+} ,D^{*-} particles, and good agreement was also observed between different data samples.

Furthermore, since the reconstruction of the $D^{*-} \to D^0 + \pi^-$ and $D^{*+} \to \bar{D}^0 + \pi^+$ samples was done separately, it is necessary to check the compatibility between these samples as well.

Fig.23 shows the compatibility check between the samples D^0 and $\bar{D}^0$.

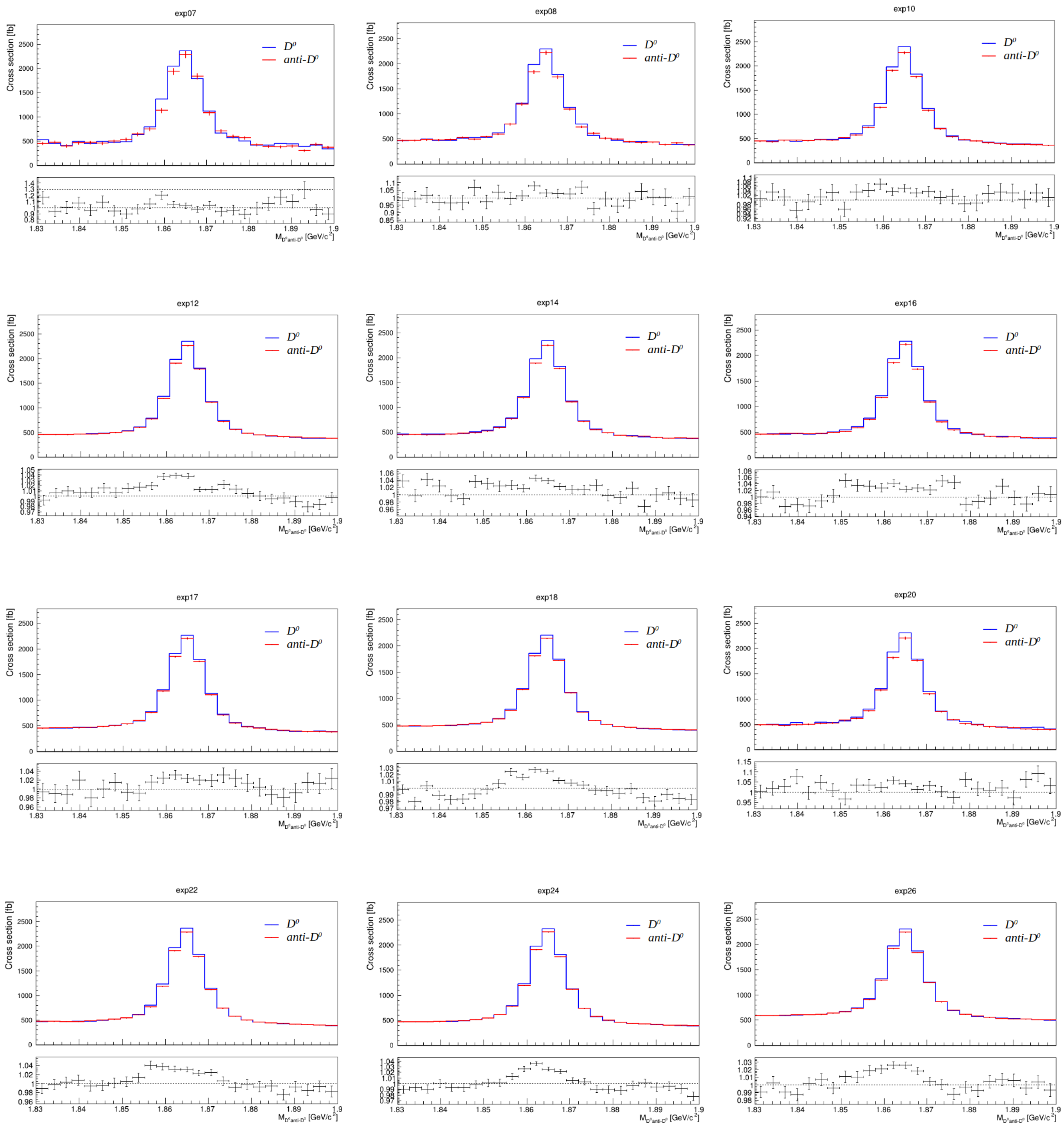

Figure 23: *Compatibility check between D^0 vs. $\bar{D}^0$ samples*

The results indicate that there is good agreement between the D^0 vs. $\bar{D}^0$ samples, and they can be used together.

A similar check has also been performed for the D^{*+} vs. D^{*-} samples and a good agreement was also observed there. In general we can conclude that all the *experiments* used are compatible with each other and can be used as a big data file.

4.3 MC samples

The MC15 run independent sample was used for these studies with the background condition ”BGx1” for the event selection and background suppression. The samples have been produced through the GRID system [34] based on a huge amount (with the integrated luminosity for each quark combination equal to 1000 fb^{-1}) of the so-called "generic" MC data (prepared by the Belle II Collaboration), which include different quark combinations like: $u\bar{u}, d\bar{d}, s\bar{s}, c\bar{c}$ as well as $B^0\bar{B}^0$, B^-B^+ pairs combined with weights proportional to the corresponding cross section for $e^-e^+ \to q\bar{q}$ processes. Table. 3 shows the possible processes with the corresponding cross sections.

Processes	Cross section [nb]	Name of the production
$e^+e^- \to u\bar{u}$	1.61	’uubar’
$e^+e^- \to d\bar{d}$	0.4	’ddbar’
$e^+e^- \to s\bar{s}$	0.38	’ssbar’
$e^+e^- \to c\bar{c}$	1.3	’ccbar’
$e^+e^- \to B\bar{B}$	1.05±0.1	’mixed’,’charged’

Table 3: *Possible processes with the corresponding cross sections*

The full reconstruction of charged tracks based on the hits in a corresponding detector is done using the Belle II tracking algorithm. Such realistic MC simulation with the reflection of the whole Belle II spectrometer provides good agreement for the MC-Data comparison, some examples of such a comparison can be seen in Belle II papers [38], [39], [40]. The invariant mass distributions of the samples D^{*+} and D^{*-} for different combinations of MC are shown in Fig. 24.

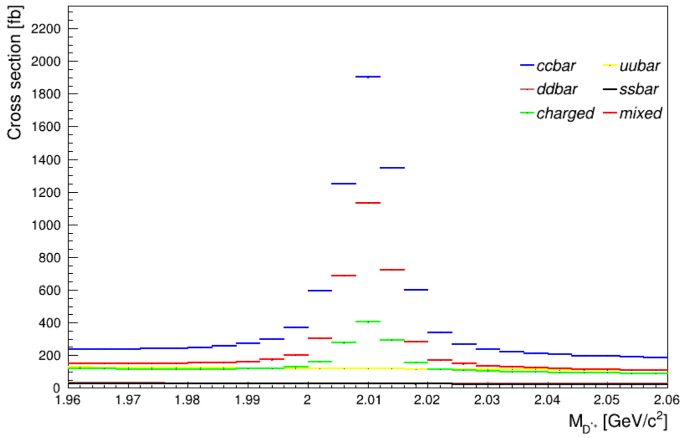

a

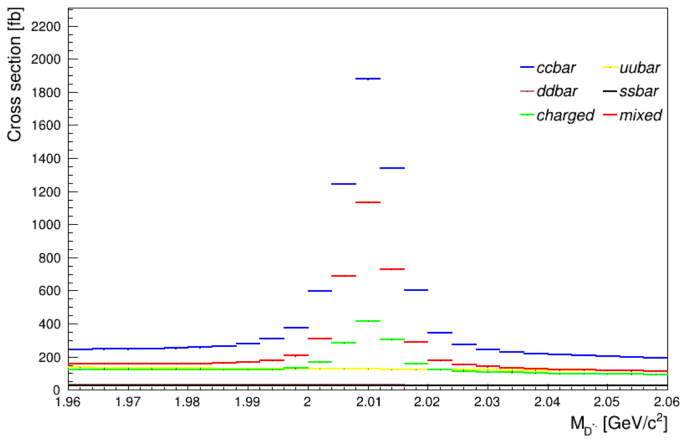

b

Figure 24: *The invM distribution for D^{*+} (a) and D^{*-} (b).*

And the invariant mass distributions of the D^0 and $\bar{D}^0$ particles for different MC samples are shown in Fig. 25.

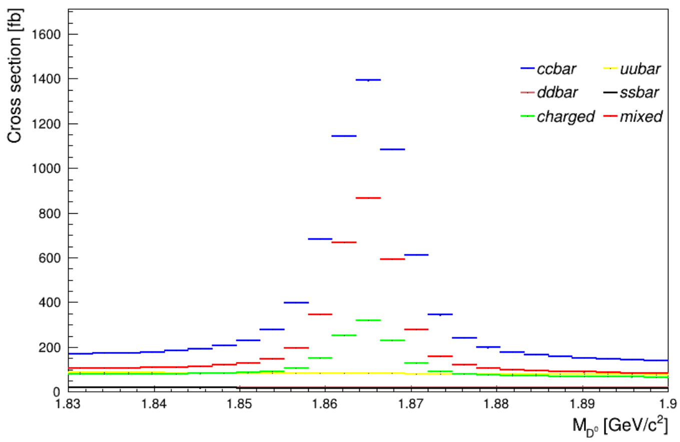

a

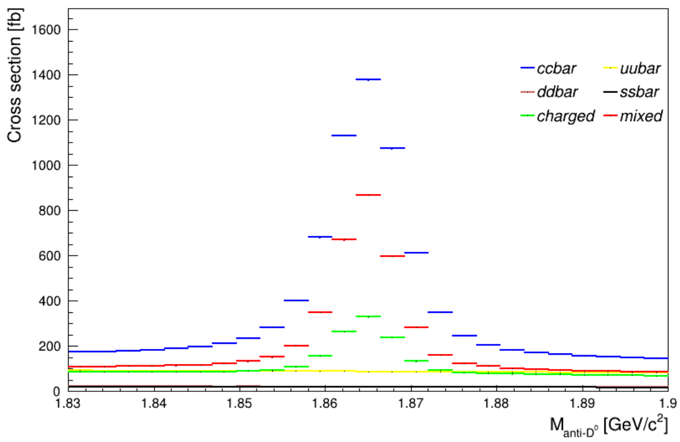

b

Figure 25: *The invM distribution for* D^0 *(a) and* $\bar{D}^0$ *(b).*

As it was expected the $c\bar{c}$ sample has the most participation in invariant mass distributions for $D^{*\pm}$ and $D^0(\bar{D}^0)$ particles since they are charmed particles.

The compatibility check between $D^{*-} \to D^0 + \pi^-$ and $D^{*+} \to \bar{D}^0 + \pi^+$ samples was also checked for MC samples and the results are shown in Fig. 26.

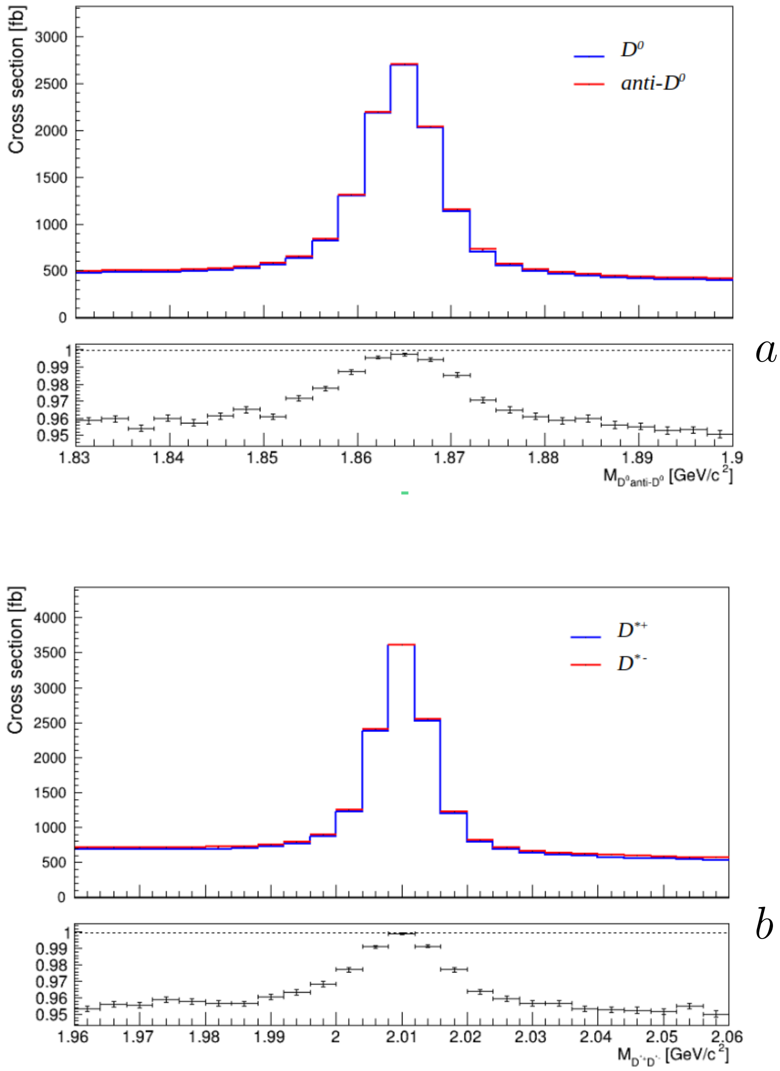

Figure 26: *The invM distribution for D^0 vs. $\bar{D}^0$ (a) and D^{*+} vs. D^{*-} (b) samples.*

The good agreement between all discussed MC combinations allows us to look at them together as a combined MC sample. All summarizing was done proportional to cross sections.

4.4 Previous studies

In order to calculate the efficiency and mis-identification probability values it is necessary to estimate both the number of events in numerator and denominator (Eq. 13- 16) after subtracting the background, that is, based on the fitting results for mean and sigma to estimate the number of events under the signal region (Gaussian distribution) and number of events under the polynomial within $M \pm 3\sigma$. Because the efficiency depends on a hadron momentum (p_h) and polar angle (θ_h), the invariant mass spectrum is reconstructed in double slices over a hadron momentum and polar angle. This creates certain difficulties in the case of limited statistics in the data for the decays considered [42], [43]. With the lack of statistics in some of the double bins it becomes impossible to perform the fitting procedure with a stable outcome for the mean and sigma as a fit parameter, as well as for numbers of signal (N_{signal}) and background ($N_{back.}$) events, which later will be used to define the mass window and finally will be used for $\epsilon_{\pi/K}$ and $\eta_{\pi/K}$ extraction. The difficulties with possible lack of statistics in experimental data to perform necessary fitting of invariant mass spectra into many double bins can be solved by using the following scheme:

- Check how well the MC simulated data agree with experimental data in term of invariant mass spectrum, here all applied cuts should be identical for experimental and MC data.
- In case of good agreement one can use huge number of MC samples providing enough statistics in each momentum/polar angle double bin for any of investigated decay modes
- Perform the fitting procedure with MC data, then determine the μ ratio of signal to background events for each double bin:

$$\mu(p_h, \theta_h) = \frac{N^h_{signal} = \int_{M-3\sigma}^{M+3\sigma} N(x, M, \sigma)dx}{N^h_{back.} = \int_{M-3\sigma}^{M+3\sigma} P(x, n)dx + N^h_{signal}}, \tag{17}$$

  where $N(x, M, \sigma)$ and $P(x, n)$ are the Gaussian function and polynomial of the order n used for the fitting procedure.

The ratios $\mu(p_h, \theta_h)$ will be applied for experimental invariant mass spectra at each p_h, θ_h double bin to determine the signal events like:

$$N^{data}_{signal}(p_h, \theta_h) = N^{data}_{total}(p_h, \theta_h)\mu(p_h, \theta_h) \tag{18}$$

The described scheme corresponding to formulas Eq. 17 and 18 has to be performed in two options: first for the spectra fitted with applied R_{cut} (corresponds to the numerator in Eq. 13, 14), second without applied R_{cut} (corresponds to the denominator in Eq. 13, 14). Also, the μ coefficients have to be extracted for cases when pion or kaon are in the ARICH acceptance. Then, in the final stage, four tables with the extracted coefficients μ will be obtained.

In order to make a propagation of uncertainties for the statistical error ΔN^{data}_{signal} in Eq. 18 the errors obtained during the fit procedure of invariant mass spectrum at different momentum (angular) bins from MC samples ΔN^{MC}_{signal} and $\Delta N^{MC}_{back.}$ were used to define values of $\Delta\mu$ by taking into account a clear correlation between the samples of N_{signal} and $N_{back.}$ events as:

$$\Delta\mu = \frac{1}{N_{total}}\sqrt{(\mu\Delta N_{total})^2 + \Delta N^2_{signal} - 2\mu^{3/2}\Delta N_{signal}\Delta N_{total}}, \tag{19}$$

where $N_{total} = N_{signal} + N_{back.}$, $\Delta N_{total} = \sqrt{\Delta N^2_{signal} + \Delta N^2_{back.}}$.

Based on these uncertainties, the next propagation on the level of Eq.19 can be finally performed.

4.5 Technical part

The main MC generator to simulate hadron interactions in high-energy physics is Pythia8 package [35], and simulation of a charged track passing through the material of a target and the detector system is done with the Geant4 package [36]. All simulations are performed within the Belle II Analysis Software Framework (basf2 [37]), Fig. 27, with detailed simulation of the responses of the involved detectors taking into account the calibration constants for all detectors.

Figure 27: *Basf2 framework*

To perform this analysis a python code was written which allows us to reconstruct necessary particles. In this case $D^{*\pm} \to D^0(\bar{D}^0)\pi^\pm \to (K^\mp\pi^\pm)\pi^\pm$ decay was reconstructed. The slight changes on fallowing code may allow for the reconstruction off different particles, and also similar studies for other sub-detectors.

Later, codes were sent to the GRID system and after being done were downloaded to AANL, Belle local machine. In order to continue further studies *ROOT* and $JupiterNotebook$ programs were used. We also wrote a code for fitting procedures as well as another code for checks of different distributions for different variables.

The codes can be seen in paragraph 5.6

5 Results

5.1 MC/Data comparison

In this section, the Data vs. MC comparisons will be shown. For the combined $D^{*\pm}$ and $D^0\bar{D}^0$ samples, the results are shown in Fig. 28

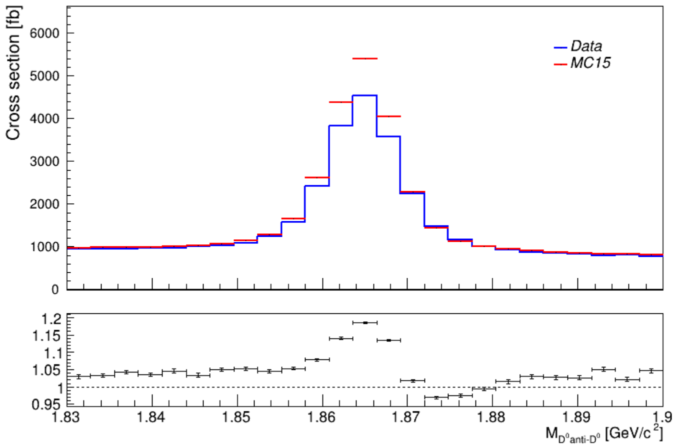

a

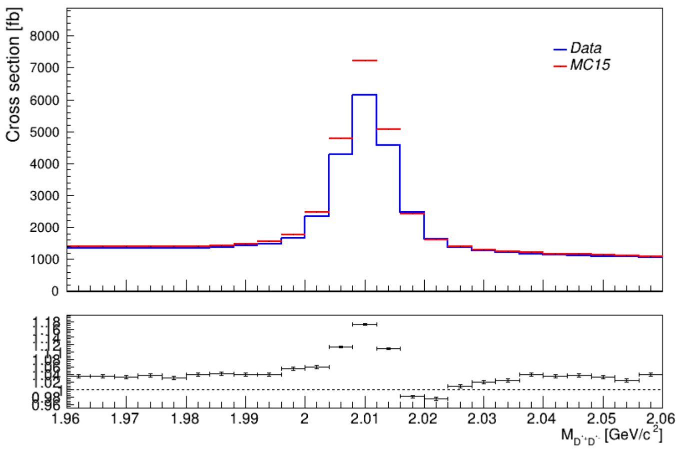

b

Figure 28: *The invariant mass distribution for D^0 (a) and D^{*+} (b).*

As we can see from the obtained results there is a good agreement in the background region for both the $D^0\bar{D}^0$ and $D^{\pm}$ samples for MC and Data. But for the signal region there is an MC / Data difference of about 17% in the signal region for $D^{*\pm}$ and of about 18% for $D^0\bar{D}^0$ sample.

More detailed comparisons between $D^{*-} \to D^0 + \pi^-$ and $D^{*+} \to \bar{D}^0 + \pi^-$ samples for Data and MC with ratio plots are shown on Fig. 29 - Fig. 30.

Fig. 29 shows the invariant mass distributions of D^{*+} and D^0 particles.

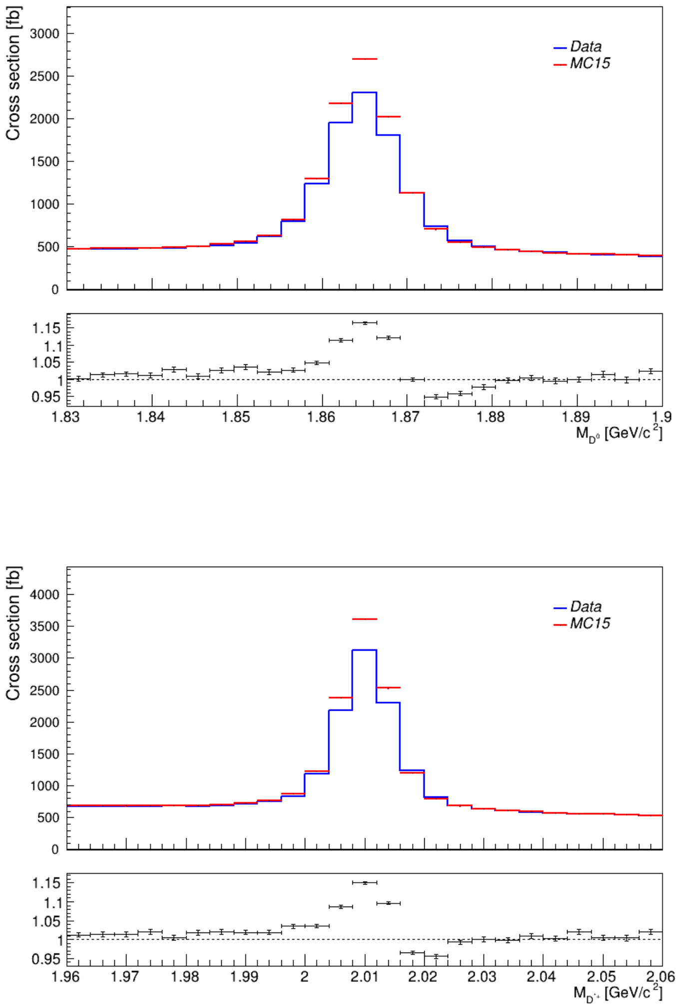

a

b

Figure 29: *The invariant mass distribution for D^0 (a) and D^{*+} (b).*

As we can see from the obtained results, we have a good agreement in the background region for both D^0 and D^{*+} samples for MC and Data. But for signal region we have MC/Data difference about 17% for D^{*+} and about 15% for D^0 sample.

And for D^{*-} and $\bar{D}^0$ samples we see fallowing results.

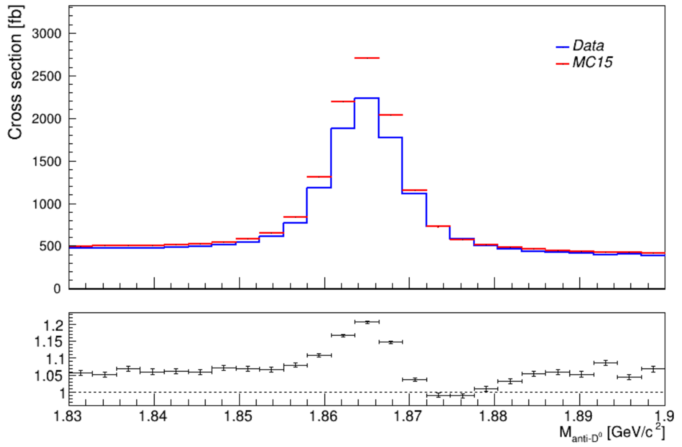

a

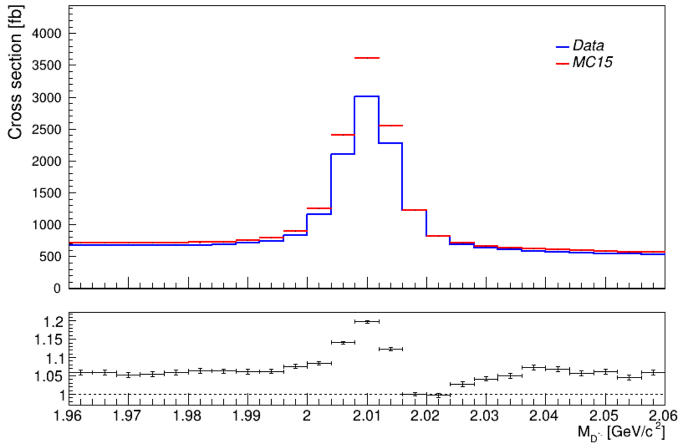

b

Figure 30: *The invariant mass distribution for D^0 (a) and D^{*+} (b).*

We can see the same pattern here, a good agreement in the background regions but a difference in the MC / Data ratio in the signal region about 20% for D^{*-} and about 21% for the $\bar{D}^0$ sample.

In order to get better MC/Data comparison, reduce background, and get more clean signal samples, we implement additional restrictions and check the influence of variables such as: $pValue$, pt, and $pCMS$. The distributions of these variables are shown below and their influences are shown on invariant mass distributions.

pValue is the χ^2 probability of the track fit. This variable defines the quality of final tracks and was used in Belle II different studies before. In this case as final-stage particles we have only *kaons* and *pions*. $pValue$ distributions for our three tracks: *kaons*, *pions* and *slow pions* (pions of the daughter of $D^{*\pm}$) are shown on Fig. 31

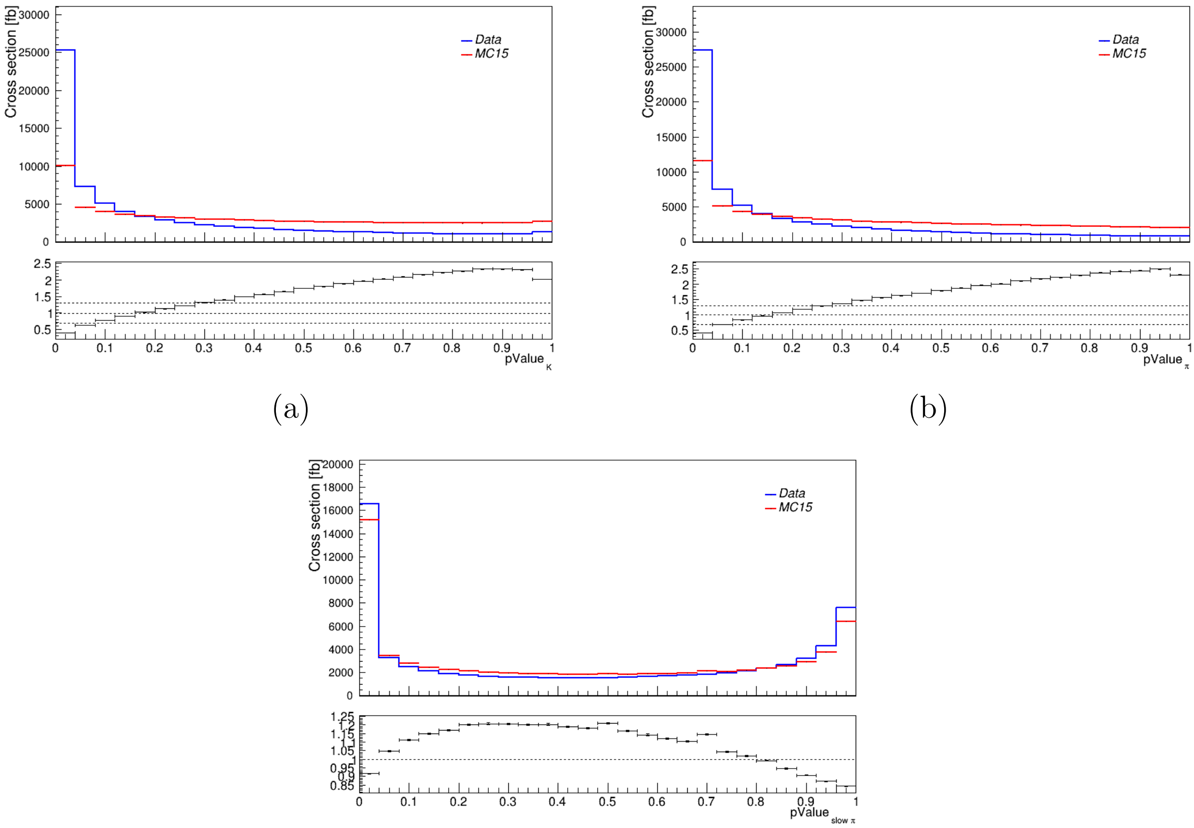

(a) (b) (c)

Figure 31: *pValue distributions for kaons (a), pions (b) and slow pions (c).*

As we can see from the results obtained in Fig. 31, $pValue$ the distribution differs for Data and MC samples. In data for daughter particles of $D^0\bar{D}^0$ the peak around 0 is much higher than for MC. Therefore, we see more bad tracks for Data than for MC.

We apply $pValue > 0.001$ for all three charged particles in order to reject bad-quality fitted tracks.

The invariant mass distributions of $D^0\bar{D}^0$ and $D^\pm$ after applying the restriction $pValue > 0.001$ are shown in Fig. 32.

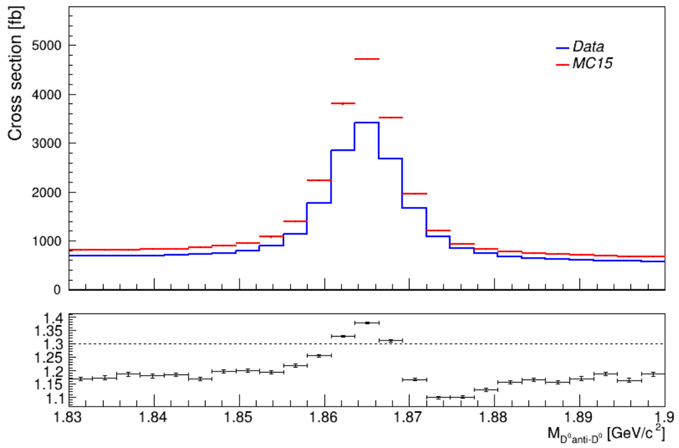

b

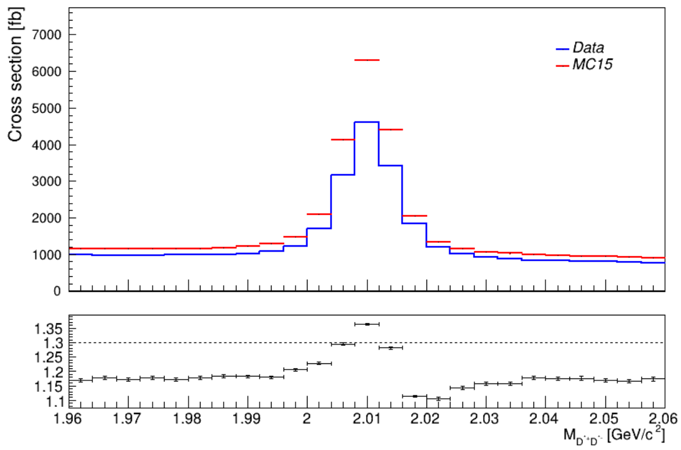

c

Figure 32: *The invariant mass distribution for $D^0\bar{D}^0$ (a) and $D^{\pm}$ (b) samples with a cut pValue > 0.001.*

As we can see from Fig. 32 after applying $pValue > 0.001$ MC/Data ratio in signal region differs about 39% for $D^{*\pm}$ and about 37% for $D^0\bar{D}^0$ samples. Thus, this is not a reliable cut, and we will not take it for our future studies.

pt is the transverse momentum of a particle. For our final stage three particles we have fallowing distributions:

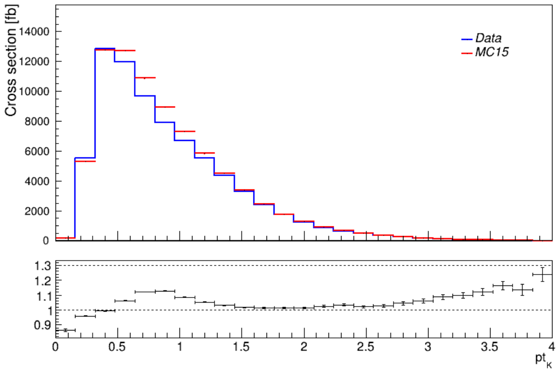

(a)

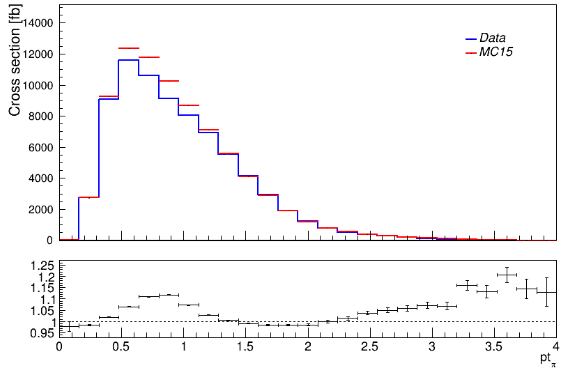

(b)

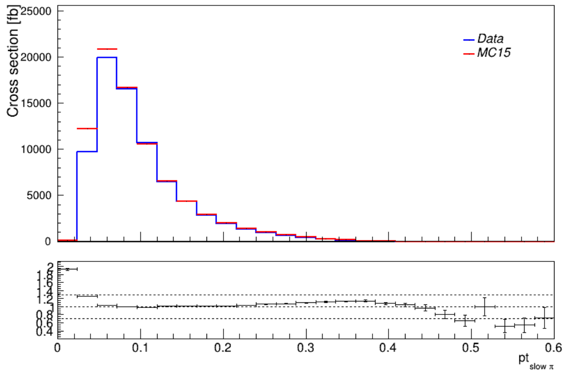

(c)

Figure 33: *pt distributions for kaons (a), pions (b) and slow pions (c).*

As we can see from Fig. 33 there is a good agreement between Data vs. MC for the pt distributions for all three cases. For slow pions, the transverse momentum reaches $0.4[GeV/c]$ and applying a cut on this variable will reduce the reconstruction of $D^{*\pm}$ particles, which is not beneficial for this study. We will apply the $pt > 0.1$ cut to the daughter kaons and pions of $D^0\bar{D}^0$.

The invariant mass distributions of $D^0\bar{D}^0$ and $D^{\pm}$ after applying the restriction $pt > 0.1$ are shown in Fig. 34.

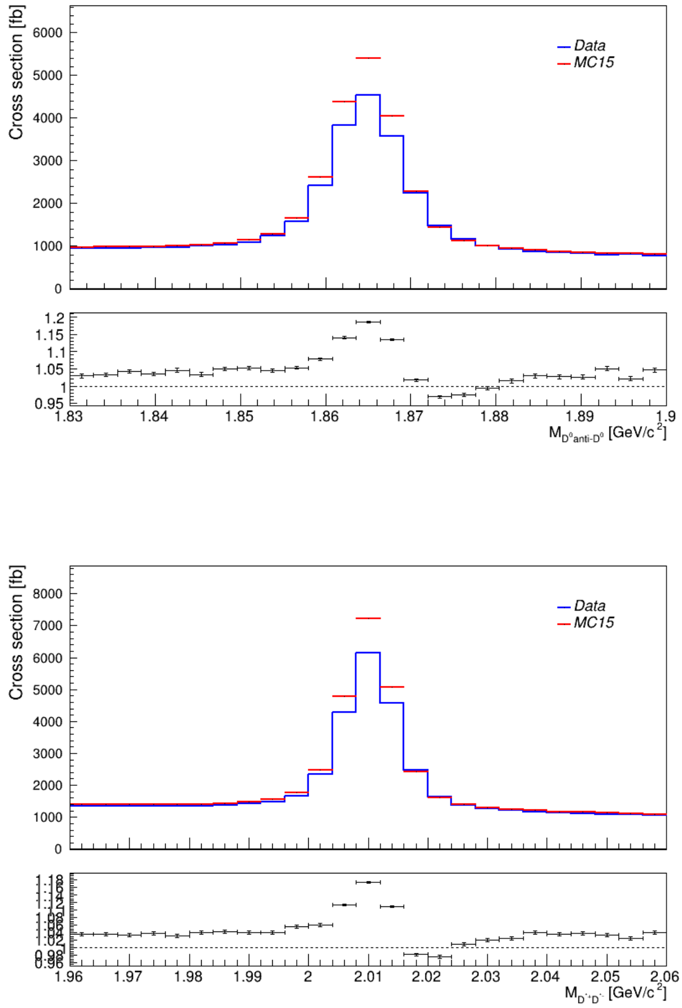

a

b

Figure 34: *The invariant mass distribution for $D^0\bar{D}^0$ (a) and $D^{\pm}$ (b) samples with a cut pt > 0.1 .*

This cut does not bring to much changes in Data/MC ratio and since we already have a momentum cut on both tracks we will skip this cut as well.

pCMS is the momentum of a $D^{*\pm}$ in the CMS frame which is an event variable. The distributions of the variable $pCMS$ are shown in Fig. 35.

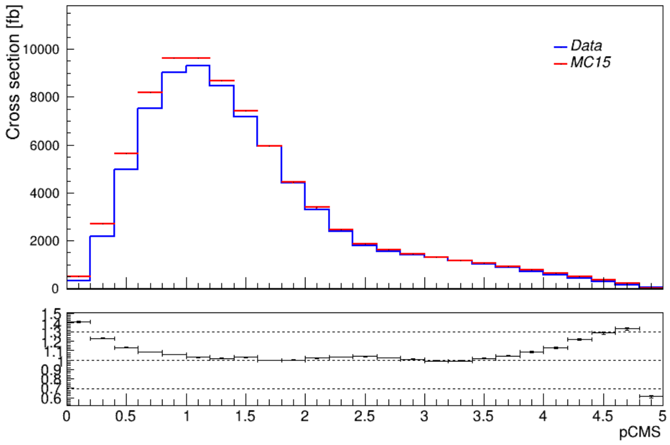

Figure 35: *Momentum in CMS frame*

This variable is often used in Belle II studies for background suppression [41].

The invariant mass distributions of $D^0\bar{D}^0$ and $D^{\pm}$ after applying the restriction $pCMS > 2.5$ are shown in Fig. 36.

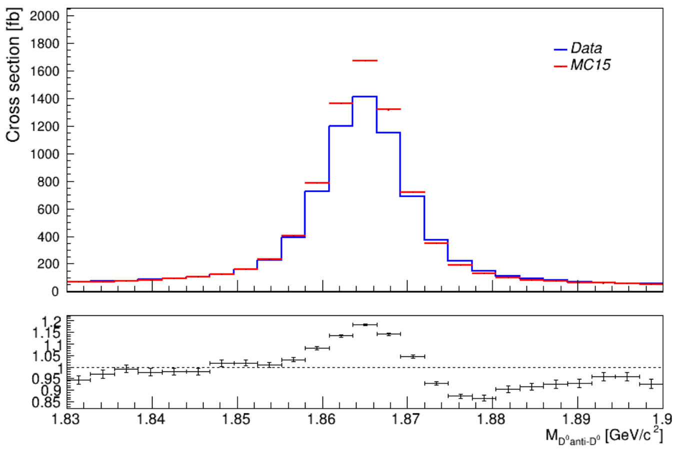

a

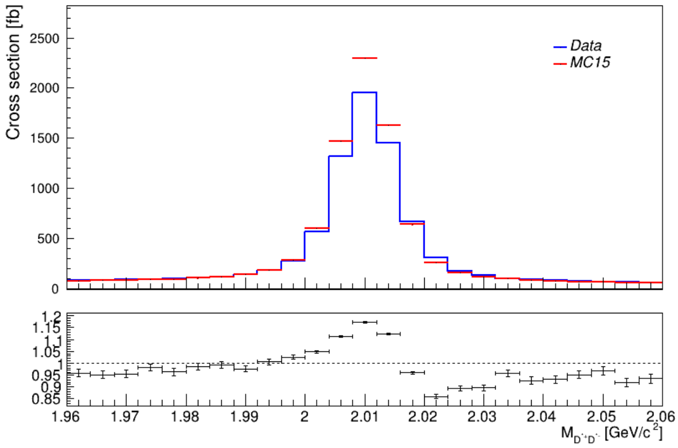

b

Figure 36: *The invariant mass distribution for $D^0\bar{D}^0$ (a) and $D^{\pm}$ (b) samples with a cut pCMS > 2.5.*

In Fig. 28 (b) we see that for the $D^0\bar{D}^0$ sample the signal/background ratio differs about 5.4 for Data and 4.5 for MC. After applying $pCMS > 2.5$ on Fig. 36 (b) we see that these ratios are getting better and for Data it becomes about 20 and 23.8 for MC.

As can be seen from Fig. 36 $pCMS > 2.5$ restriction is very useful for our studies and it reduces background making the invariant mass distribution more clean.

5.1.1 MC run dependent studies

For studies above we were using *run independent*(ri) MC samples, which means that *runs* are equal with their luminosity values and do not have run dependence. Meanwhile, *run dependent*(rd) MC has the same experiment and run numbers as the corresponding data from which the beam background overlay events are extracted.

As was shown in Fig. 28, 32, 34, 36 there are some differences between the MC15 *run independent*(ri) and Data samples. The decision was also made to check the compatibility of the data with the MC15 *run dependent* sample. For this purpose was generated $D^{*+} \rightarrow D^0(K^-\pi^+) + \pi^+$ MC *run dependent*(rd)

sample for 20 − 26 *experiments* which integrated luminosity corresponding to 699.235$[fb^{-1}]$. Therefore we used only these experiments also for Data sample.

The comparison results between MC15 *run independent* and MC15 *run dependent* samples are shown on Fig. 37. As we can see they are in good agreement with each other and there are just tiny differences.

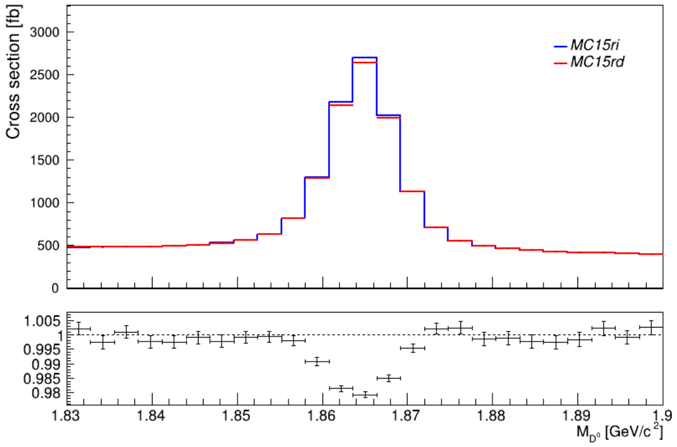

a

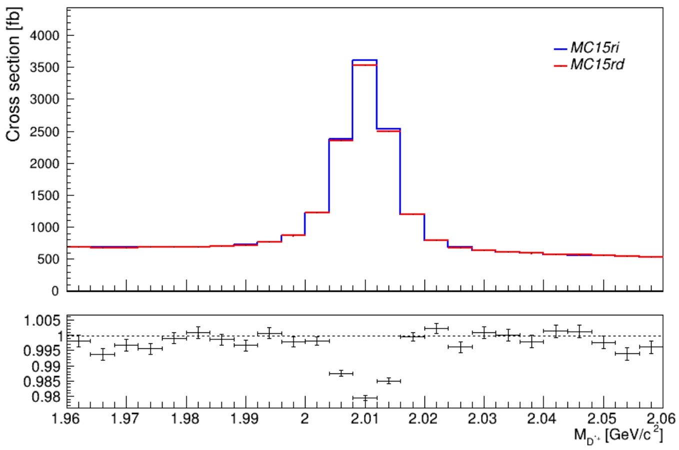

b

Figure 37: *The invariant mass distribution for D^0 (a) and D^{*+} (b) samples for MC15ri and MC15rd*

The comparison results between Data and MC15 *run dependent* samples are shown in Fig. 38 and it can be seen that there is a difference of approximately 15% in the signal region which is really close to obtained results from Data vs. MC15 *run independent* studies.

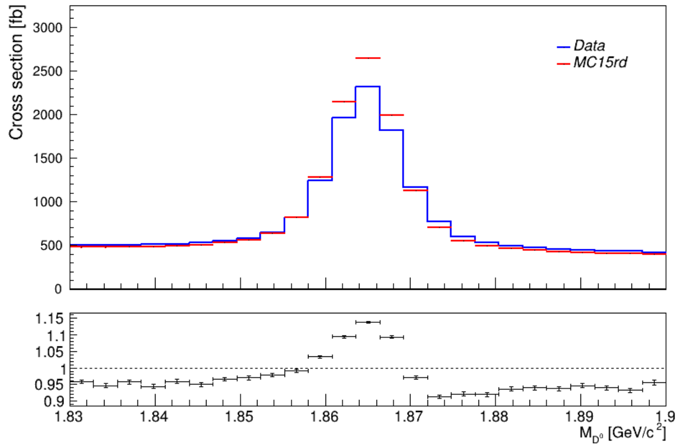

a

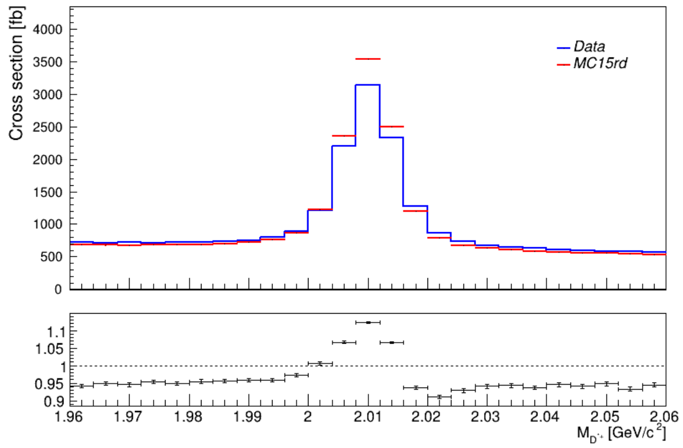

b

Figure 38: *The invariant mass distribution for D^0 (a) and D^{*+} (b) samples for Data and MC15rd*

In conclusion we can say that the MC15 *run independent* and MC15 *run dependent* samples are in good agreement with each other but both have some noticeable differences from Data.

5.2 RooFit

In order to perform a huge amount of necessary fittings into many double momentum/angular bins, the fitting procedure has been realized using the Python framework and RooFit [44]. As a result of the performed fit, one can extract not only the needed parameters for Gaussian and polynomial, but also the number of signal and background events within $\mu \pm 3\sigma$ and estimated uncertainties for those events.

In order to find the best corresponding fit for $D^0\bar{D}^0$ combined spectra, we used one- and double-Gaussian fits with 1^{st} order of Chebyshev polynomial. The typical examples of the Gaussian fit are shown in Fig. 39.

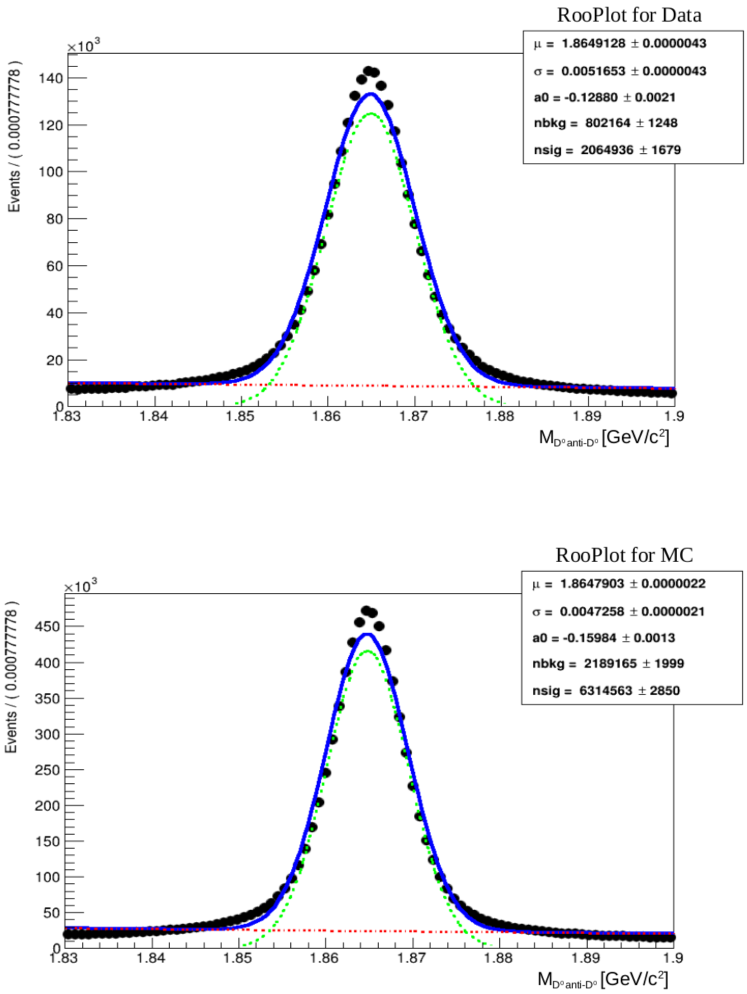

a

b

Figure 39: *The fitted $D^0\bar{D}^0$ invariant mass distributions for Data (a) and MC (b) with one Gaussian + 1^{st} order of Chebyshev polynomial.*

As we can see from Fig. 39 one Gaussian fit does not fully cover the invariant mass region of $D^0\bar{D}^0$ particle, and there is a need to apply the second Gaussian. Meanwhile, the Chebyshev polynomial fully covers the background region.

Fig. 40 shows an invariant mass fit of $D^0\bar{D}^0$ with double Gaussian and 1^{st} order of the Chebyshev polynomial.

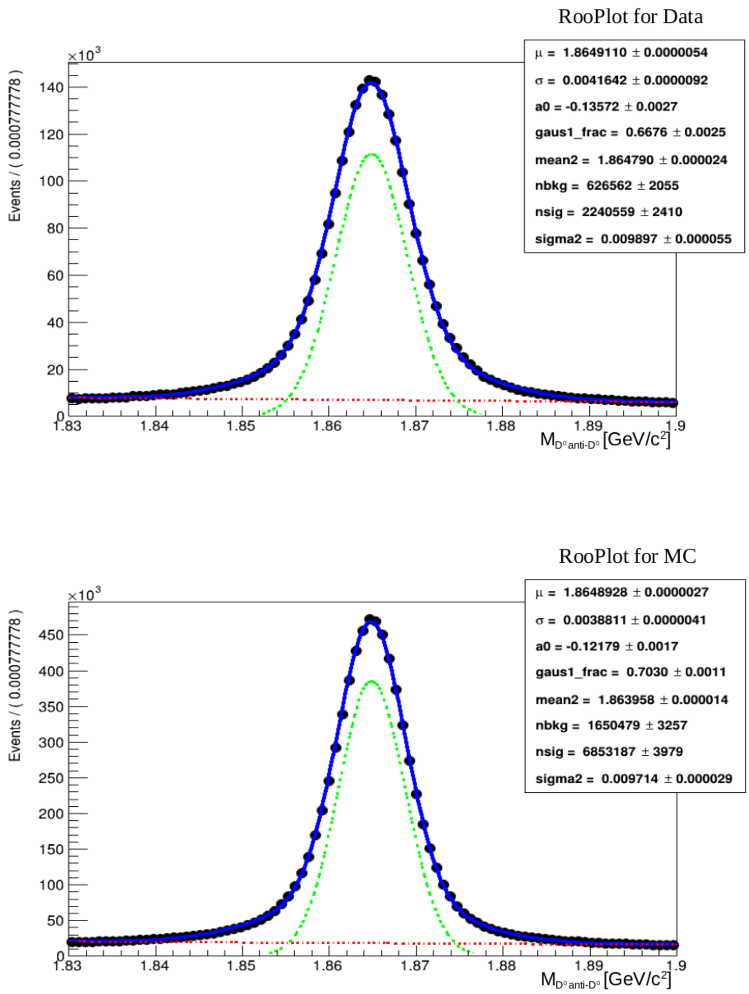

a

b

Figure 40: *The fitted $D^0\bar{D}^0$ invariant mass distributions for Data (a) and MC (b) with double Gaussian + 1^{st} order of Chebyshev polynomial.*

For future studies, we will study particles that form the signal region $\mu \pm 3\sigma$ and go to the acceptance of ARICH, which is a very narrow angular range $17° - 32°(0.2967[rad] - 0.52359[rad])$. If a *kaon* comes from the $\mu \pm 3\sigma$ signal region of $D^0\bar{D}^0$ particles and goes to the ARICH acceptance, the Fig. 41 will show the *momentum* and *polar angle* distributions of it.

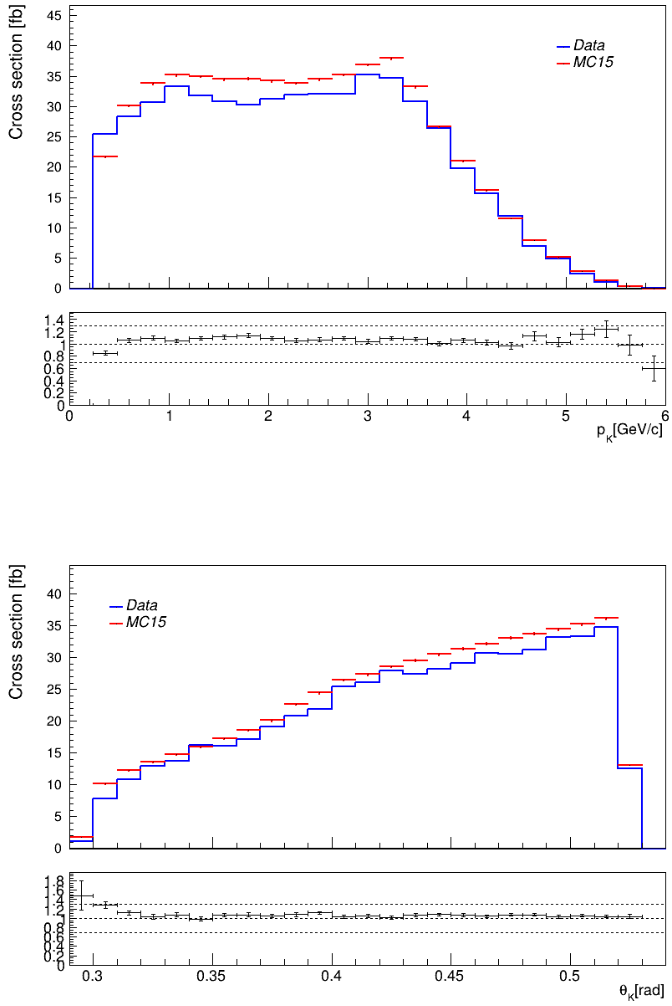

a

b

Figure 41: *Momentum(a) and polar angle(b) distributions for Kaons*

And for pions which come from the $\mu \pm 3\sigma$ signal region and go to ARICH acceptance, Fig. 42 will show the *momentum* and *polar angle* distributions of it.

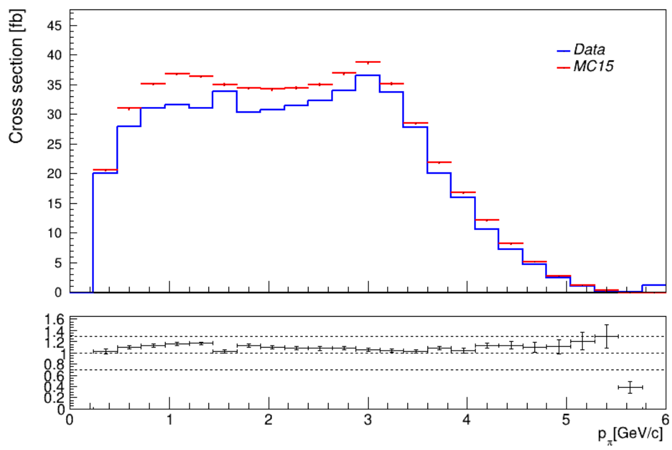

a

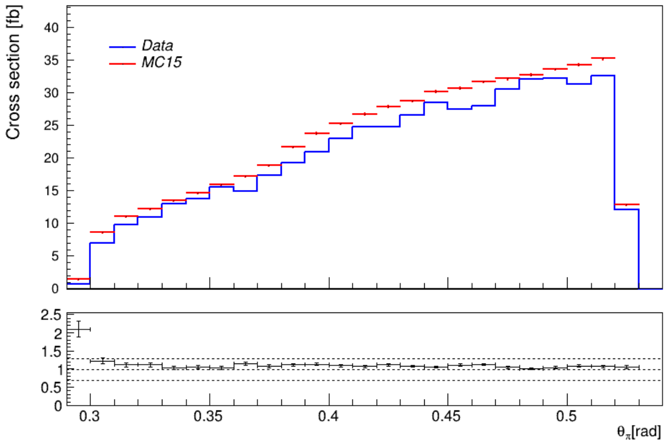

b

Figure 42: *momentum(a) and polar angle(b) distributions for Pions*

For present studies we will use 6×6 two-dimensional binning over momentum and polar angle shown in Table 1:

p bins [GeV/c]	θ bins [rad]
[0.3;1.0]	[0.30;0.36]
[1.0;1.7]	[0.36;0.39]
[1.7;2.4]	[0.39;0.42]
[2.4;3.1]	[0.42;0.45]
[3.1;3.8]	[0.45;0.48]
[>3.8]	[0.48;0.53]

Table 4: *2D bining for kaons and pions*

As was defined in Eq.(11, 12) we are going to use $R_{K/\pi}$ and $R_{\pi/K}$ variables to calculate ARICH detection efficiency for kaons and pions. Fig. 43 shows the $R_{K/\pi}$ and $R_{\pi/K}$ distributions for kaons(a) and pions(b) in ARICH acceptance.

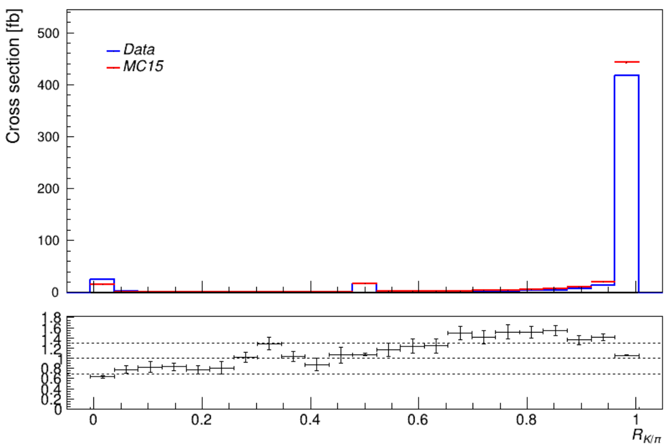

a

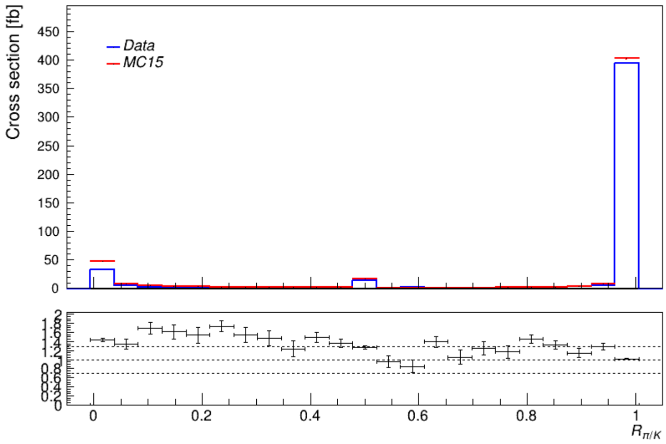

b

Figure 43: $R_{K/\pi}$ *and* $R_{\pi/K}$ *distributions for kaons(a) and pions(b).*

5.3 Efficiency and mis-identification 1D studies

Using Eq.(13-16) we calculated the efficiency and mis-identification probability values for kaons and pions obtained for Data and MC. For this purpose, we use the binning over momentum and polar angle shown in Table 4.

The efficiency and mis-identification probability values are determined as $\epsilon = A \pm \sigma_A / B \pm \sigma_B$, where A, σ_A, B, σ_B is defined from fitting procedures. For this purpose, bin-by-bin fitting was done.

The plots in Fig. 44 show the invariant mass distribution fits of $D^0\bar{D}^0$ when the kaon is in ARICH acceptance for MC studies over momentum binning. (a) column is our true kaon list, which has been detected in ARICH acceptance without any ID cut. In column (b), there are our kaons with the cut $R_{K/\pi} > 0.6$ applied, which means that with high probability, these particles are kaons. And in the (c) column there are the kaons with $R_{\pi/K} > 0.6$ which indicates that these particles with high probability are pions but were detected as kaons:

MC Kaons $0.3 - 1.0$[GeV/c] bin

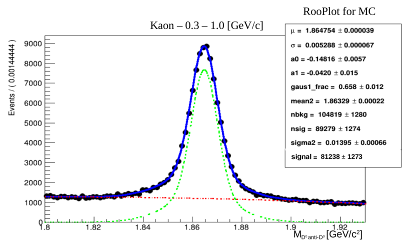

(a)

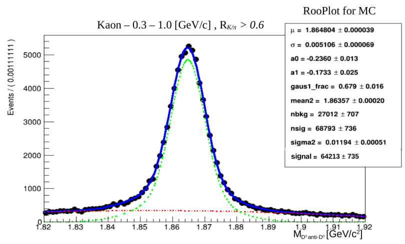

(b)

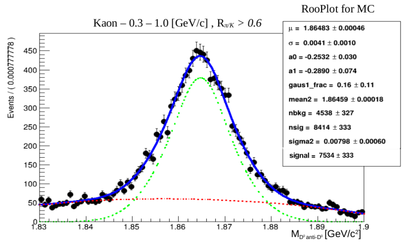

(c)

MC Kaons $1.0 - 1.7$[GeV/c] bin

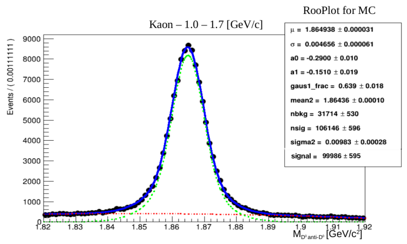

(a)

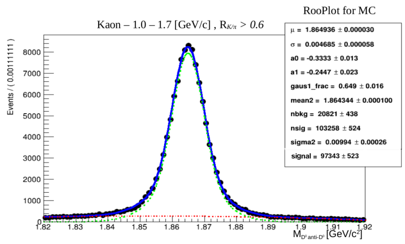

(b)

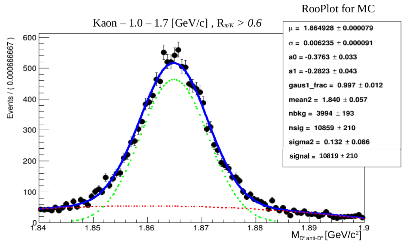

(c)

MC Kaons $1.7 - 2.4$[GeV/c] bin

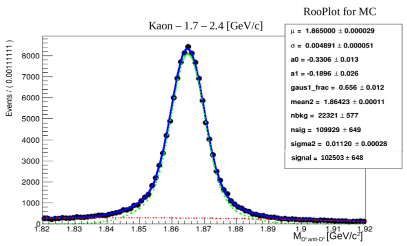

(a)

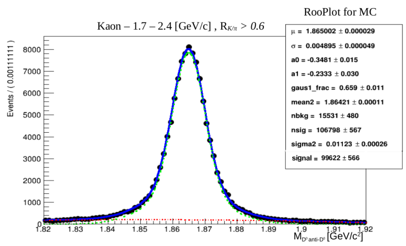

(b)

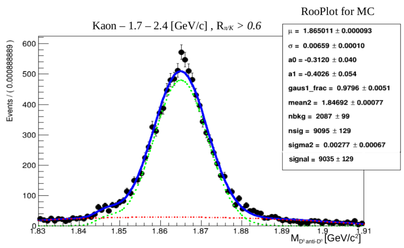

(c)

MC Kaons $2.4 - 3.1$[GeV/c] bin

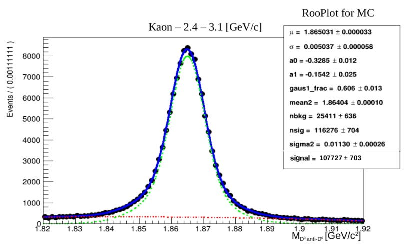

(a)

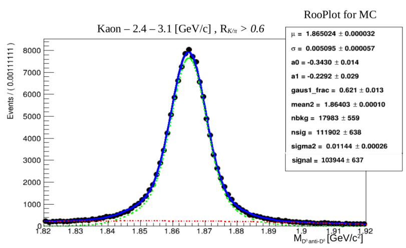

(b)

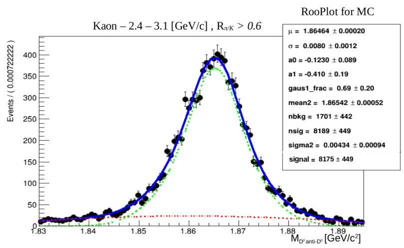

(c)

MC Kaons $3.1 - 3.8$[GeV/c] bin

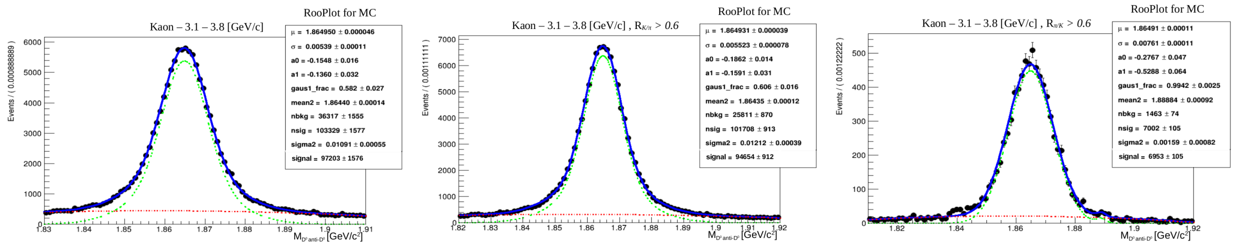

(a) (b) (c)

MC Kaons > 3.8[GeV/c] bin

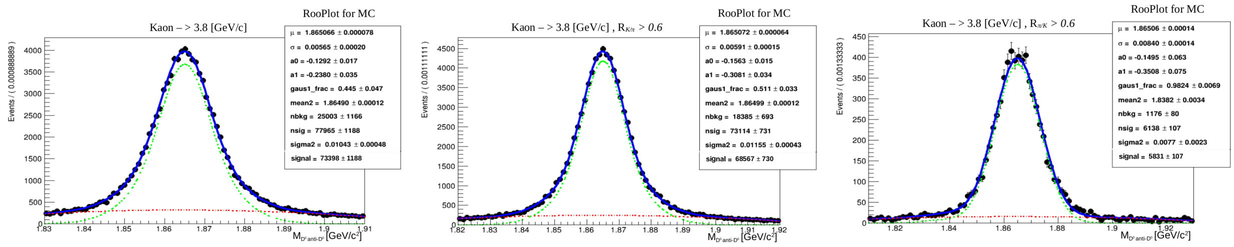

(a) (b) (c)

Figure 44: invariant mass distribution fit for Kaons from MC

Similar fitting pictures were also obtained *kaons* from the Data sample and also for *pions* from Data and MC.

A and B are the signal values in the $\mu \pm 3\sigma$ region and σ_A, σ_B are the corresponding error numbers of it, which we take from the pictures above. Having those numbers, we calculate efficiencies and mis-identification probabilities. Furthermore, we also calculate the efficiency uncertainty σ_ϵ that is determined from the equation.

$$\sigma_\epsilon = \frac{1}{B}\sqrt{\epsilon^2\sigma_B^2 + \sigma_A^2 - 2\epsilon^{2/3}\sigma_A\sigma_B} \tag{20}$$

Table 5 shows the overall performance of ARICH for the detection of *kaons* and *pions* over momentum binning for Data and MC.

Name	0.3 - 1.0 [GeV/c]	1.0 - 1.7 [GeV/c]	1.7 - 2.4 [GeV/c]	2.4 - 3.1 [GeV/c]	3.1 - 3.8 [GeV/c]	> 3.8 [GeV/c]
K_{eff}^{Data} $\pm\Delta\mu$	0.778 0.008	0.9721 0.0022	0.9712 0.0019	0.9479 0.003	0.9264 0.0072	0.8848 0.0063
K_{eff}^{MC} $\pm\Delta\mu$	0.790 0.006	0.9735 0.001	0.9718 0.0011	0.9648 0.0012	0.9737 0.0067	0.934 0.006
π_{eff}^{Data} $\pm\Delta\mu$	0.6797 0.010	0.8708 0.004	0.872 0.0039	0.8889 0.0049	0.934 0.009	0.88 0.009
π_{eff}^{MC} $\pm\Delta\mu$	0.631 0.0054	0.80 0.006	0.867 0.0039	0.88 0.0058	0.8496 0.0079	0.8760 0.0063
K_{misID}^{Data} $\pm\Delta\mu$	0.129 0.0109	0.111 0.0056	0.0768 0.0035	0.0778 0.002	0.069 0.002	0.069 0.00447
K_{misID}^{MC} $\pm\Delta\mu$	0.0927 0.0039	0.108 0.0019	0.088 0.0012	0.075 0.004	0.0715 0.0013	0.079 0.0016
π_{misID}^{Data} $\pm\Delta\mu$	0.025 0.002	0.095 0.003	0.0819 0.0049	0.09 0.0037	0.154 0.007	0.1586 0.0054
π_{misID}^{MC} $\pm\Delta\mu$	0.0288 0.00036	0.1038 0.0014	0.0892 0.006	0.0905 0.0036	0.1434 0.003	0.215 0.0044

Table 5: *Overall performance between Data and MC via momentum binning*

The efficiency and mis-identification probability values in one-dimensional frame over momentum binning can be seen on Fig. 45.

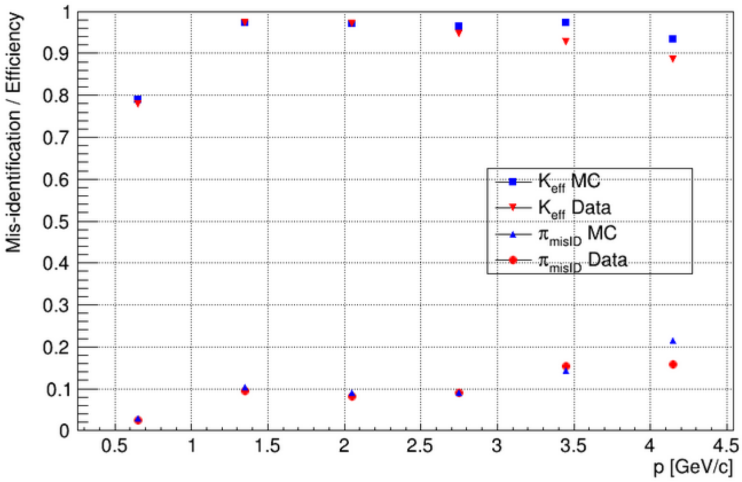

a

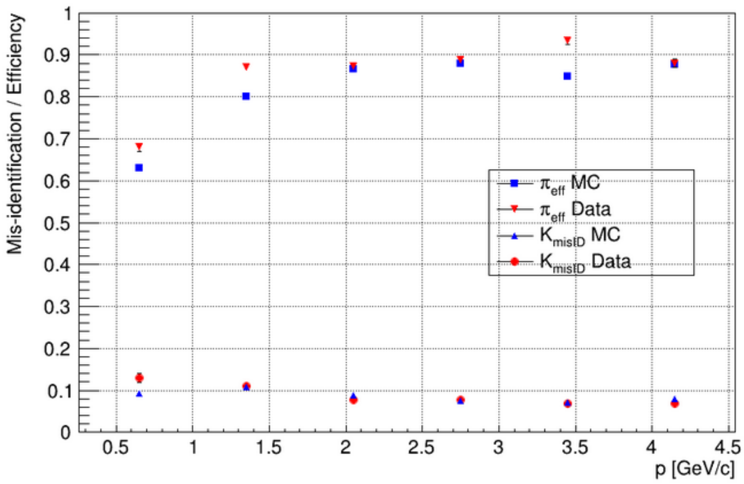

b

Figure 45: *Efficiency and misID dependencies in momentum binning.*

As can be seen from the obtained results, in general there is good agreement between the Data and MC samples. Kaon efficiency has its lowest value for the lowest momentum bin and is about 78-79%. The same behavior we can see also for pions, the detection efficiency is 63% for MC and about 68% for Data. Furthermore, the mis-identification probability for *kaon* is changed from 6-13%. It reaches its maximum for the small momenta and its smallest value for higher momentum. Meanwhile, the *pion* mis-identification probability is lowest for the smallest momentum bins and about 3%, but reaches its maximum for the highest momentum bins until 21%.

As we can see, the first bin efficiency results are much lower compared with other ones. We improved these numbers by slightly raising the lowest threshold value for momentum. Fix 0.7 [GeV/c] instead of 0.3 [GeV/c].

The efficiency and mis-identification probability values in one-dimensional frame over momentum binning after the lowest momentum value change can be seen in Fig. 46.

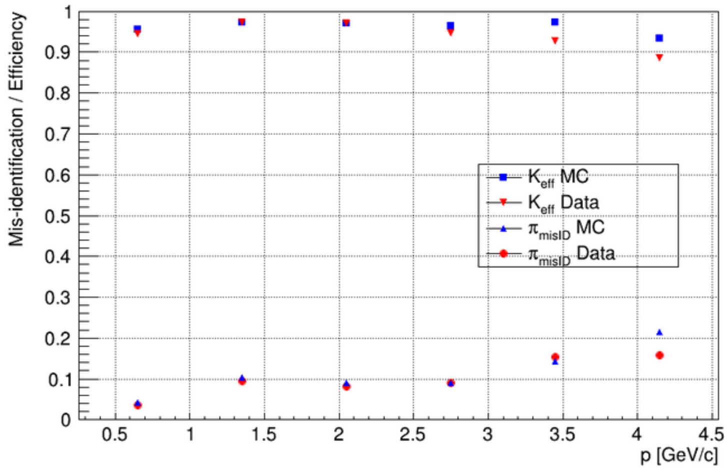

a

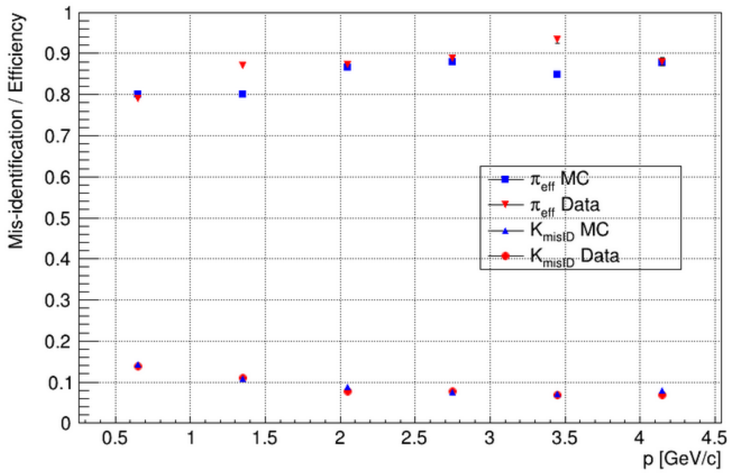

b

Figure 46: *Efficiency and misID dependencies in momentum binning.*

As we can see, increasing the momentum threshold from 0.3 [GeV/c] to 0.7 [GeV/c] improves the detection efficiency of *kaons* and *pions*. Rising the momentum helps us not to take the particles with bad tracking, which makes it difficult to identify the particle type. For *kaons* the efficiency improves from 78%(Data)/79%(MC) to 94%(Data)-95%(MC) and for *pions* from 63%(MC)/68%(Data) to 79%(Data)-80%(MC).

It is also important to see the ARICH performance in respect of polar angle. The plots in Fig. 47 show the invariant mass distribution fits of $D^0\bar{D}^0$ when Kaon is in ARICH acceptance for MC studies over angular binning.

MC Kaons 0.3 – 0.36[rad] bin

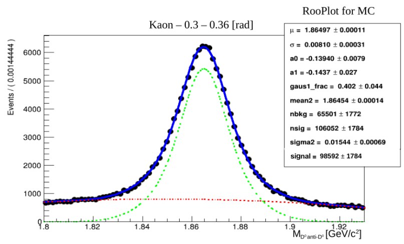

(a)

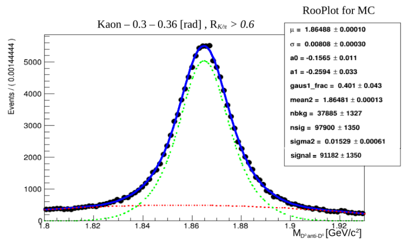

(b)

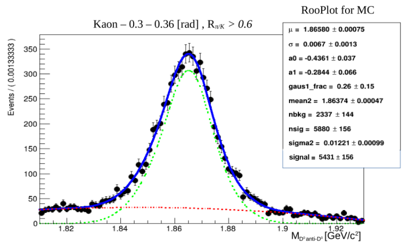

(c)

MC Kaons 0.36 – 0.39[rad] bin

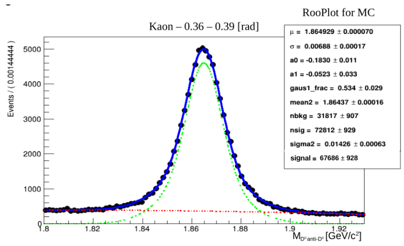

(a)

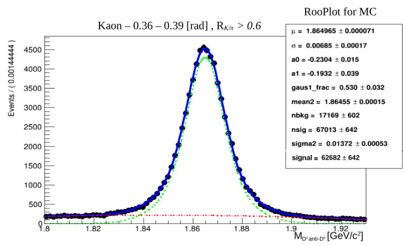

(b)

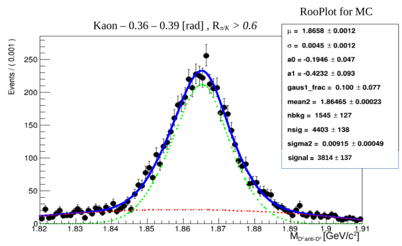

(c)

MC Kaons 0.39 – 0.42[rad] bin

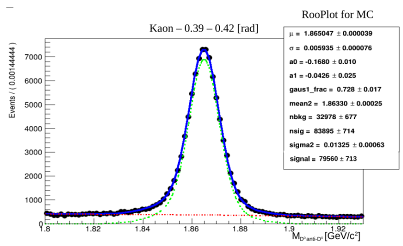

(a)

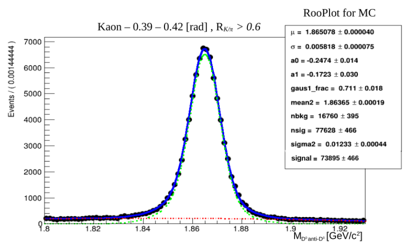

(b)

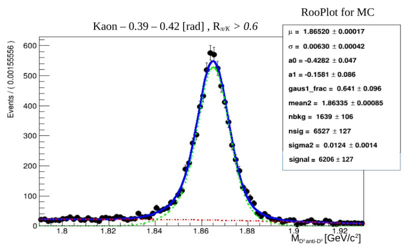

(c)

MC Kaons 0.42 – 0.45[rad] bin

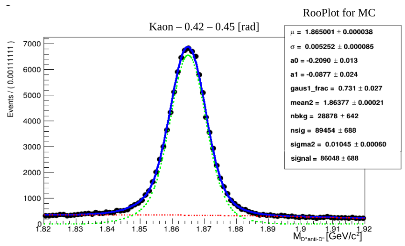

(a)

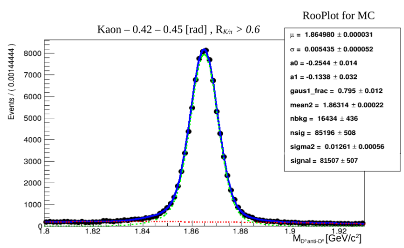

(b)

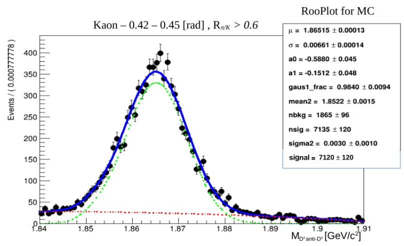

(c)

MC Kaons 0.45 – 0.48[rad] bin

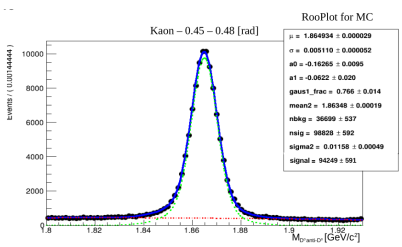

(a)

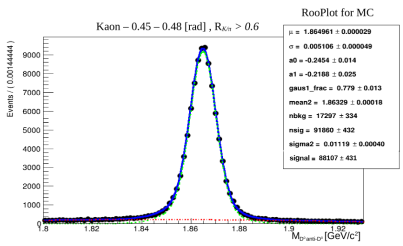

(b)

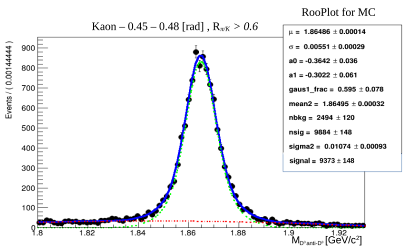

(c)

MC Kaons 0.48 – 0.53[rad] bin

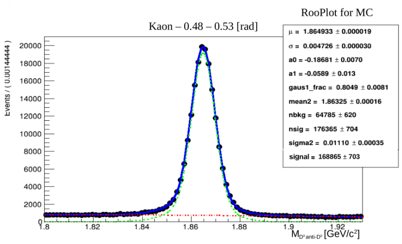

(a)

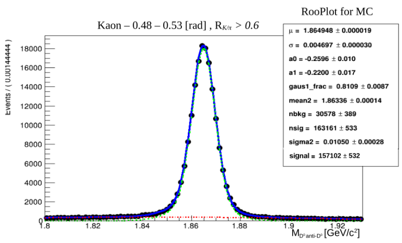

(b)

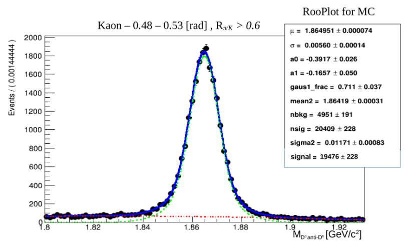

(c)

Figure 47: invariant mass distribution fit for Kaons from MC

Similar fitting procedures were done also for *kaons* from Data sample also for *pions* from Data and MC.

Fig. 48 shows the efficiency and mis-identification probabilities in one dimensional frame over polar angle binning.

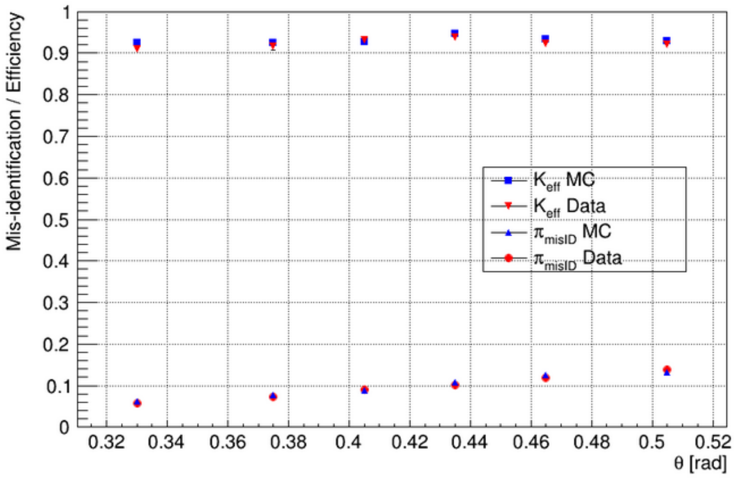

a

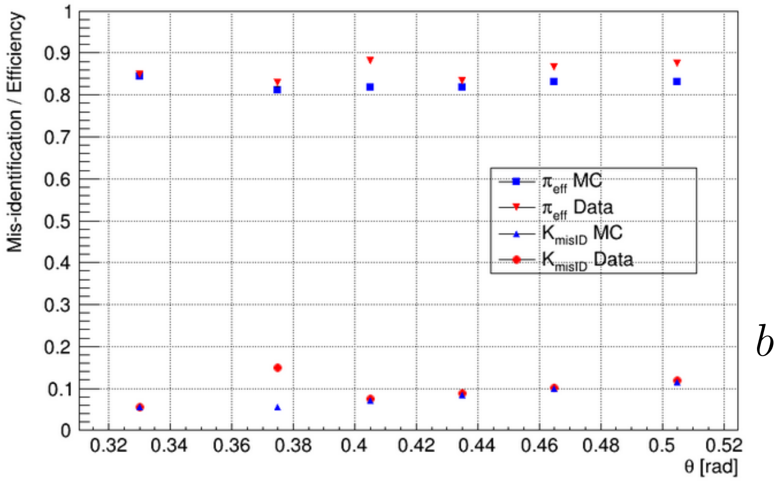

Figure 48: *Efficiency and misID dependencies in 1D polar angle bins.*

Table 6 shows the overall performance between Data and MC samples.

Name	0.3 - 0.36 [rad]	0.36 - 0.39 [rad]	0.39 - 0.42 [rad]	0.42 - 0.45 [rad]	0.45 - 0.48 [rad]	0.48 - 0.53 [rad]
K_{eff}^{Data} $\pm\Delta\mu$	0.910 0.004	0.9166 0.0089	0.9318 0.0033	0.9372 0.006	0.922 0.0028	0.9202 0.0017
K_{eff}^{MC} $\pm\Delta\mu$	0.9248 0.005	0.926 0.004	0.928 0.003	0.9472 0.0022	0.934 0.0018	0.9303 0.0011
π_{eff}^{Data} $\pm\Delta\mu$	0.8487 0.007	0.829 0.0088	0.882 0.0053	0.8335 0.0048	0.867 0.0054	0.875 0.0034
π_{eff}^{MC} $\pm\Delta\mu$	0.845 0.003	0.812 0.007	0.819 0.0053	0.8179 0.0079	0.83 0.0043	0.83 0.0028
K_{misID}^{Data} $\pm\Delta\mu$	0.055 0.0040	0.70 0.006	0.074 0.0038	0.087 0.0044	0.1014 0.0069	0.119 0.0024
K_{misID}^{MC} $\pm\Delta\mu$	0.055 0.0016	0.056 0.0019	0.07 0.0015	0.0827 0.0013	0.099 0.0014	0.115 0.00127
π_{misID}^{Data} $\pm\Delta\mu$	0.057 0.003	0.0738 0.0047	0.09 0.0034	0.1013 0.0027	0.1189 0.00368	0.138 0.0027
π_{misID}^{MC} $\pm\Delta\mu$	0.0611 0.0046	0.077 0.0019	0.089 0.0026	0.1078 0.0014	0.126 0.002	0.1315 0.0018

Table 6: *Overall performance between Data and MC via polar angle binning.*

As can be seen from the obtained results, in general there is good agreement between the Data and MC samples. *Kaon* detection efficiency for all bins in the above bins from 90% and defers from 91-94%. Meanwhile, *pion* detection efficiency is higher than 80% and is delayed from 81-87%. Furthermore, the mis-identification probability for *kaon* is changed from 5-12%. It reaches its minimum value for the small momentum bins and its highest value for higher momentum bins. For the *pion* mis-identification probability is lowest for the smallest momentum bins and about 6% but reaches its maximum for highest momentum bins until 13%.

5.4 Efficiency and mis-identification 2D studies

Using binning over momentum and polar angle as shown in Table 4 2D studies were performed. This is a more detailed study.

Table 7 shows the efficiency values for Data in 2D (momentum, polar angle) double bins for kaons.

K_{eff}^{Data}	0.3 - 1.0 [GeV/c]	1.0 - 1.7 [GeV/c]	1.7 - 2.4 [GeV/c]	2.4 - 3.1 [GeV/c]	3.1 - 3.8 [GeV/c]	$>$ 3.8 [GeV/c]
0.3 - 0.36 [rad]	0.8966	0.643	0.8208	0.966	0.891	0.602
$\pm\Delta\mu$	0.053	0.056	0.011	0.0167	0.08	0.023
0.36 - 0.39 [rad]	0.716	0.949	0.982	0.990	0.903	0.632
$\pm\Delta\mu$	0.02	0.014	0.018	0.0075	0.029	0.02
0.39 - 0.42 [rad]	0.7187	0.9785	0.9787	0.966	0.9478	0.662
$\pm\Delta\mu$	0.0168	0.0043	0.0105	0.046	0.0063	0.011
0.42 - 0.45 [rad]	0.8279	0.979	0.9676	0.9728	0.9377	0.6515
$\pm\Delta\mu$	0.0267	0.0087	0.0039	0.0035	0.009	0.0257
0.45 - 0.48 [rad]	0.744	0.9936	0.9734	0.950	0.9401	0.674
$\pm\Delta\mu$	0.0212	0.0015	0.0029	0.006	0.0117	0.009
0.48 - 0.53 [rad]	0.7289	0.988	0.9726	0.951	0.920	0.6408
$\pm\Delta\mu$	0.01414	0.0015	0.0028	0.0026	0.00377	0.006

Table 7: *Kaon efficiencies in 2D ($p-\theta$) plane for Data*

Table 8 shows the mis-identification values for Data in 2D (momentum, polar angle) double bins for pions.

π^{Data}_{misID}	0.3 - 1.0 [GeV/c]	1.0 - 1.7 [GeV/c]	1.7 - 2.4 [GeV/c]	2.4 - 3.1 [GeV/c]	3.1 - 3.8 [GeV/c]	$>$ 3.8 [GeV/c]
0.3 - 0.36 [rad]	0.119	0.0626	0.076	0.0439	0.0417	0.108
$\pm\Delta\mu$	0.002	0.0083	0.006	0.0035	0.006	0.035
0.36 - 0.39 [rad]	0.0127	0.1146	0.080	0.0568	0.067	0.201
$\pm\Delta\mu$	0.002	0.0066	0.0108	0.0046	0.008	0.0268
0.39 - 0.42 [rad]	0.010	0.107	0.0885	0.0679	0.1156	0.1858
$\pm\Delta\mu$	0.002	0.0056	0.0046	0.0044	0.0055	0.010
0.42 - 0.45 [rad]	0.0226	0.0964	0.085	0.0937	0.154	0.208
$\pm\Delta\mu$	0.0023	0.0045	0.004	0.0044	0.006	0.01
0.45 - 0.48 [rad]	0.0308	0.1117	0.10	0.0937	0.1768	0.216
$\pm\Delta\mu$	0.002	0.0057	0.005	0.0041	0.0067	0.008
0.48 - 0.53 [rad]	0.0399	0.132	0.1275	0.1131	0.207	0.244
$\pm\Delta\mu$	0.0024	0.0056	0.004	0.0036	0.006	0.0079

Table 8: *Pion mis-identification in 2D ($p-\theta$) plane for Data*

Table 9 shows the efficiency values for MC in 2D (momentum, polar angle) double bins for kaons.

K^{MC}_{eff}	0.3 - 1.0 [GeV/c]	1.0 - 1.7 [GeV/c]	1.7 - 2.4 [GeV/c]	2.4 - 3.1 [GeV/c]	3.1 - 3.8 [GeV/c]	$>$ 3.8 [GeV/c]
0.3 - 0.36 [rad]	0.823	0.8644	0.840	0.883	0.845	0.80
$\pm\Delta\mu$	0.02	0.022	0.025	0.0072	0.0056	0.0227
0.36 - 0.39 [rad]	0.806	0.948	0.9732	0.991	0.935	0.90
$\pm\Delta\mu$	0.024	0.003	0.002	0.0013	0.004	0.047
0.39 - 0.42 [rad]	0.733	0.9694	0.9659	0.960	0.919	0.868
$\pm\Delta\mu$	0.026	0.0018	0.002	0.005	0.0058	0.0349
0.42 - 0.45 [rad]	0.766	0.979	0.955	0.956	0.8376	0.845
$\pm\Delta\mu$	0.0124	0.003	0.003	0.0029	0.022	0.015
0.45 - 0.48 [rad]	0.794	0.980	0.968	0.974	0.962	0.900
$\pm\Delta\mu$	0.0086	0.0033	0.002	0.0017	0.002	0.027
0.48 - 0.53 [rad]	0.8644	0.9559	0.964	0.968	0.956	0.893
$\pm\Delta\mu$	0.0227	0.0017	0.0016	0.0029	0.0029	0.0029

Table 9: *Kaon efficiencies in 2D ($p-\theta$) plane for MC*

Table 10 shows the mis-identification values for MC in 2D (momentum, polar angle) double bins for pions.

π^{MC}_{misID}	0.3 - 1.0 [GeV/c]	1.0 - 1.7 [GeV/c]	1.7 - 2.4 [GeV/c]	2.4 - 3.1 [GeV/c]	3.1 - 3.8 [GeV/c]	$>$ 3.8 [GeV/c]
0.3 - 0.36 [rad]	0.00679	0.074	0.071	0.0477	0.0537	0.137
$\pm\Delta\mu$	0.00077	0.0039	0.0053	0.002	0.003	0.0076
0.36 - 0.39 [rad]	0.0116	0.069	0.074	0.012	0.097	0.1809
$\pm\Delta\mu$	0.0015	0.003	0.0035	0.0025	0.004	0.006
0.39 - 0.42 [rad]	0.019	0.103	0.0826	0.085	0.119	0.185
$\pm\Delta\mu$	0.0016	0.0036	0.0026	0.003	0.0053	0.005
0.42 - 0.45 [rad]	0.026	0.105	0.098	0.100	0.1388	0.233
$\pm\Delta\mu$	0.0015	0.0034	0.003	0.003	0.0035	0.0096
0.45 - 0.48 [rad]	0.0339	0.1142	0.112	0.1037	0.163	0.238
$\pm\Delta\mu$	0.0017	0.0026	0.0026	0.0025	0.0037	0.0056
0.48 - 0.53 [rad]	0.042	0.124	0.1299	0.122	0.192	0.243
$\pm\Delta\mu$	0.0015	0.002	0.0026	0.0024	0.003	0.0046

Table 10: *Pion mis-identification in 2D $(p-\theta)$ plane for MC*

Fig. 49 shows the 2D efficiency frame for kaons and mis-identification frame for pions based on Data results.

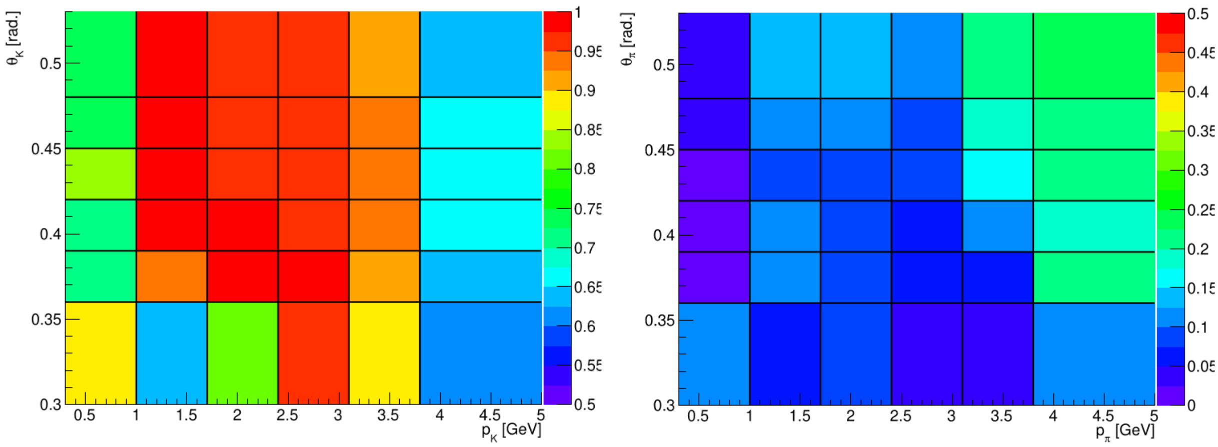

(a) (b)

Figure 49: *2D efficiency plot for kaon(a) and mis-identification plot(b) for pion based on Data results.*

Fig. 50 shows the 2D efficiency frame for kaons and mis-identification frame for pions based on MC results.

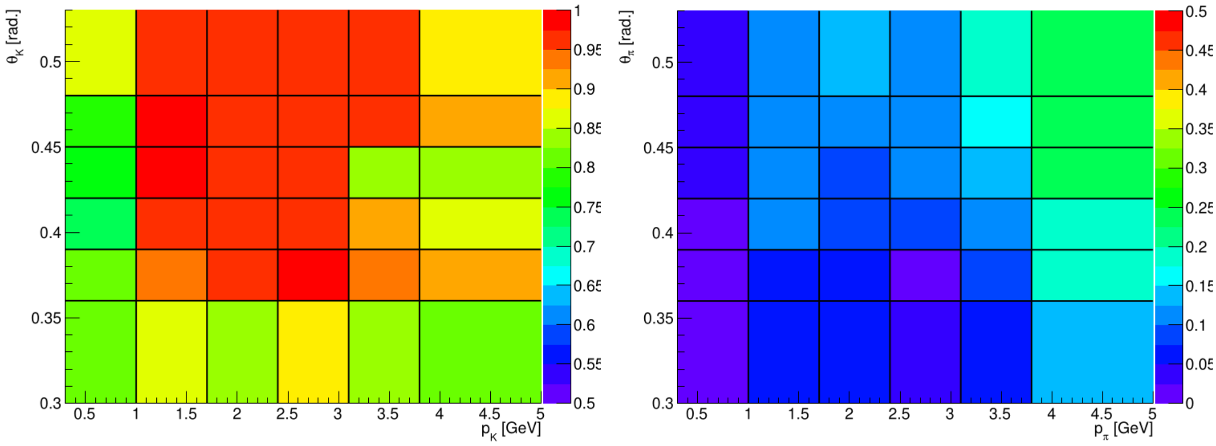

(a) (b)

Figure 50: *2D efficiency plot for kaon(a) and mis-identification plot(b) for pion based on MC results.*

As can be seen in Figs. 49 (a) and 50 (a), the kaon efficiency is low for low- and high-momentum bins, meanwhile, it is higher for middle-momentum and high-polar angle bins. Furthermore, as can be noticed in Figs. 49 (b) and 50 (b), the pion mis-identification probability is low for small momentum bins and higher for high momentum bins, which explains the low kaon efficiency in high-momentum bins. Moreover, there is good agreement between Data (Fig. 49) and MC (Fig. 50) samples for the kaon detection efficiency and pion mis-identification probability values in the 2D frame.

Table 11 shows the efficiency values for Data in 2D (momentum, polar angle) double bins for pions.

π^{Data}_{eff}	0.3 - 1.0 [GeV/c]	1.0 - 1.7 [GeV/c]	1.7 - 2.4 [GeV/c]	2.4 - 3.1 [GeV/c]	3.1 - 3.8 [GeV/c]	$>$ 3.8 [GeV/c]
0.3 - 0.36 [rad]	0.62	0.8028	0.9306	0.963	0.9457	0.8515
$\pm\Delta\mu$	0.03	0.0198	0.038	0.009	0.024	0.0177
0.36 - 0.39 [rad]	0.7835	0.8609	0.917	0.8847	0.788	0.944
$\pm\Delta\mu$	0.025	0.0111	0.012	0.0137	0.048	0.022
0.39 - 0.42 [rad]	0.676	0.908	0.871	0.891	0.823	0.903
$\pm\Delta\mu$	0.028	0.0129	0.0073	0.0098	0.009	0.017
0.42 - 0.45 [rad]	0.642	0.844	0.8825	0.9009	0.897	0.80
$\pm\Delta\mu$	0.014	0.012	0.011	0.0104	0.008	0.028
0.45 - 0.48 [rad]	0.623	0.8808	0.8628	0.926	0.989	0.8928
$\pm\Delta\mu$	0.012	0.0116	0.016	0.0049	0.0028	0.025
0.48 - 0.53 [rad]	0.6986	0.876	0.883	0.907	0.919	0.8515
$\pm\Delta\mu$	0.010	0.0049	0.0043	0.0038	0.0049	0.009

Table 11: *Pion efficiencies in 2D* $(p - \theta)$ *plane for Data*

Table 12 shows the mis-identification values for Data in 2D (momentum, polar angle) double bins for kaons.

K^{Data}_{misID}	0.3 - 1.0 [GeV/c]	1.0 - 1.7 [GeV/c]	1.7 - 2.4 [GeV/c]	2.4 - 3.1 [GeV/c]	3.1 - 3.8 [GeV/c]	$>$ 3.8 [GeV/c]
0.3 - 0.36 [rad]	0.0967	0.116	0.057	0.06	0.0201	0.0165
$\pm\Delta\mu$	0.014	0.0131	0.0035	0.0039	0.0034	0.0022
0.36 - 0.39 [rad]	0.104	0.0996	0.0709	0.0497	0.034	0.0292
$\pm\Delta\mu$	0.026	0.008	0.0075	0.0046	0.0036	0.003
0.39 - 0.42 [rad]	0.1345	0.0915	0.0858	0.055	0.0425	0.0498
$\pm\Delta\mu$	0.0146	0.0066	0.005	0.0049	0.0042	0.0038
0.42 - 0.45 [rad]	0.1311	0.1235	0.0811	0.0413	0.2115	0.0508
$\pm\Delta\mu$	0.0156	0.0084	0.0059	0.00397	0.0096	0.0045
0.45 - 0.48 [rad]	0.1287	0.006	0.094	0.095	0.0512	0.0669
$\pm\Delta\mu$	0.0099	0.1217	0.0049	0.0203	0.0045	0.004
0.48 - 0.53 [rad]	0.1247	0.1303	0.1118	0.116	0.108	0.077
$\pm\Delta\mu$	0.0067	0.0045	0.0042	0.004	0.0049	0.003

Table 12: *Kaon mis-identification in 2D* $(p - \theta)$ *plane for Data*

Table 13 shows the efficiency values for MC in 2D (momentum, polar angle) double bins for pions, meanwhile Table 14 shows the mis-identification values for MC in 2D (momentum, polar angle) double bins for kaons.

π_{eff}^{MC}	0.3 - 1.0 [GeV/c]	1.0 - 1.7 [GeV/c]	1.7 - 2.4 [GeV/c]	2.4 - 3.1 [GeV/c]	3.1 - 3.8 [GeV/c]	>3.8 [GeV/c]
0.3 - 0.36 [rad]	0.555	0.951	0.886	0.920	0.8188	0.979
$\pm\Delta\mu$	0.014	0.0095	0.012	0.02	0.017	0.011
0.36 - 0.39 [rad]	0.625	0.836	0.85	0.848	0.911	0.956
$\pm\Delta\mu$	0.0144	0.010	0.006	0.025	0.0169	0.015
0.39 - 0.42 [rad]	0.612	0.798	0.819	0.8736	0.846	0.820
$\pm\Delta\mu$	0.0119	0.0066	0.00670	0.016	0.024	0.0077
0.42 - 0.45 [rad]	0.623	0.830	0.830	0.8708	0.8597	0.822
$\pm\Delta\mu$	0.0099	0.004	0.012	0.003	0.0047	0.006
0.45 - 0.48 [rad]	0.57	0.847	0.8667	0.875	0.8859	0.861
$\pm\Delta\mu$	0.0057	0.0036	0.006	0.0029	0.0038	0.0095
0.48 - 0.53 [rad]	0.63	0.846	0.8575	0.871	0.8746	0.856
$\pm\Delta\mu$	0.006	0.002	0.0034	0.0028	0.004	0.0056

Table 13: *Pion efficiencies in 2D ($p-\theta$) plane for MC*

K_{misID}^{MC}	0.3 - 1.0 [GeV/c]	1.0 - 1.7 [GeV/c]	1.7 - 2.4 [GeV/c]	2.4 - 3.1 [GeV/c]	3.1 - 3.8 [GeV/c]	>3.8 [GeV/c]
0.3 - 0.36 [rad]	0.09	0.1399	0.061	0.032	0.023	0.0135
$\pm\Delta\mu$	0.005	0.005	0.0022	0.0019	0.002	0.0018
0.36 - 0.39 [rad]	0.096	0.119	0.074	0.0027	0.032	0.1502
$\pm\Delta\mu$	0.006	0.0034	0.0028	0.002	0.002	0.009
0.39 - 0.42 [rad]	0.134	0.1209	0.078	0.057	0.049	0.0583
$\pm\Delta\mu$	0.0066	0.0036	0.0029	0.002	0.002	0.0026
0.42 - 0.45 [rad]	0.1174	0.117	0.0592	0.07	0.062	0.0766
$\pm\Delta\mu$	0.0044	0.003	0.002	0.002	0.0029	0.0029
0.45 - 0.48 [rad]	0.1222	0.1212	0.095	0.0935	0.088	0.093
$\pm\Delta\mu$	0.0044	0.003	0.003	0.0026	0.0024	0.004
0.48 - 0.53 [rad]	0.1399	0.1278	0.112	0.111	0.102	0.108
$\pm\Delta\mu$	0.00529	0.0028	0.002	0.002	0.00199	0.0024

Table 14: *Kaon mis-identification in 2D ($p-\theta$) plane for MC*

Fig. 51 shows the 2D efficiency frame for pions and mis-identification frame for kaons based on Data results.

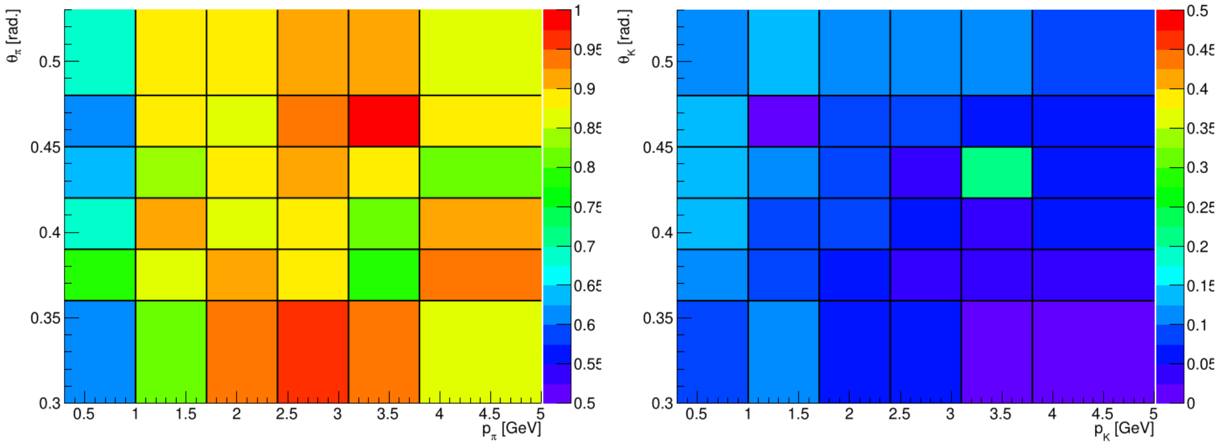

(a) (b)

Figure 51: *2D efficiency plot for pion(a) and mis-identification kaon(b) for pion based on Data results.*

Fig. 52 shows the 2D efficiency frame for pions and mis-identification frame for kaons based on MC results.

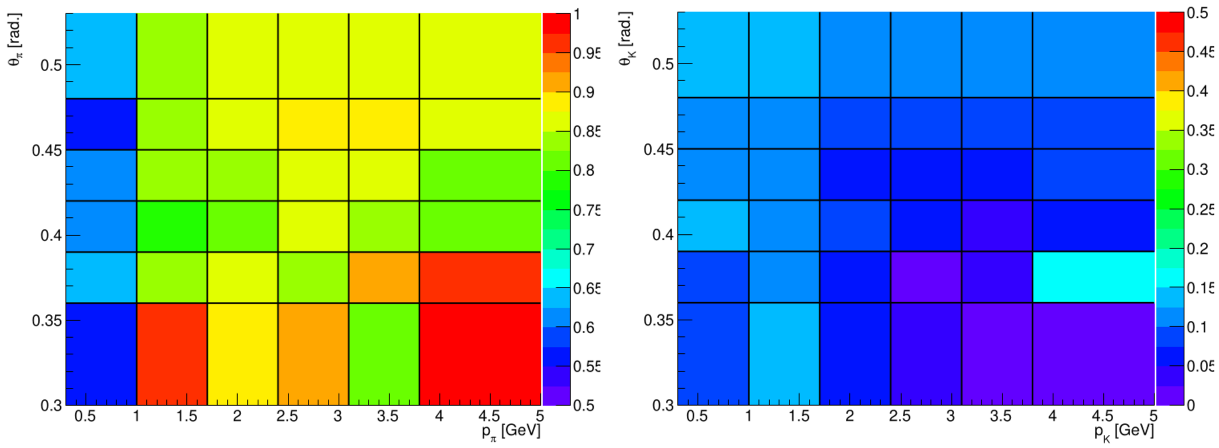

(a) (b)

Figure 52: *2D efficiency plot for pion(a) and mis-identification plot(b) for kaon based on MC results.*

As can be seen in Figs. 51 (a) and 52 (a), the pion efficiency is low for low-momentum bins, meanwhile, it is higher for middle- and high-momentum bins. Moreover, those 2D results prove the noticeable difference between Data and MC for pion efficiencies which was caused due to a release problem. Furthermore, as can be noticed in Figs. 51 (b) and 52 (b), the pion mis-identification probability is low for all momentum bins and there is good agreement between Data and MC samples for kaon mis-identification.

The ratio $L_\pi/(L_\pi + L_K)$, where the likelihood L_i for a pion or kaon hypothesis combines PID information from all sub-detectors was used to separate final states into exclusive samples and to further reduce backgrounds for many Belle II analyses [29] [30] [31] [32], where pion/kaon separation is essential to reconstruct many investigated decays of B, D and other decaying particles. For decays with one pion and one kaon in the final state, the events in which both tracks are identified as pions or kaons were discarded. In addition, the polar angle of the prompt $h^\pm$ in the laboratory frame is restricted to be within the acceptance of the PID detectors. The PID requirement correctly identifies on average 94%(Data)/96%(MC) of kaons and 87%(Data)/84%(MC) of pions.

5.5 R variable dependence

In therms of this study some other important checks were performed as well. One of them is efficiency and mis-identification probability dependence check on $R_{K/\pi}$ and $R_{\pi/K}$ selection. It is very interesting and useful to see the detection efficiency behavior with respect to different values of R. Table 15 shows the efficiency and mis-identification probability values for kaons and pions for Data and MC over R values. As the lowest value was chosen $R = 0.6$ and the highest value is $R = 0.9$.

R_{value}	0.60	0.6	0.70	0.75	0.80	0.85	0.9
K_{eff}^{MC}	0.9349	0.9285	0.9212	0.912	0.9012	0.8869	0.8667
$\pm\Delta\mu$	0.0009	0.0009	0.0009	0.001	0.001	0.0012	0.00121
K_{eff}^{Data}	0.9243	0.9199	0.914	0.908	0.9014	0.8912	0.8778
$\pm\Delta\mu$	0.002	0.002	0.002	0.002	0.002	0.0022	0.0023
π_{eff}^{MC}	0.8177	0.8139	0.8095	0.8048	0.800	0.794	0.7856
$\pm\Delta\mu$	0.00136	0.00138	0.00139	0.0014	0.001416	0.00142	0.00144
π_{eff}^{Data}	0.8654	0.8618	0.8582	0.8542	0.8492	0.8439	0.8368
$\pm\Delta\mu$	0.003	0.003	0.003	0.003	0.0031	0.0031	0.0031
K_{misID}^{MC}	0.059	0.090	0.0964	0.091	0.090	0.0894	0.0848
$\pm\Delta\mu$	0.059	0.090	0.0964	0.091	0.090	0.0894	0.0848
K_{misID}^{Data}	0.0976	0.0974	0.0969	0.0966	0.0958	0.0949	0.0939
$\pm\Delta\mu$	0.00197	0.0017	0.0017	0.0017	0.0019	0.0019	0.0019
π_{misID}^{MC}	0.109	0.108	0.1068	0.1049	0.1035	0.1003	0.0977
$\pm\Delta\mu$	0.0007	0.0007	0.0007	0.00079	0.00069	0.0008	0.0010
π_{misID}^{Data}	0.099	0.089	0.0969	0.0958	0.0946	0.092	0.0904
$\pm\Delta\mu$	0.0033	0.00311	0.0031	0.0029	0.003	0.0026	0.0025

Table 15: *The efficiency and mis-identification probability values for kaons and pions for Data and MC over the R values*

As we can see from the results obtained, $kaon efficiency$ is at its maximum at $R_{cut} = 0.6$ point and is about 93% for MC and 92% for Data. Detection efficiency decreases with growth of R_{cut} reaching its lowest value at $R_{cut} = 0.9$, which is approximately 87% for MC and 88% for Data. The same behavior shows the *pion* detection efficiency which has its highest value at $R_{cut} = 0.6$

point and is about 81% for MC and 86% for Data. Meanwhile at $R_{cut} = 0.9$ *pion* detection efficiency is 78% for MC and 83% for Data.

Furthermore, the pion mis-identification probability is mainly constant on average about 9-10%.

The plots in Fig. 57 show fitted $D^0\bar{D}^0$ invariant mass distributions using the R_{cut} binning from Table 15 for MC *kaons* in ARICH acceptance. (a) column is our true kaon list which has been detected in ARICH acceptance without any ID cut. In column (b), there is a list of kaons with $R_{K/\pi} > X$ PID cut applied and in column (c) are the kaons with $R_{\pi/K} > X$, where X changes from 0.60 to 0.90.

MC Kaons $\mathbf{R_{cut}} > 0.60$;

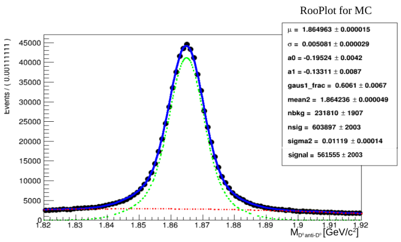

(a)

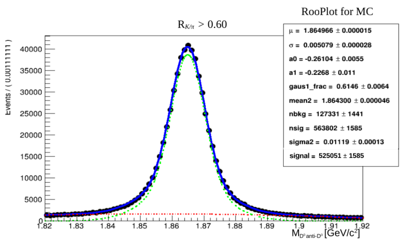

(b)

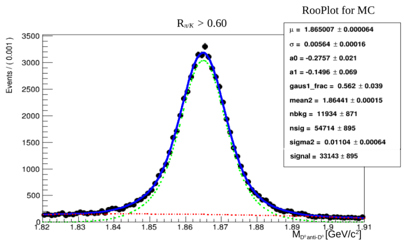

(c)

MC Kaons $\mathbf{R_{cut}} > 0.65$

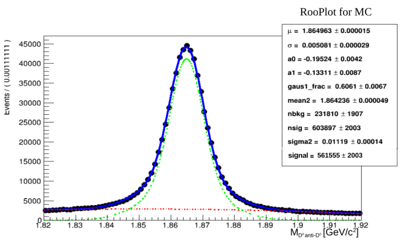

(a)

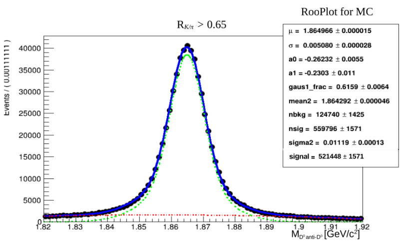

(b)

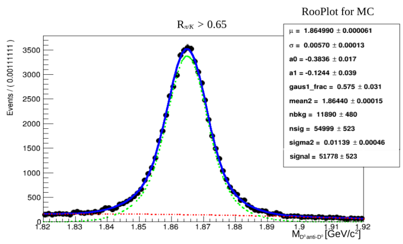

(c)

MC Kaons $\mathbf{R_{cut}} > 0.70$;

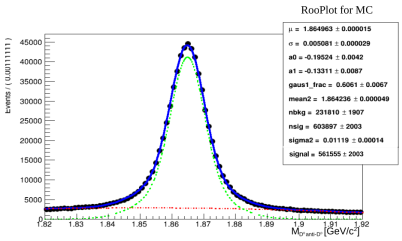

(a)

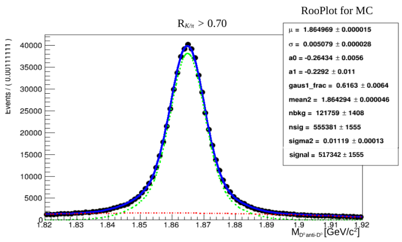

(b)

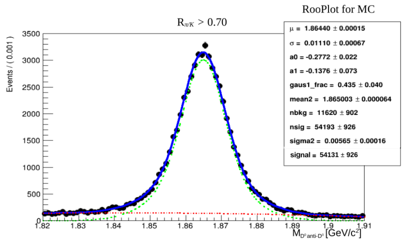

(c)

MC Kaons $\mathbf{R_{cut}} > 0.75$

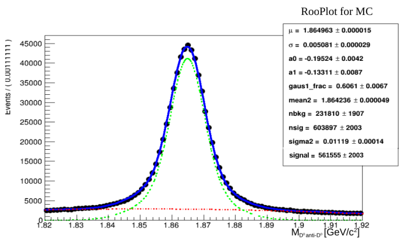

(a)

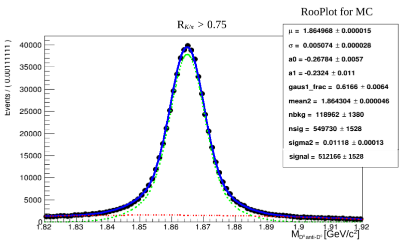

(b)

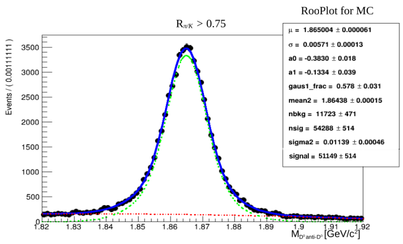

(c)

MC Kaons $\mathbf{R_{cut}} > 0.80$;

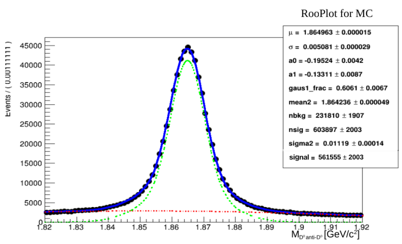

(a)

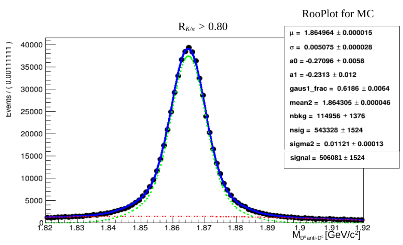

(b)

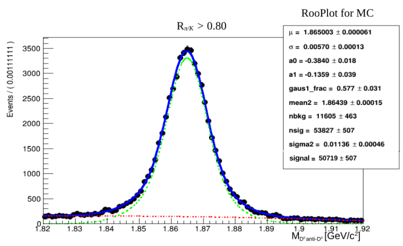

(c)

MC Kaons $\mathbf{R_{cut}} > 0.85$

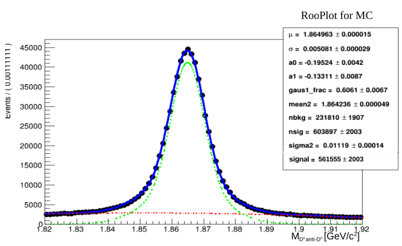

(a)

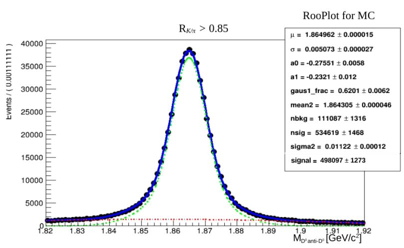

(b)

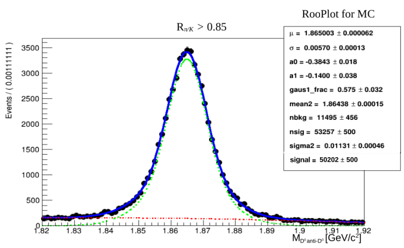

(c)

MC Kaons $R_{cut} > 0.90$;

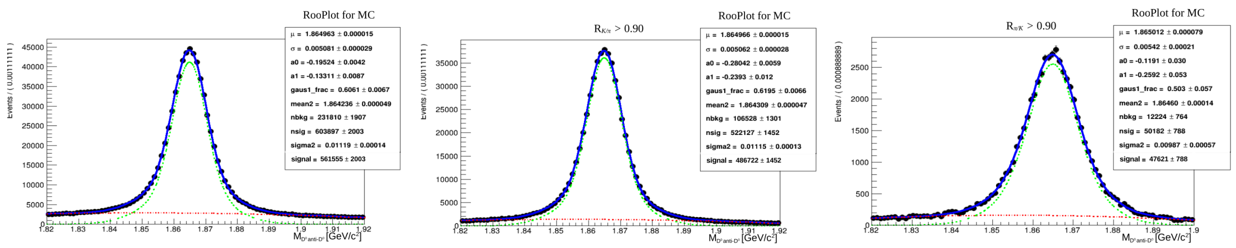

(a) (b) (c)

Figure 57: Invariant mass distributions for Kaons from MC

Fig. 58 shows the efficiency and mis-identification probability values with respect to the R variable for kaons and pions obtained for Data and MC on a graph frame.

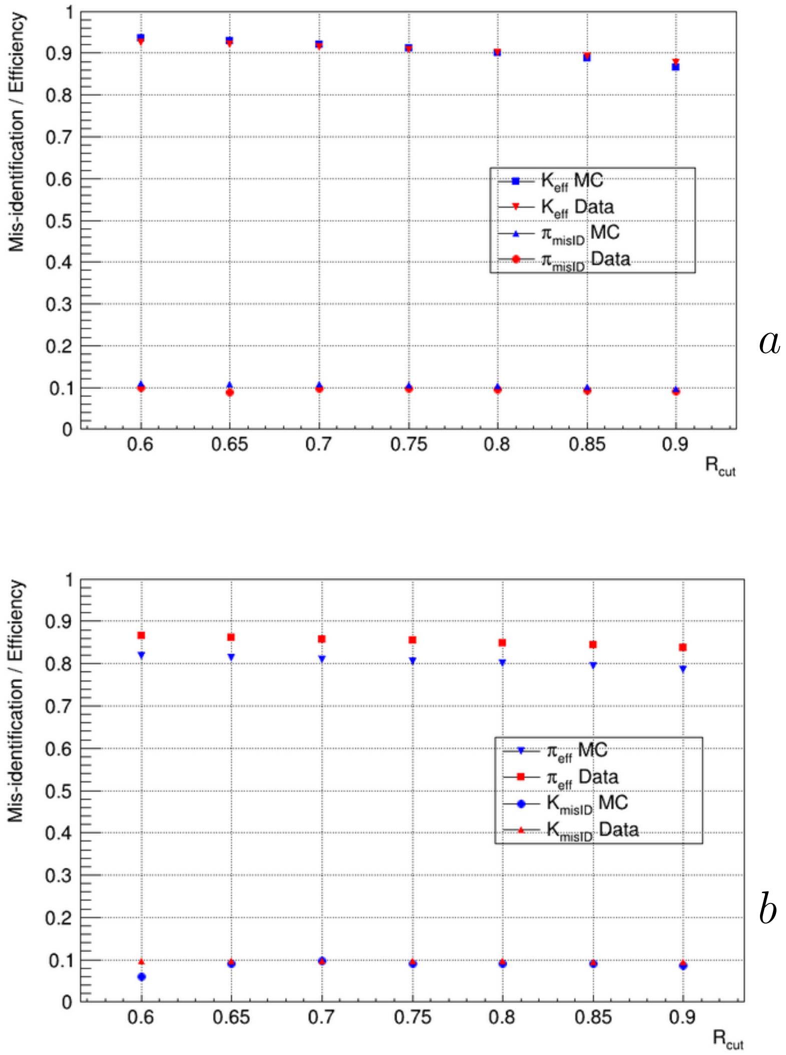

Figure 58: *Efficiency and misID studies depending on R variable.*

As we can see from obtained results there is a good agreement between Data and MC samples for kaon efficiencies and pion mis-identification probabilities(Fig. 58(a)).

Meanwhile, for pion detection efficiency (Fig. 58(b)) we see a shifted results between Data and MC. Detection efficiency for Data on average estimated about 4-5% is higher from the MC results. This phenomenon has been noticed in other Belle II analyses and was related to $release06$. This problem exists only in $release06$ and was fixed in higher releases. Whereas the kaon mis-identification probability is mainly constant and in average it is about 9-10%.

5.6 Q variable dependence

Another check which has been done in terms of this study is the efficiency and mis-identification probability dependence check from the Q variable, which is the energy released in $D^{*\pm} \rightarrow D^0(\bar{D}^0)\pi^\pm \rightarrow (K^\mp\pi^\pm)\pi^\pm$ decay.

Table 16 shows the efficiency and mis-identification probability values for kaons and pions for Data and MC over the Q values. As the lowest value was chosen $Q = 0.010[GeV]$ and the highest value is $Q = 0.040[GeV]$

Q_{value}	0.010	0.015	0.020	0.025	0.030	0.035	0.040
K_{eff}^{MC}	0.934	0.918	0.916	0.9165	0.9146	0.914	0.9154
$\pm\Delta\mu$	0.001	0.00086	0.00094	0.00099	0.0012	0.00145	0.0013
K_{eff}^{Data}	0.92446	0.9264	0.9295	0.9713	0.966	0.967	0.927
$\pm\Delta\mu$	0.00245	0.00273	0.0029	0.003	0.0023	0.0039	0.0028
π_{eff}^{MC}	0.8177	0.8177	0.80	0.826	0.840	0.794	0.8058
$\pm\Delta\mu$	0.0013	0.0015	0.0019	0.0016	0.0022	0.0015	0.0016
π_{eff}^{Data}	0.8833	0.88299	0.87077	0.903	0.8674	0.8338	0.832
$\pm\Delta\mu$	0.0039	0.0042	0.0024	0.003	0.0026	0.0036	0.0037
K_{misID}^{MC}	0.092	0.0946	0.096	0.0965	0.0981	0.0997	0.1017
$\pm\Delta\mu$	0.0008	0.0007	0.00096	0.00096	0.0013	0.00098	0.0009
K_{misID}^{Data}	0.105	0.1058	0.1069	0.108	0.1086	0.1083	0.1087
$\pm\Delta\mu$	0.0017	0.00214	0.00216	0.0023	0.00236	0.0021	0.0022
π_{misID}^{MC}	0.108	0.112	0.113	0.1167	0.1207	0.116	0.119
$\pm\Delta\mu$	0.0009	0.001	0.001	0.0011	0.00089	0.00098	0.0008
π_{misID}^{Data}	0.103	0.104	0.106	0.1129	0.109	0.105	0.1059
$\pm\Delta\mu$	0.004	0.0024	0.0026	0.003	0.003	0.003	0.0022

Table 16: *The efficiency and mis-identification probability values for kaons and pions for Data and MC over the Q values*

Fig. 59 shows the efficiency and misidentification probabilities on the Q dependence variable.

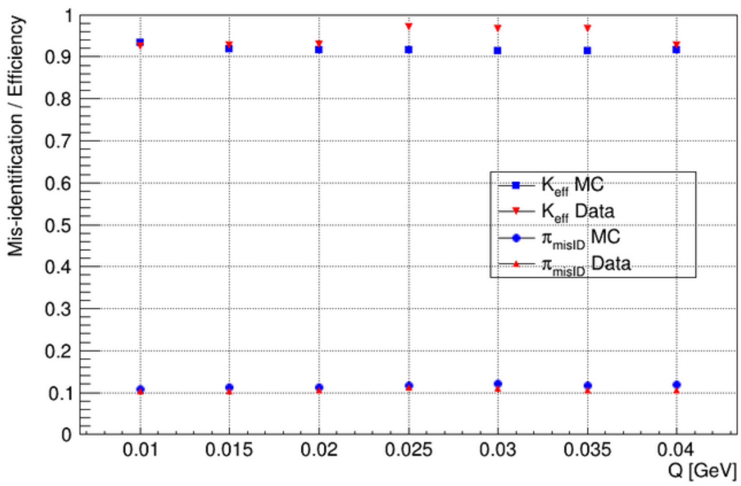

a

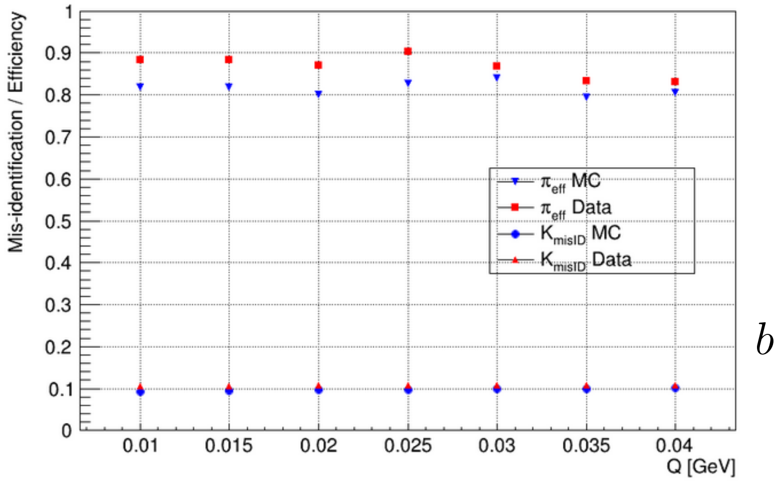

Figure 59: *Efficiency and misID dependencies on Q variable.*

The plots in Fig. 60 shows fitted $D^0\bar{D}^0$ invariant mass distributions using binning from table 16 for MC and Data for *kaons* in ARICH acceptance. (a) column is our true kaon list which has been detected in ARICH acceptance without any ID cut. In column (b), there is a list of kaons with $R_{K/\pi} > 0.6$ PID cut applied, and in column (c) are the kaons with $R_{\pi/K} > 0.6$.

MC Kaons , $0.0 < Q_{cut} < 0.010$

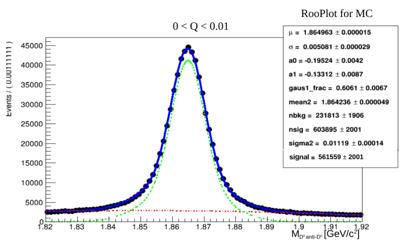

(a)

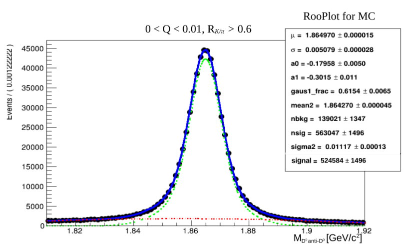

(b)

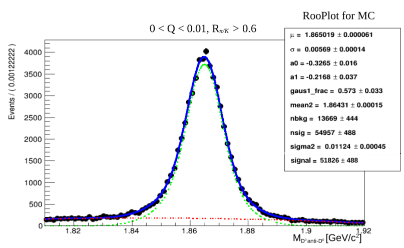

(c)

MC Kaons , $0.0 < Q_{cut} < 0.015$

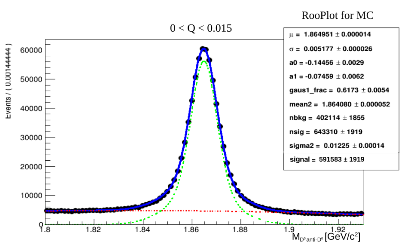

(a)

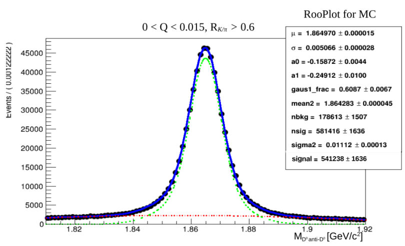

(b)

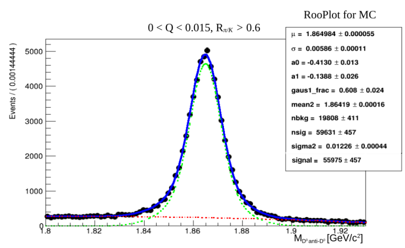

(c)

MC Kaons , $0.0 < Q_{cut} < 0.020$

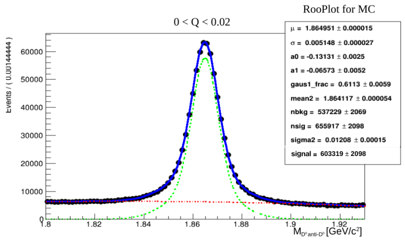

(a)

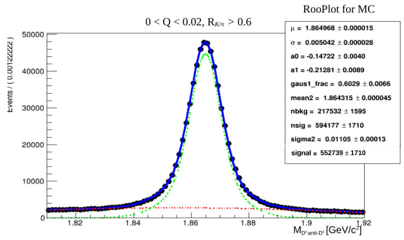

(b)

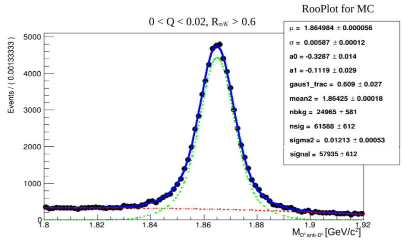

(c)

MC Kaons , $0.0 < Q_{cut} < 0.025$

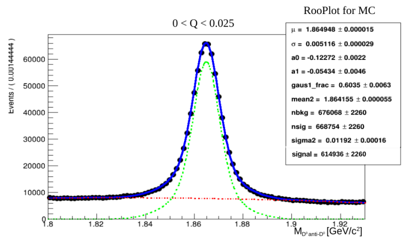

(a)

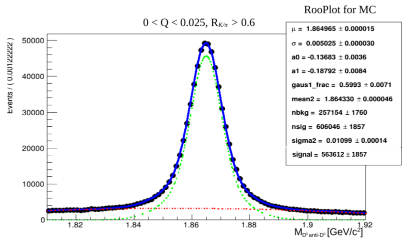

(b)

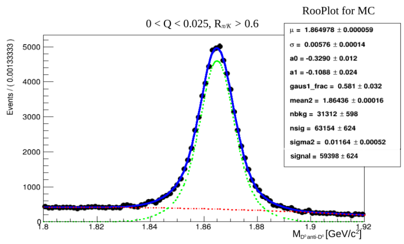

(c)

MC Kaons , $0.0 < Q_{cut} < 0.030$

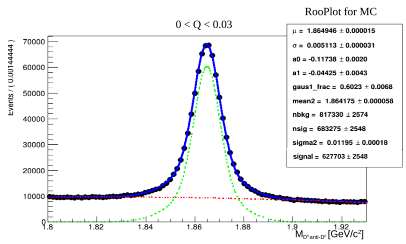

(a)

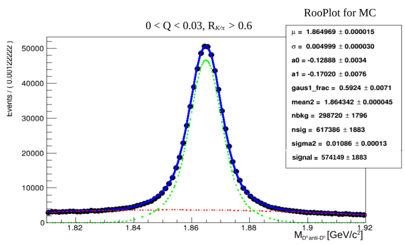

(b)

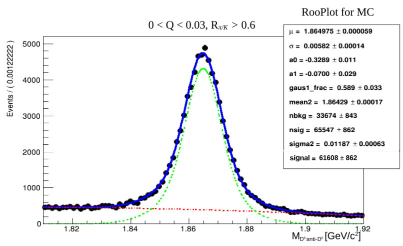

(c)

MC Kaons , $0.0 < Q_{cut} < 0.035$

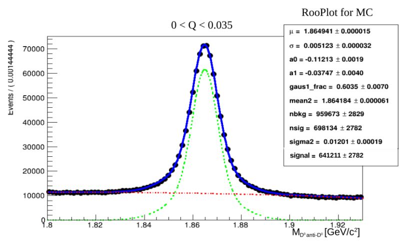

(a)

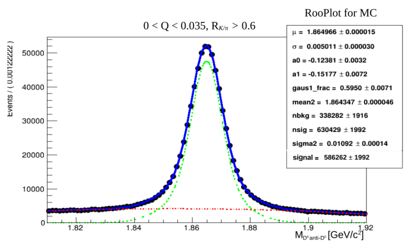

(b)

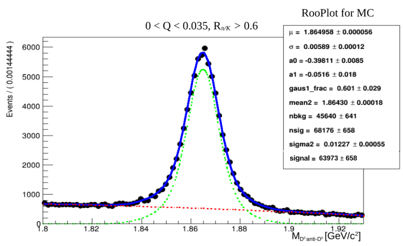

(c)

MC Kaons , $0.0 < Q_{cut} < 0.040$

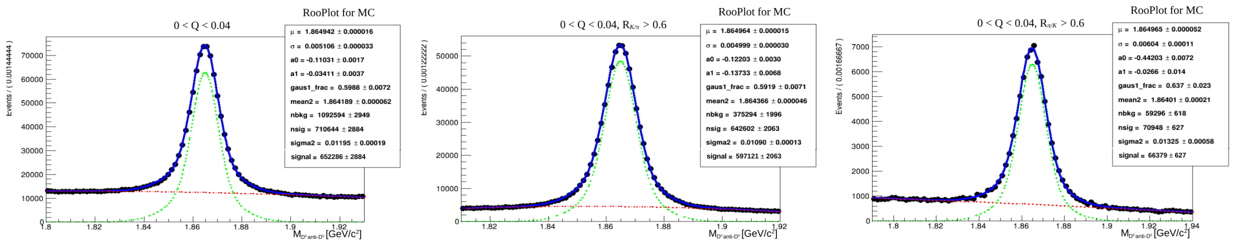

(a) (b) (c)

Figure 60: Invariant mass distributions for Kaons from MC

As we can see from the results obtained there is mainly a good agreement between Data and MC samples for kaon efficiencies(figure 58(a)) except for few points where we see that the efficiency obtained for Data is higher than that for the MC. Meanwhile, from (Fig. 58(b)) we see slightly shifted results for pion efficiencies between Data and MC samples. As was explained above, this is a release problem and was fixed in later releases. Furthermore, for pion(figure 58(a)) and kaon (figure 58(b)) mis-identification probabilities we see a good agreement between Data and MC. In general, kaon efficiency varies from 91.4-97.13% and for pions its 80-90%. Overall, the kaon mis-identification probability in average is about 9.2-10%, meanwhile for pions it is about 11-12%.

Conclusion

The physical program of Belle II experiment requires prompt reconstructions of different decaying particles, meaning the separation of final state hadrons. This is provided with the set of PID detectors, including the ARICH-aerogel Cherenkov detector, which is one of the most important ones. The separation is done with the combined PID information from all PID sub-detectors. Thus, the studies of ARICH performance performed during the preparation of this thesis are very important to provide an effective global PID. The efficiencies and mis-identification probabilities determined as a function of charged particle momentum or polar angle, as well as two-dimensional values of mentioned characteristics determined for both: momentum and angle, are essential ingredients for look-up tables used to be included into the final criteria of global PID. In order to extract the performance dependencies well known decays like $D^{*\pm} \to D^0(\bar{D}^0)\pi^{\pm} \to (K^{\mp}\pi^{\pm})\pi^{\pm}$ were reconstructed from Belle II data, also necessary Monte Carlo studies were performed to estimate possible backgrounds. In addition to momentum and polar angle dependencies, possible influence on track multiplicity will also be investigated.

Acknowledgement

WHEN YOU WANT SOMETHING, ALL THE UNIVERSE CONSPIRES IN HELPING YOU TO ACHIEVE IT.

- Paulo Coelho, The Alchemist

NORAYR AKOPOV - I would like to express my deepest gratitude to my supervisor, for his exceptional guidance, invaluable insights, and unwavering support throughout the course of this research. His expertise, patience, and encouragement have been instrumental in shaping this thesis. This work would not have been possible without your dedication and inspiration.

GEVORG KARYAN - I would like to extend my sincere gratitude to my group leader for his continuous support, leadership, and encouragement throughout this research. His insightful feedback, thoughtful advice, and collaborative spirit have been invaluable to the success of this project.

MY FELLOW COLLABORATORS - I would like to express my heartfelt thanks to my fellow group members for their collaboration, support, and friendship throughout this research process. Thank you for your constant encouragement, teamwork, and positive spirit.

MY FAMILY AND FRIENDS - I would like to express my deepest gratitude to my family and friends for their unwavering love, encouragement, and support throughout this entire journey.

I also thank EIF and PMI "PhD supporting program 2021" and Science Committee of the Republic of Armenia Grant no. 20TTCG-1C010 and Grant no. 23LCG-1C01 for supporting this proposal.

Bibliography

[1] E. Kou, P. Urquijo, and W. Altmannshofer. "The Belle II Physics Book." In: *Prog Theor Exp Phys* (2019). URL: hep-ex%20arXiv:1808.10567.

[2] M. Yonenaga, I. Adachi, and L. Burmistrov et al. "Performance evaluation of the aerogel RICH counter for the Belle II spectrometer using early beam collision data". In: *Prog Theor Exp Phys* (2020).

[3] L. Santelj et al. "Recent developments in data reconstruction for aerogel RICH at Belle II". In: *Nuclear Instruments and Methods in Physics Research Section A: Accelerators, Spectrometers, Detectors and Associated Equipment* (2023).

[4] J. Charles et al. "Future sensitivity to new physics in B_D,B_S, and K mixings". In: *Physical Review D* (2014).

[5] Thomas Keck. "Machine learning algorithms for the Belle II experiment and their validation on Belle data". In: *Inspire HEP* (2017).

[6] K. Adamczyk et al. A. Gabrielli. "The silicon vertex detector of the Belle II experiment". In: *Nuclear Instruments and Methods in Physics Research Section A: Accelerators, Spectrometers, Detectors and Associated Equipment* (2024).

[7] Bostjan Golob et al. AJ Bevan. "The physics of the B factories". In: *The European Physical Journal C 74.11* (2014).

[8] William R Leo. "Techniques for Nuclear and Particle Physics Experiments: A How-to Approach". In: *Springer-Verlag,* (1994).

[9] Manca Mrvar. "Calibration of Aerogel Ring-Imaging Cherenkov Detector in Belle II Spectrometer". In: *Doctoral Thesis* (2014).

[10] J Urgen Engelfried. "Ring Imaging Cherenkov Detectors". In: *AIP Conference Proceedings. Vol. 857. 2. AIP.* (2006).

[11] A Soleimani Dorcheh and MH Abbasi. "Silica aerogel; synthesis, properties and characterization". In: *materials processing technology 199.1-3* (2008).

[12] Masanobu Yonenaga. “Particle Identification using the Aerogel RICH Counter at the Belle II Experiment”. In: (2020).

[13] T. Iijima et al. “A Novel Type of Proximity Focusing RICH Counter with Multiple Refractive Index Aerogel Radiator”. In: *Nuclear Instruments and Methods in Physics Research Section A: Accelerators, Spectrometers, Detectors and Associated Equipment 548.3* (2005).

[14] Peter Krizan, Samo Korpar, and Toru Iijima. “Study of a Nonhomogeneous Aerogel Radiator in a Proximity Focusing RICH Detector”. In: *Nuclear Instruments and Methods in Physics Research Section A: Accelerators, Spectrometers, Detectors and Associated Equipment 565.2* (2006).

[15] R. Pestotnik et al. “Design Optimization of the Proximity Focusing RICH with Dual Aerogel Radiator Using a Maximum-Likelihood Analysis of Cherenkov Rings”. In: *Nuclear Instruments and Methods in Physics Research Section A: Accelerators, Spectrometers, Detectors and Associated Equipment* (2007).

[16] Makoto Tabata et al. “Large-Area Silica Aerogel for Use as Cherenkov Radiators with High Refractive Index, Developed by Supercritical Carbon Dioxide Drying”. In: *The Journal of Supercritical Fluids 110* (2016).

[17] I. Adachi et al. “Construction of Silica Aerogel Radiator System for Belle II RICH Counter”. In: *Nuclear Instruments and Methods in Physics Research Section A: Accelerators, Spectrometers, Detectors and Associated Equipment.* (2017).

[18] Makoto Tabata et al. “Assembly of a Silica Aerogel Radiator Module for the Belle II ARICH System”. In: *Proceedings of International Conference on Technology and Instrumentation in Particle Physics.* (2017).

[19] Y. Yusa et al. “Test of the HAPD Light Sensor for the Belle II Aerogel RICH”. In: *Nuclear Instruments and Methods in Physics Research Section A: Accelerators, Spectrometers, Detectors and Associated Equipment.* (2017).

[20] K. Ogawa et al. "Behavior of 144ch HAPDs for the Belle II Aerogel RICH in the Magnetic Field". In: *Proceedings of International Conference on Technology and Instrumentation in Particle Physics.* (2017).

[21] S. Korpar et al. "A 144-Channel HAPD for the Aerogel RICH at Belle II". In: *Nuclear Instruments and Methods in Physics Research Section A: Accelerators, Spectrometers, Detectors and Associated Equipment.* (2013).

[22] H. Kakuno et al. "Readout ASIC and electronics for the 144ch HAPD for Aerogel RICH at Belle II". In: *Nuclear Instruments and Methods in Physics Research Section A: Accelerators, Spectrometers, Detectors and Associated Equipment* (2014).

[23] R. Pestotnik et al. "Front-End Electronics of the Belle II Aerogel Ring Imaging Detector". In: *Nuclear Instruments and Methods in Physics Research Section A: Accelerators, Spectrometers, Detectors and Associated Equipment* (2018).

[24] S. Nishida et al. "Readout ASICs and Electronics for the 144-channel HAPDs for the Aerogel RICH at Belle II". In: *Physics Procedia* (2012).

[25] S. Nishida et al. "Development of the readout ASIC for the 144ch HAPD for aerogel RICH". In: *Nuclear Instruments and Methods in Physics Research Section A: Accelerators, Spectrometers, Detectors and Associated Equipment* (2010).

[26] Ichiro Adachi et al. Makoto Tabata. "Progress in the development of silica aerogel as a RICH radiator in the Belle II experiment". In: *Nuclear Science Symposium and Medical Imaging Conference (NSS/MIC* (2013).

[27] Lawrence W. Hrubesh. "Aerogel applications". In: *Journal of Non-Crystalline Solids* (1998).

[28] W. Altmannshofer et al. In: *PTEP* (2019).

[29] I. Adachi et al. (Belle II Collaboration). "Measurement of branching fractions and direct CP asymmetries for $B \to K\pi$ and $B \to \pi\pi$ decays at Belle II". In: *Physical Review D* (2024).

[30] I. Adachi et al. (Belle II Collaboration). "Search for a long-lived spin-0 mediator in b $\rightarrow$ s transitions at the Belle II experiment". In: *Physical Review D* (2023).

[31] The Belle and Belle II collaborations (I. Adachi et al.) "Measurement of CP asymmetries and branching-fraction ratios for $B\pm \rightarrow DK^{\pm}$ *and* $D\pi^{\pm}$ *with* $D \rightarrow K_S^0 K^{\pm}\ \pi^{\mp}$ using Belle and Belle II data". In: *Journal of High Energy Physics* (2023).

[32] The Belle and Belle II collaborations (I. Adachi et al.) "Measurement of branching-fraction ratios and CP asymmetries in $B^{\pm} \rightarrow D_{CP\pm}K^{\pm}$ decays at Belle and Belle II". In: *Journal of High Energy Physics* (2023).

[33] The Belle and Belle II collaborations (I. Adachi et al.) "Measurement of the energy dependence of the $e^+e^- \rightarrow B\bar{B}, B\bar{B}^*$, *and* $B^{*-}B^*$ *cross sections at Belle II*". In: *Journal of High Energy Physics* (2024).

[34] T. Nakamura, G. Iwai, and H. Matsunaga et al. "Development of stable Grid service at the next generation system of KEKCC". In: *J. Phys.* (2017).

[35] T. Sjostrand, S. Ask, and J. R. Christiansen et al. "An Introduction to PYTHIA 8.2". In: *Comput.Phys.* (2015).

[36] S. Agostinelli et al. "Geant4 - a simulation toolkit". In: *Nucl. Instrum. Meth. A .* (2003).

[37] T. Kuhr et al. "The Belle II Core Software". In: *Comput. Softw. Big Sci.* (2019).

[38] F. Abudin en, N. Akopov, and A. Aloisio et al. "B-flavor tagging at Belle II". In: *Eur. Phys.J. C* (2022).

[39] F. Abudin en, I. Adachiba, and K. Adamczyk et al. "Precise measurement of the D^0 and D^+ lifetimes at Belle II". In: *Phys.Rev.Lett.* (2021).

[40] F. Abudin, I. Adachi, and K. Adamczyk et al. "Search for B^+K^+ Decays Using an Inclusive Tagging Method at Belle II". In: *Phys.Rev.Lett.* (2021).

[41] Q.-D. ZHOU. “Correction for tracking momentum bias based on invariant mass peak studies”. In: *BELLE2-NOTE-PH-2020-030* (2020).

[42] G. Ghevondyan. “Performance study of the aerogel RICH at the Belle II experiment”. In: *Nuclear Instruments and Methods in Physics Research Section A: Accelerators, Spectrometers, Detectors and Associated Equipment* (2023).

[43] N. Akopov and G. Ghevondyan et al. “Investigations of Characteristics for Arich Detector with Mesons Decay at Belle II Experiment Using the Monte Carlo Method”. In: *Journal of Contemporary Physics (Armenian Academy of Sciences)* (2023).

[44] In: (). URL: `https://root.cern/doc/master/group%20tutorial%20roofit.html`.

List of Codes

$\mathbf{D^{*+} \to D^0\pi^+}$ reconstruction code

```
#!/usr/bin/env python3
# -*- coding: utf-8 -*-

import basf2 as b2
import modularAnalysis as ma
import variables.collections as vc
import variables.utils as vu
from variables import variables
from vertex import *
from variables import variables
from basf2 import *
from modularAnalysis import *
import sys

my_path = b2.Path()

inputMdst('default','/belle/MC/release-06-00-08/DB00002100/
MC15ri_b/prod00024787/s00/e1003/4S/r00000/ccbar/mdst/
sub*/*.root', path=my_path)

outfilename = 'ccbar.root'

b2.conditions.prepend_globaltag('tracking_data_Moriond23_v1')

# create and fill the ParticleLists
```

```
#######################################################
fillParticleList('pi+:all', '', path=my_path)
fillParticleList('K-:all', '', path=my_path)

# track level cuts
#######################################################
trackCutsplus = '[dr < 2.0] and [abs(dz) < 5.0] and [pt > 0.1]
and [charge > 0] and [pValue > 0.001] and [p > 0.3]'
trackCuts = '[dr < 2.0] and [abs(dz) < 5.0] and [pt > 0.1] and
[charge > 0] and [pValue > 0.001]'
trackCutsminus = '[dr < 2.0] and [abs(dz) < 5.0] and [pt > 0.1]
and [charge < 0] and [pValue > 0.001] and [p > 0.3]'

cutAndCopyLists('pi+:good', 'pi+:all', trackCutsplus, path=my_path)
cutAndCopyLists('pi+:new', 'pi+:all', trackCuts, path=my_path)
cutAndCopyLists('K-:good', 'K-:all', trackCutsminus, path=my_path)

# other event based quantities
######################################################
reconstructDecay('D0:dec -> K-:good pi+:good', '1.77 < M < 1.97',
path=my_path)
treeFit('D0:dec',0.001, updateAllDaughters=False,
path=my_path)

reconstructDecay('D*+:dec -> D0:dec pi+:new', '0.0 < Q < 0.04',
path=my_path)
treeFit('D*+:dec',0.001, updateAllDaughters=False, path=my_path)
# alias variables
#######################################################
```

```
variables.addAlias('EoverP', 'formula(clusterE / p)')
variables.addAlias('pikExpPairPID_ARICH',
'pidPairProbabilityExpert(211,-321,ARICH)')
variables.addAlias('kpiExpPairPID_ARICH',
'pidPairProbabilityExpert(-321,211,ARICH)')

variables.addAlias('piExpPID_ARICH',
'pidProbabilityExpert(211,ARICH)')
variables.addAlias('kExpPID_ARICH',
'pidProbabilityExpert(-321,ARICH)')

variables.addAlias('piExpLogL_ARICH',
'pidLogLikelihoodValueExpert(211, ARICH)')
variables.addAlias('kExpLogL_ARICH',
'pidLogLikelihoodValueExpert(321, ARICH)')
variables.addAlias('pExpLogL_ARICH',
'pidLogLikelihoodValueExpert(2212, ARICH)')
variables.addAlias('eExpLogL_ARICH',
'pidLogLikelihoodValueExpert(11, ARICH)')
variables.addAlias('muExpLogL_ARICH',
'pidLogLikelihoodValueExpert(13, ARICH)')

# write out the info into an ntuple
#####################################################
eventVariables = ['Q','M','Ecms']
d0Variables = ['M']

trackVariables = ['theta', 'cosTheta', 'p', 'EoverP','nCDCHits','dr']
trackVariables += ['pikExpPairPID_ARICH','kpiExpPairPID_ARICH']
```

```
trackVariables += ['piExpPID_ARICH','kExpPID_ARICH','dz','M']
trackVariables += ['piExpLogL_ARICH','kExpLogL_ARICH','pExpLogL_ARICH'
trackVariables += ['eExpLogL_ARICH','muExpLogL_ARICH']

dstarVariableList = vu.create_aliases_for_selected
                    (list_of_variables=eventVariables,
                    decay_string='^D*+:dec',
                    prefix=['part_dst']) + \
                    vu.create_aliases_for_selected
                   (list_of_variables=d0Variables,
                    decay_string='D*+:dec -> ^D0 ^pi+',
                    prefix=['part_d0','part_pip']) + \
                    vu.create_aliases_for_selected
                    (list_of_variables=trackVariables,
                    decay_string='D*+:dec -> [D0 -> ^K- ^pi+] ^pi+',
                    prefix=['part_d0_km','part_d0_pip','part_dst_pip']


ma.variablesToNtuple(decayString='D*+:dec',
                     variables=dstarVariableList,
                     filename=outfilename,
                     treename='Dstar',
                     path=my_path)

# Process the events
b2.process(my_path)

# print out the summary
print(b2.statistics)
```

Invariant mass fitting code from Jupyter Notebook

```
## Plot pictures for signal and Background
import os, sys, ROOT
from math import *
from IPython.display import IFrame
from ROOT import kTRUE, kFALSE, kBlue, kRed, kGreen, kBlack

part_d0_M  = ROOT.RooRealVar("part_d0_M", "", 1.82,1.92)
part_d0_M.setBins(40)

part_dst_Q =  ROOT.RooRealVar("part_dst_Q", "", 0.0,0.04)
part_d0_pip_p = ROOT.RooRealVar("part_d0_pip_p",
"kaon_momentum [GeV]", 0.0,6.0)
part_d0_pip_theta = ROOT.RooRealVar("part_d0_pip_theta",
"theta", 0.0, 3.0)
part_dst_useCMSFrame_p = ROOT.RooRealVar("part_dst_useCMSFrame_p",
"CMS_p", 0.0, 7.0)
part_d0_pip_pikExpPairPID_ARICH =
ROOT.RooRealVar("part_d0_pip_pikExpPairPID_ARICH", "PID", 0.0,1.0)
part_d0_km_kpiExpPairPID_ARICH =
ROOT.RooRealVar("part_d0_km_kpiExpPairPID_ARICH", "PID", 0.0,1.0)

chain = ROOT.TChain("Dstar")
chain.Add("/home/gayane.gevondyan/Main/data.root")

data_exp = ROOT.RooDataSet("data_exp","data_exp",ROOT.RooArgSet
(part_d0_M,part_d0_pip_p,part_d0_pip_theta,part_dst_Q,
```

```
part_dst_useCMSFrame_p),ROOT.RooFit.Import(chain),
ROOT.RooFit.Cut("part_d0_pip_p > 1.0 && part_d0_pip_p < 1.7 &&
part_d0_pip_theta > 0.42 && part_d0_pip_theta < 0.45 &&
part_dst_useCMSFrame_p > 2.5 && part_dst_Q < 0.01 && part_dst_Q > 0.0"

#Construct signal pdf
mean1 = ROOT.RooRealVar("#mu", "mean1", 1.87, 1.82, 1.92)
sigma1 = ROOT.RooRealVar("#sigma", "sigma1", 0.005, 0.0001, 1.0)
signalModel = ROOT.RooGaussian("signalModel", "gaus", part_d0_M,
mean1, sigma1)

mean2 = ROOT.RooRealVar("mean2", "mean2", 1.88, 1.82,1.92)
sigma2 = ROOT.RooRealVar("sigma2", "sigma2", 0.05, 0.00, 2.0)
gx2 = ROOT.RooGaussian("gx2", "gx2", part_d0_M, mean2, sigma2)

# Construct background pdf
a0 = ROOT.RooRealVar("a0", "a0", -0.1, -10, 10)
a1 = ROOT.RooRealVar("a1", "a1", 0.04, -10, 10)
a2 = ROOT.RooRealVar("a2", "a2", 0.008, -10, 10)
param = ROOT.RooArgList()
param.add(a0)
param.add(a1)
param.add(a2)

background = ROOT.RooChebychev("background", "px", part_d0_M,
ROOT.RooArgList(a0,a1))

# Construct composite pdf
f1 = ROOT.RooRealVar("f1", "f1", 0.5, 0.0, 1.0)
```

```
weight = ROOT.RooArgList()
weight.add(f1)

function_list = ROOT.RooArgList()
function_list.add(background)
function_list.add(signalModel)

nsig = ROOT.RooRealVar("nsig","#signal events",20000,0.,200000.);
nbkg = ROOT.RooRealVar("nbkg","#background events",10000,0.,100000.);

gaus1_frac = ROOT.RooRealVar("gaus1_frac", "fraction of Gaussian
1 in signal", 0.8, 0.0, 1.0)
gaussian_sum = ROOT.RooAddPdf("gaussian_sum","Add two Gaussians",
ROOT.RooArgList(signalModel,gx2), gaus1_frac)

# RooFit Extended pdf
sig_extended = ROOT.RooExtendPdf("sig_extended","sig_extended",
gaussian_sum,nsig)
bkg_extended = ROOT.RooExtendPdf("bkg_extended","bkg_extended",
background,nbkg)

#model = ROOT.RooAddPdf("model","gauss+chebyshev",
ROOT.RooArgList(gaussian_sum,background), ROOT.RooArgList(nsig,nbkg))
model = ROOT.RooAddPdf("model","gauss+chebyshev",
ROOT.RooArgList(sig_extended,bkg_extended),
ROOT.RooArgList(nsig,nbkg));

# Make a frame for the physics sample
frame =  part_d0_M.frame()
```

```
r = model.fitTo(data_exp,ROOT.RooFit.Extended(kTRUE),
ROOT.RooFit.Save())
fit_param = ROOT.RooArgSet()
fit_param = model.getVariables()

mean = fit_param.find("#mu").getVal()
mean_err = fit_param.find("#mu").getError()

width = fit_param.find("#sigma").getVal()
width2 = fit_param.find("sigma2").getVal()
num_sig = fit_param.find("nsig").getVal()
num_bkg = fit_param.find("nbkg").getVal()

print("Mean, sigma, Nsig, Nbkg, mean_err", mean, width, num_sig,
num_bkg, mean_err)

print("width1,width2", width, width2)

part_d0_M.setRange("signal_initial",1.82,1.92)
part_d0_M.setRange("signal_final",mean - 3*width,mean + 3*width)

r1 = model.fitTo(data_exp,ROOT.RooFit.Extended(kTRUE),
ROOT.RooFit.Save(),ROOT.RooFit.NormRange("signal_final"))
fit_param2 = ROOT.RooArgSet()
fit_param2 = model.getVariables()

num_sig2 = fit_param2.find("nsig").getVal()
num_bkg2 = fit_param2.find("nbkg").getVal()
```

```
sig_err = fit_param2.find("nsig").getError()

width3 = fit_param2.find("#sigma").getVal()
width4 = fit_param2.find("sigma2").getVal()

print("sig_err", sig_err)
print("num_sig", num_sig)
print("num_sig2", num_sig2)
print("sigma3,sigma4", width3, width4)

# Get list of component objects, top-level node
model_comps = model.getComponents()
model_comps.Print("v")

frac_of_model= model.createIntegral(ROOT.RooArgSet(part_d0_M),
ROOT.RooArgSet(part_d0_M),"signal_final")
model_num = frac_of_model.getVal()*(num_sig + num_bkg)

frac_of_signal = gaussian_sum.createIntegral
(ROOT.RooArgSet(part_d0_M),ROOT.RooArgSet(part_d0_M),
"signal_final")

signal_num = frac_of_signal.getVal()*num_sig2
frac_of_signal0 = gaussian_sum.createIntegral
(ROOT.RooArgSet(part_d0_M),ROOT.RooArgSet(part_d0_M),"signal_final")
signal_num0 = frac_of_signal0.getVal()*num_sig

frac_of_bkg = background.createIntegral(ROOT.RooArgSet(part_d0_M),
ROOT.RooArgSet(part_d0_M),"signal_final")
```

```
background_num = frac_of_bkg.getVal()*num_bkg

frame2 = part_d0_M.frame()
data_exp.plotOn(frame2,ROOT.RooFit.Name("data_set"),
ROOT.RooFit.DataError(ROOT.RooAbsData.Poisson),
ROOT.RooFit.Binning(90),ROOT.RooFit.MarkerStyle(20),
ROOT.RooFit.MarkerSize(1.5),ROOT.RooFit.MarkerColor(kBlack))
model.plotOn(frame2,ROOT.RooFit.Name("gaus_cheby"),
ROOT.RooFit.LineWidth(4)) #Model name, attributes
model.plotOn(frame2,ROOT.RooFit.Components("background"),
ROOT.RooFit.LineColor(kRed),ROOT.RooFit.LineStyle(4),
ROOT.RooFit.NormRange("signal_initial"))
model.plotOn(frame2,ROOT.RooFit.Components("gaussian_sum"),
ROOT.RooFit.LineColor(kGreen),ROOT.RooFit.LineStyle(4),
ROOT.RooFit.NormRange("signal_final"))
model.paramOn(frame2, ROOT.RooFit.Layout(0.7))
frame2.getAttText().SetTextSize(0.03)

chi2_frame = frame2.chiSquare("gaus_cheby","data_set")

print("model_num = ", model_num)
print("frac_of_signal = ", frac_of_signal)
print("signal_num =   ", signal_num)
print("signal_num0 =   ", signal_num0)
print("background_num =   ", background_num )

c = ROOT.TCanvas("c","The Canvas Title",900,600)
frame2.Draw()
c.SaveAs('mc_p2_n_042045.png')
```